

UNIVERSIDADE FEDERAL DE MINAS GERAIS  
Escola de Engenharia  
Colegiado do Curso de Graduação em Engenharia ...

Nome da pessoa autora

**TÍTULO DO TRABALHO**

Belo Horizonte  
2024

Nome da pessoa autora

## **TÍTULO DO TRABALHO**

Trabalho de Conclusão de Curso apresentado ao Curso de Engenharia de Sistemas da Universidade Federal Minas Gerais, como requisito parcial para o grau de bacharel (a) em Engenharia de Sistemas.

Orientadora: Profa. Dra. Fulana Beltrano

Coorientador: Prof. Dr. Ciclano da Silva

Belo Horizonte

2024

Troque pelo arquivo PDF da ficha  
catalográfica após obtê-la da biblioteca  
da sua unidade.

Troque pelo arquivo PDF da folha de aprovação ou ata de defesa após obtê-la do seu programa de pós-graduação (após a defesa).

*Esse trabalho é dedicado à aquela pessoa.*

# Agradecimentos

Você pode escrever aqui os agradecimentos a pessoas que contribuíram para a realização do trabalho.

“Aqui vai uma bela e inspiradora frase.”

# Resumo

Escreva aqui o resumo do seu trabalho.

**Palavras-chave:** palavra-chave 1; palavra-chave 2; palavra-chave 3.



# Abstract

Translate here the abstract of your work.

**Keywords:** keyword 1; keyword 2; keyword 3.

# Lista de Siglas e Símbolos

## Siglas

ACO	Ant Colony Optimization
BIM	Born Iterative Method
CNN	Convolutional Neural Networks
DE	Differential Evolution
EA	Evolutionary Algorithm
GA	Genetic Algorithm
GAN	Generative Adversarial Network
PSO	Particle Swarm Optimization
TMz	Modo Magnético Transversal em $z$

## Símbolos

$\varepsilon$	Permissividade complexa [F/m + $j\Omega$ /m]
$\varepsilon_r$	Permissividade relativa
$\theta$	Ângulo da coordenada polar [rad]
$\lambda_b$	Comprimento de onda de fundo [m]
$\sigma$	Condutividade [ $\Omega$ /m]
$\phi$	Ângulo de incidência [rad]
$\mathbf{E}$	Vetor de intensidade elétrica [V/m]
$E_z$	Componente $z$ do vetor de intensidade elétrica [V/m]
$k$	Número de onda [1/m]
$\mathbb{R}$	Conjunto dos números reais
$\mathbf{r}$	Vetor posição no espaço 3D [m]
$x, y, z$	Coordenadas cartesianas [m]
$V$	Espaço tridimensional

# Sumário

<b>1</b>	<b>Introdução</b>	<b>13</b>
1.1	Objetivos Geral e Específicos . . . . .	13
1.2	Contribuições e Originalidade . . . . .	13
1.3	Organização do Trabalho . . . . .	13
<b>2</b>	<b>Revisão Bibliográfica</b>	<b>14</b>
<b>3</b>	<b>Metodologia</b>	<b>15</b>
<b>4</b>	<b>Results</b>	<b>17</b>
4.1	Case Studies . . . . .	17
4.1.1	Austria Profile . . . . .	18
4.1.2	Multiple Scatterers . . . . .	25
4.1.3	Non-Homogeneous Scatterer . . . . .	30
4.1.4	Strong Scatterer . . . . .	36
4.2	Benchmarking . . . . .	43
4.2.1	Test Sets and Algorithms Parameters Considerations . . . . .	44
4.2.2	Discussion . . . . .	46
<b>5</b>	<b>Conclusion</b>	<b>55</b>
5.1	Recapitulation . . . . .	55
5.2	Self-Criticism . . . . .	58
5.3	Continuity Proposals . . . . .	58
5.4	Bibliographic Production . . . . .	59
	<b>Referências Bibliográficas</b>	<b>61</b>
<b>A</b>	<b>Como fazer citações</b>	<b>63</b>
<b>B</b>	<b>Como escrever equações</b>	<b>64</b>
<b>C</b>	<b>Como inserir figuras</b>	<b>66</b>

<b>D</b>	<b>Como inserir tabelas</b>	<b>69</b>
<b>E</b>	<b>Como inserir algoritmos</b>	<b>71</b>
<b>F</b>	<b>Como inserir definições e outras coisas especiais</b>	<b>72</b>
<b>G</b>	<b>Dyadic Green's Function</b>	<b>73</b>
G.1	Dyadic Green's Function for Homogeneous Medium . . . . .	73
G.2	The Singularity of the Dyadic Green's Function . . . . .	75
G.3	Dyadic Green's Function for Inhomogeneous Medium . . . . .	77
<b>H</b>	<b>Integral Equation Formulation</b>	<b>79</b>
<b>I</b>	<b>Functional Analysis</b>	<b>82</b>
I.1	Normed and Hilbert Spaces . . . . .	82
I.2	Linear Bounded and Compact Operators . . . . .	85
<b>J</b>	<b>Shape metrics</b>	<b>88</b>

# Capítulo 1

## Introdução

Parte inicial do texto na qual se apresenta a delimitação do assunto tratado, os objetivos da pesquisa e outros elementos necessários para apresentar o tema do trabalho. O texto tem o objetivo de introduzir o leitor ao trabalho e apresentar as informações para uma compreensão geral da proposta desenvolvida.

### 1.1 Objetivos Geral e Específicos

Descrever os objetivos geral e específicos do trabalho. O objetivo geral devem ser claro e conciso, indicando o propósito do trabalho. Os objetivos específicos devem ser apresentados de forma a indicar os passos necessários para atingir o objetivo geral. Geralmente, em formato de tópicos.

### 1.2 Contribuições e Originalidade

Descrever as contribuições do trabalho, indicando o que o trabalho propõe de novo ou diferente em relação ao estado da arte. As contribuições devem ser claras e objetivas, indicando o que o trabalho agrega ao conhecimento existente.

### 1.3 Organização do Trabalho

Descrever a organização do trabalho, indicando o conteúdo de cada capítulo e a relação entre eles. A organização do trabalho deve ser clara e coerente, de forma a facilitar a compreensão do leitor.

## Capítulo 2

# Revisão Bibliográfica

Ao redigir uma revisão bibliográfica em trabalhos acadêmicos, é crucial adotar uma abordagem sistemática e crítica. Inicie identificando e selecionando fontes relevantes que abordem diretamente o tema de pesquisa, priorizando publicações acadêmicas revisadas por pares, como artigos de periódicos, livros e conferências. Uma boa prática é organizar a literatura em temas ou escolas de pensamento, facilitando a compreensão do leitor sobre o estado da arte e as lacunas existentes. É importante também avaliar criticamente cada obra, discutindo sua contribuição para o campo, metodologias, resultados e limitações. A revisão deve ser escrita de forma coesa, com transições suaves entre os trabalhos discutidos, e deve terminar destacando como a pesquisa atual se insere e contribui para o conhecimento existente. Citando adequadamente todas as fontes, evita-se o plágio e reconhece-se o trabalho dos pesquisadores originais, além de fornecer ao leitor caminhos para aprofundamento.

# Capítulo 3

## Metodologia

Redigir um capítulo sobre metodologia em um trabalho acadêmico é fundamental para demonstrar a validade e a confiabilidade da pesquisa. Este capítulo deve detalhar os procedimentos e técnicas utilizados para coletar e analisar dados, permitindo que outros pesquisadores reproduzam o estudo. Aqui estão os passos essenciais para escrever um capítulo de metodologia eficaz:

- **Introdução à Metodologia:** Comece com uma breve introdução que esclareça o propósito do capítulo e como ele contribui para os objetivos gerais da pesquisa.
- **Descrição da Pesquisa:** Especifique o tipo de pesquisa realizada (qualitativa, quantitativa, mista) e justifique a escolha. Explique como essa abordagem é adequada para responder às perguntas de pesquisa ou hipóteses.
- **Participantes ou Dados:** Descreva a população-alvo, critérios de inclusão e exclusão, e como os participantes ou dados foram selecionados. Para pesquisas experimentais, explique como os grupos de controle e experimentais foram formados.
- **Instrumentos e Materiais:** Liste os instrumentos, ferramentas, ou materiais utilizados na coleta de dados, incluindo questionários, entrevistas, software, etc. Descreva como e por que cada instrumento foi escolhido.
- **Procedimento:** Detalhe todos os passos seguidos durante a coleta de dados. Para experimentos, descreva as condições sob as quais foram realizados, incluindo variáveis controladas e não controladas.
- **Análise de Dados:** Explique as técnicas estatísticas, métodos de análise qualitativa, ou modelos utilizados para analisar os dados coletados. Justifique a escolha desses métodos e discuta sua adequação para o tipo de dados coletados.
- **Validade e Confiabilidade:** Discuta as medidas tomadas para garantir a validade e confiabilidade dos resultados. Isso pode incluir a validação de instrumentos, triangulação de dados, ou testes piloto.
- **Limitações:** Reconheça quaisquer limitações metodológicas que possam afetar os resultados ou a interpretação da pesquisa.
- **Ética:** Se aplicável, descreva as considerações éticas relacionadas à pesquisa, incluindo

aprovações de comitês de ética, consentimento informado dos participantes, e como a privacidade e a confidencialidade foram mantidas.

- **Resumo:** Conclua o capítulo com um resumo dos pontos-chave, reforçando como a metodologia adotada permite abordar as perguntas de pesquisa ou testar as hipóteses.

Lembre-se de que a clareza e a precisão são cruciais neste capítulo. O objetivo é fornecer informações suficientes para que outros pesquisadores possam entender como o estudo foi conduzido e, se desejado, replicar a pesquisa.



# Capítulo 4

## Results

Chapter 5 presents the results of the computational experiments conducted in this thesis, evaluating the proposed methodologies through both case studies and benchmarking. The case studies are detailed in Section 4.1, which encompasses various problem scenarios, including single scatterers (subsection 4.1.1), multiple scatterers (subsection 4.1.2), non-homogeneous scatterers (subsection 4.1.3), and strong scatterers (subsection 4.1.4). In each case study, a comparison is made between the proposed algorithms and traditional deterministic methods.

Following the case studies, Section 4.2 focuses on the benchmarking study, which aims to assess the performance of the proposed methods and identify any potential differences among them. The subsection 4.2.1 introduces the settings of the benchmarking study, providing essential context for the subsequent analysis. Subsequently, the results are presented and discussed, offering insights into the performance of the algorithms.

Some general comments apply to both the case studies and benchmarking stages. Firstly, all designs utilized lossless materials. Additionally, the amplitude of the incident wave was consistently set at 1 [V/m]. To incorporate a level of realism, the scattered field data was subjected to random noise. This noise is a random complex number, with its modulus representing a percentage of the original value and its phase uniformly distributed between 0 and  $2\pi$ .

Regarding runtime results, they were obtained using a specific machine configuration: Ubuntu 20.04.5 LTS, Intel Xeon(R) CPU E5-2640 0 @ 2.50GHz with 8 cores, and 11.7 GB memory. It is important to note that the method implementations may not have been optimized to their fullest extent, potentially impacting runtime analysis fairness. Consequently, a completely fair runtime analysis cannot be guaranteed due to potential variations in implementation optimizations.

### 4.1 Case Studies

Case studies involve a comprehensive analysis of either a single or a set of specific instances of a problem. The aim is to deeply analyze these instances, carefully examining their

unique attributes. These instances are deliberately chosen to explore specific characteristics that hold relevance for the proposal. By examining these selected cases, valuable insights and understanding can be gained.

This section covers four case studies, each focusing on a different scenario. The first case study examines the behavior of the proposed algorithms in situations that can be easily solved using traditional methods. The second case study investigates the performance of the proposed algorithms in a scenario with multiple scatterers and a significant level of contrast. In the third case study, the objective is to analyze the behavior of the proposed algorithms when dealing with a non-homogeneous scatterer that exhibits different levels of contrast. Additionally, this case explores the capability of the qualitative method to provide suitable initial solutions in such scenarios. The fourth and final case study aims to observe the performance of the proposed algorithms in a scenario where traditional methods typically struggle to produce satisfactory solutions.

Throughout all the tests, a noise level of 20 [%/sample] is considered for the scattered field data. Such noise level might affect significantly the performance of some methods and, therefore, the goal is to analyze the performance under a challenging scenario. In addition to the five proposed algorithms discussed in Chapter ??, an evolutionary algorithm that transforms the inverse problem into a two-dimensional optimization problem will also be included. However, this algorithm does not employ surrogate models. Furthermore, four deterministic methods, namely ECSI (Subsection ??), SOM (Subsection ??), BIM (Subsection ??), and DBIM (Subsection ??), will be employed. The ECSI version van den Berg et al. (1999) of the CSI family of algorithms is chosen due to its slightly better performance and fewer control parameters.

For the algorithms assisted by surrogate models, the threshold variable ranges from 0 to 1. The Method of Moments CG-FFT (MoM-CG-FFT) used in the simulations employs a stopping criterion of a maximum of 20 iterations or an error tolerance level below  $10^{-3}$ . This choice allows for a rougher approximation and helps to save computational time.

The performance of the algorithms will be primarily analyzed based on the error in estimating the object contrast and recovering its shape. Hence, the  $\zeta_{\epsilon OE}$  and  $\zeta_S$  indicators will be measured, respectively. The decision not to use the  $\zeta_{\epsilon PAD}$  indicator is motivated by the fact that the thresholding operator employed in the proposed approach ensures a noise-free background. This could heavily favor the proposed approach and make the comparison with traditional methods less meaningful. Lastly, the maximum number of iterations for each algorithm is determined based on the convergence of their objective function or the point just before a divergence behavior is observed.

#### 4.1.1 Austria Profile

The present case study considers the Austria profile, which is a widely used instance in the literature (Chen, 2010, 2017), to test the algorithms in a weak scattering scenario (DNL

$= 0.694$ ). The profile has multiple and homogeneous scatterers, one of which is hollow. The Fig. 4.1a shows the ground-truth image and further information regarding the parameters of the scatterers can be found in (Chen, 2010). The Table 4.1 shows the parameters regarding the measurement and imaging domains and the incident field configuration. The resulting background wavelength is 0.749 [m]. Scattered field data was synthesized using MoM-CG-FFT, with a stopping criterion of 15,000 iterations or error tolerance level less than  $10^{-5}$ , and the resolution of the original image was  $64 \times 64$ , while the reconstruction resolution was  $30 \times 30$ .

Tabela 4.1: Parameters for problem specification of Austria profile case study.

$N_M$	$N_S$	$R_O$	$f$	$L_X, L_Y$	$\epsilon_{rb}$
32	16	6 [m]	400 [MHz]	2 [m]	1

The surrogate model-assisted algorithms proposed in this study have many parameters. The parameters for this case study were chosen based on a *prior* analysis. The contrast variable range was set to 0 to 1, and the stopping criterion for each surrogate model-assisted algorithm was defined as the maximum number of evaluations, which was 26 evaluations, with 30 runs due to the stochastic characteristics present in them. Despite being based on deterministic choices, the SADM2 algorithm will be executed multiple times, and the rationale behind this decision will be elucidated in the upcoming case studies. The number of solutions sampled at the beginning was 16, and the local search operation in SAEAs algorithms happened every 5 generations. The mutation factor  $F$  present in the mutation processes of SAEAs algorithms was randomly chosen in the range of 0.6 to 1.5 following a uniform distribution. The population size in the initial solution search process for SADM1 was set at 100 individuals. For the transformation-based algorithms, MoM-CG-FFT forward solver was used to evaluate solutions, with a limited number of iterations of 20 or until reaching an error tolerance level of 0.001. In addition to the surrogate model-assisted evolutionary algorithms, a traditional evolutionary algorithm formulation was also considered in this case study for comparison purposes. The DE/rand/1/bin formulation was chosen, with  $F$  adjusted to 0.5 and the crossing rate to 0.5.

The parameter configuration of the deterministic algorithms is mostly related to the stop criteria, which includes the maximum number of iterations and the error tolerance level. The established stopping criterion for SOM was the maximum number of iterations equal to 50, with a cut-off parameter of eigenvalues set at 15. The initial guess for SOM, ECSI and CGM was defined as the solution of the Backpropagation algorithm (Subsection ??). The stopping criterion for CGM and ECSI was set to 40 and 50 iterations, respectively. The stopping criterion for DBIM was 3 iterations, with the regularization method as Tikhonov's with a parameter equal to 0.01. Finally, BIM used the same parameters as DBIM, except for the stopping criterion, which was adjusted to 10 iterations. Both algorithms are considered the Born Approximation (Subsection ??) as initial guess strategy.

In the results of the case study, Fig. 4.1 displays the best of the reconstructions among

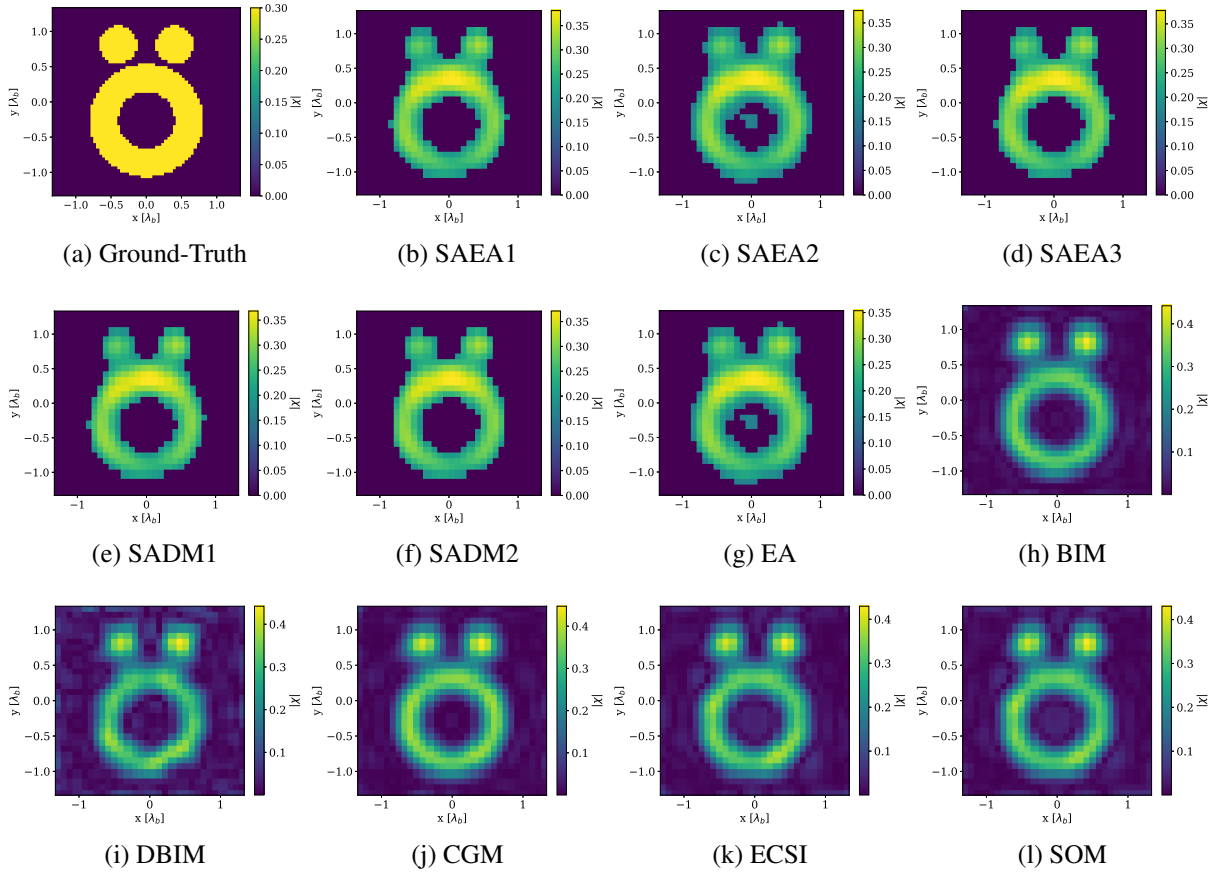


Figure 4.1: Comparison of image reconstructions using surrogate model-assisted algorithms and deterministic methods considering the Austria profile case study: (a) shows the ground-truth image; (b), (c), and (d) depict the best image recovered by SAEA1, SAEA2, and SAEA3, respectively, in 30 execution according to  $\zeta_{\epsilon OE}$  indicator; (e), (f) and (g) show the best image recovered by SADM1, SADM2, and EA, respectively, in 30 execution according to  $\zeta_{\epsilon OE}$  indicator; (g) shows the image recovered by BIM, and (h) shows the image recovered by DBIM; finally, (i), (k), and (l) show the image recovered by CGM, ECSI, and SOM, respectively.

the 30 runs of each stochastic algorithm, based on indicator  $\zeta_{\epsilon OE}$  (Figs. 4.1b-4.1g), and also includes the reconstructions of the deterministic algorithms (Figs. 4.1h-4.1l). The figures show that all algorithms overestimated the contrast slightly, which can be seen in the maximum contrast value in each figure. However, algorithms based on the problem transformation proposal tended to have slightly lower overestimation, which compensates for underestimation at the edges of the scatterer. The reconstructions also had some difficulty in detecting the separation between the ring and the two circles, which was related to the proximity between these objects. Additionally, the best SAEA2 and EA reconstructed images showed a small ghost object inside the image ring due to a threshold value adjustment issue. As the  $\zeta_{\epsilon OE}$  indicator only takes into account the estimate within the original region of the scatterer, then errors in the original background region of the problem do not influence the indicator. Furthermore, algorithms based on transforming the problem into a two-dimensional optimization problem showed a cleaner background region, which was attributed to the thresholding operator. BIM (Fig. 4.2g) presented

a slightly cleaner background region than DBIM (Fig. 4.2h), which was associated with the difficulty of DBIM in dealing with significant noise levels.

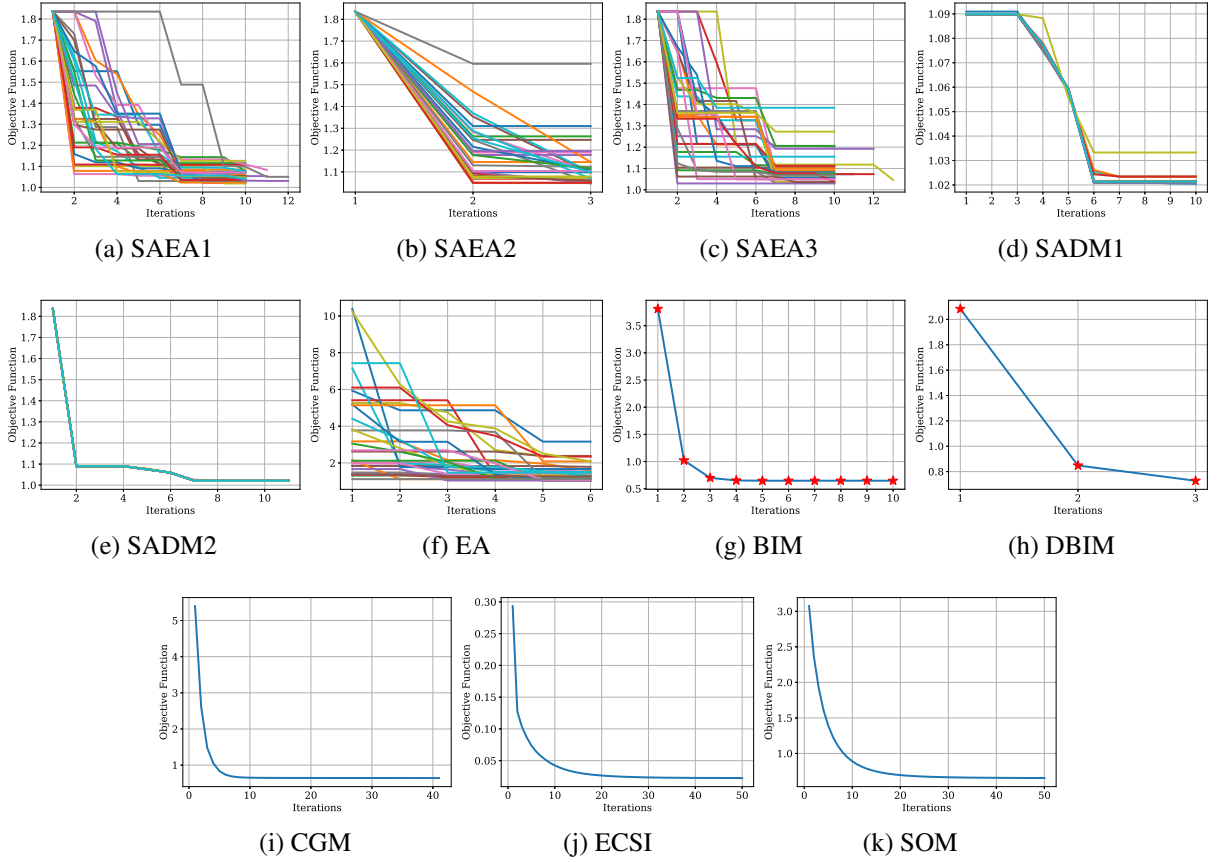
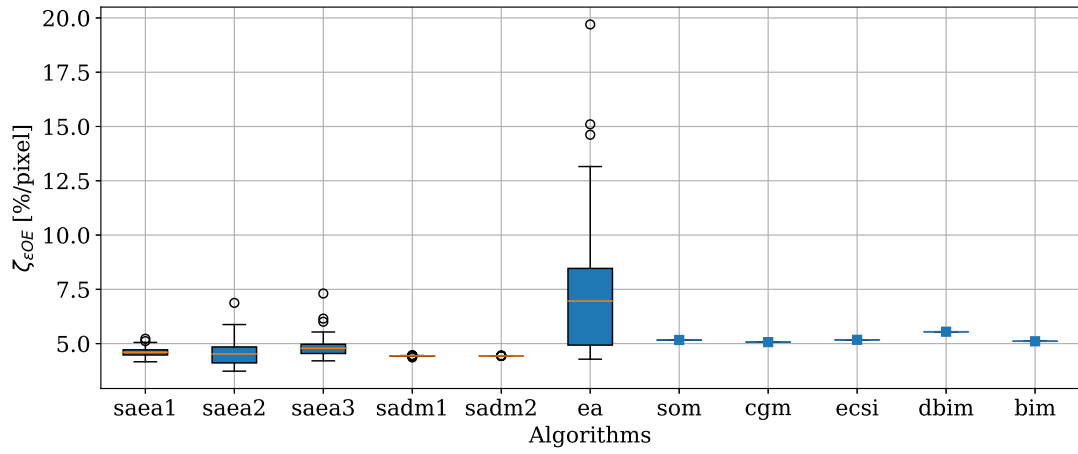


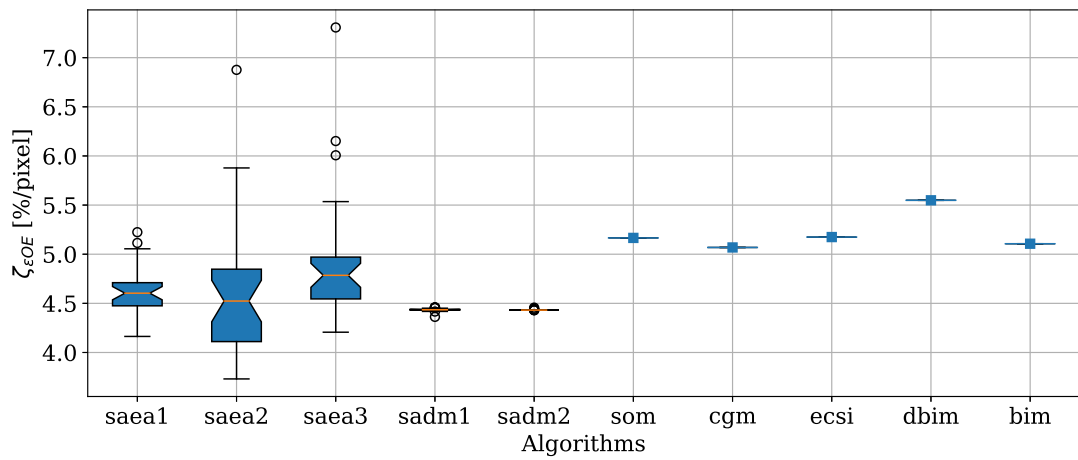
Figure 4.2: Convergence of the objective function for the Austria profile case obtained by the stochastic and deterministic algorithms. (a) to (k) show the curves obtained by SAEA1, SAEA2, SAEA3, SADM1, SADM2, EA, BIM, DBIM, CGM, ECSI, and SOM algorithms, respectively. The x-axis represents the number of iterations, and the y-axis represents the value of the objective function of the correspondent algorithm.

The convergence curve for each algorithm is shown in Fig. 4.2. The y-axis can only be compared between algorithms based on two-dimensional optimization (Figs. 4.2a-4.2f), as each deterministic algorithm has its own objective function that guides its structure. SAEA2 had a few generations but still achieved values close to those achieved by SAEA1 and SAEA3, thanks to the good mapping of the search space done by the initial population. The final values reached by SAEA1 in the 30 runs were more similar than those by SAEA3, which may suggest that SAEA1 convergence is better.

Some SADM1 runs did not converge to the same location as most, which may be an effect of the stochastic search process for the initial solution. The same does not happen for SADM2, as all executions of this algorithm converged equally, indicating a deterministic behavior. The EA has more generations than the SAEA2, but the greater number of generations did not contribute to reaching the region closer to the minimum more quickly. This is straightforward for SAEA2 because of the solution sampling strategy.



(a)



(b)

Figure 4.3: Performance of  $\zeta_{\epsilon OE}$  indicator for various algorithms in the Austria profile. (a) Boxplots show quartiles of 30 executions for stochastic algorithms, and the solid line represents the deterministic algorithms. (b) Exclusion of the EA algorithm for better visualization of differences among algorithms.

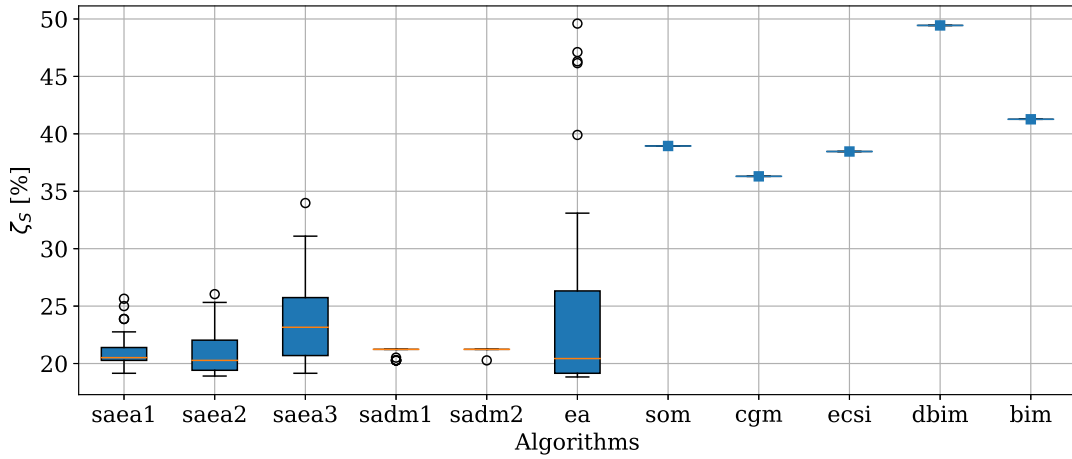


Figura 4.4: Performance of shape error estimation quantified by the  $\zeta_S$  indicator obtained by the set of algorithms considering the Austria profile. The boxes represent the quartiles of the 30 executions of the stochastic algorithms, while the other points indicate the obtained values by the deterministic ones. The shape error is calculated based on the ground-truth image and the reconstructed image obtained by each algorithm.

Fig. 4.3a shows the  $\zeta_{EOE}$  indicator quartiles for the algorithms in which 30 executions were performed and the value reached by the deterministic ones. The EA quartiles stand out negatively, as the algorithm has difficulty finding a good final estimate of the scatterer contrast. This is attributed to the algorithm's need for more generations to converge closer to the optimum, as in other algorithms assisted by surrogate models.

By removing the EA data (Fig. 4.3b), it is possible to better visualize the differences between the algorithms assisted by surrogate models and the deterministic ones. The median of algorithms assisted by surrogate models was below all deterministic ones. In particular, all SADM1 and SADM2 runs were below the deterministic contrast estimation error. However, there have been executions of SAEA's that ended with a minor error. All runs of SADM2 ended with the same error since all runs converged equally (as seen in Fig. 4.2e). Although SADM1 convergence was not as equal between runs, they achieved the same error, indicating that the final solution for each run was very close. The Kruskal-Wallis H-Test confirmed difference among SAEA1, SAEA2, and SAEA3 (p-value = 0.0219), and all-to-all comparison by Mann-Whitney U test confirmed that SAEA1 and SAEA2 overperformed SAEA3 (p-values 0.0199 and 0.0191, respectively). The Multiple Mann-Whitney U test did not detected difference between SADM1 and SADM2 (p-value = 0.0505).

The contrast estimation error of surrogate model-assisted algorithms has to do with where on the optimization surface they end up. In general, the result indicates that the problem transformation approach can be successful in making a better contrast estimate in the median of cases compared to the traditional approaches. However, in weak scattering scenarios, this difference is not as significant as the graphs show (up to 1.5 [%/pixel]).

The performance of different algorithms for shape recovery error ( $\zeta_S$ ) is shown in Fig.

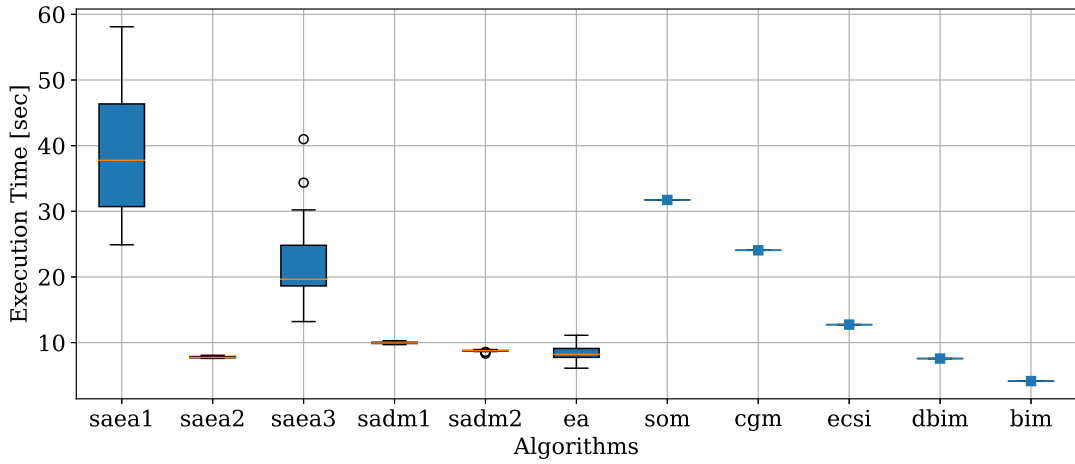


Figure 4.5: Box plot showing the execution time distribution of the set of algorithms considered for the Austria profile case. The boxes represent the quartiles of the 30 executions of the stochastic algorithms, and the whiskers represent the minimum and maximum values. The deterministic algorithms are represented by individual points. The execution time results are presented in seconds.

4.4. The difference in performance between deterministic algorithms and those based on the transformation of the problem is more significant, up to approximately 20% of the area of the original scatterer. The success of the proposed transformation approach in shape recovery results is associated with the quality of the qualitative methods used and the efficiency of the thresholding operation intrinsic to the formulation. The Kruskal-Wallis H-Test confirmed difference among SAEA1, SAEA2, and SAEA3 (p-value  $< 0.0002$ ), and all-to-all comparison by Multiple Mann-Whitney U test confirmed that SAEA1 and SAEA2 overperformed SAEA3 (p-values  $< 0.001$  for both cases). The Mann-Whitney U test detected difference suggesting that SADM1 outperform SADM2 (p-value = 0.013).

The running time of the algorithms is shown in Fig. 4.5. The median of SAEA1 was found to be the highest, while SAEA2 was the fastest among SAEA's formulations, even with the same number of evaluations. This suggests the impact of operations within the iterative process of these algorithms, such as the local search process and the number of model training calls that are less triggered in SAEA2 for the same number of evaluations. However, it is important to note that SADM also need to retrain the model once per iteration, spend one evaluation per iteration, and use the same algorithm applied for the local search process in SAEAs. Other processes that are part of the implementation of these algorithms may also be impacting the runtime. It is also worth highlighting that although BIM takes much less time than SADM2, the latter still manages to deliver good contrast and shape estimation results for a satisfactory time (less than 10 seconds), which is shorter than other algorithms such as SOM, CGM, and ECSI. Therefore, with a little more time, SADM2 can deliver a better result in this instance that is well-treated by traditional algorithms.

Figure 4.6 illustrates the performance of the algorithms, displaying both the objective



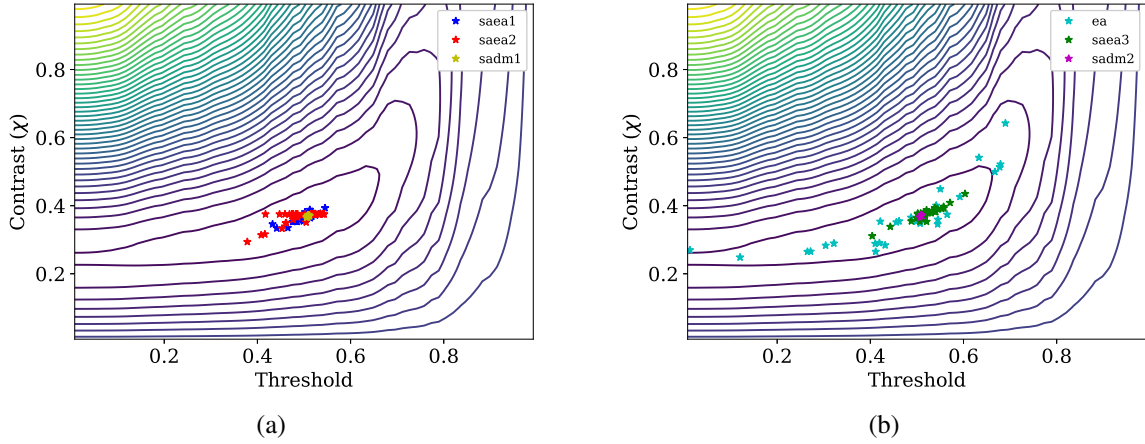


Figure 4.6: Surface of the two-dimensional optimization problem obtained from the transformation of the Austria profile and the final solutions obtained by different algorithms. Subfigure (a) shows the final solutions obtained by SAEA1, SAEA2, and SADM1 algorithms, while subfigure (b) shows the final solutions obtained by EA, SAEA3, and SADM2 algorithms.

function surface and the locations of the final solutions obtained by each algorithm after transforming the inverse problem into a two-dimensional optimization problem. The SADMs converged to the same point every time, indicating that they behaved like deterministic algorithms for a reasonably smooth surface in the macro sense. The EA solutions, on the other hand, were widely spread, indicating that the number of evaluations would need to be much higher for the algorithm to converge more often to the optimal location.

The SAEA3 had a similar behavior to EA, which slightly moved away from the point found by the SADMs. However, it is important to note that final solutions that are a little farther from the optimum can sometimes return a smaller error in contrast estimation or shape recovery. This is because the optimal point of the transformed problem can be slightly displaced from what would be ideal for the thresholding process and the exact contrast value. This displacement is intrinsic to the estimation of the qualitative method. That is, the optimal solution of the transformed problem is not necessarily the exact one, but the best that can be obtained from the qualitative method and minimizing the error of the data equation. Therefore, the performance of the qualitative method influences the position of the optimum.

### 4.1.2 Multiple Scatterers

This subsection presents a case study that examines the ability to separate objects in an image when considering multiple scatterers. This type of scenario is significant and, in order to further explore the application potential of the surrogate models, the contrast of the scatterers will be considerably higher. The study describes three scatterers that have a contrast level equal to 4. The radius of the circle is  $0.1\lambda_b$  and is centered on coordinates  $(L_X/4, 0)$ . The side of the square is  $0.2\lambda_b$  and is centered on coordinates  $(-L_Y/4, -L_X/4)$ , while the side of the triangle is

$0.2\lambda_b$  and is centered on coordinates  $(-L_Y/4, L_X/4)$ . The instance can be seen in Fig. 4.7a and it is inspired in an experiment presented in (Shah and Moghaddam, 2015) and (Batista et al., 2021) where the same geometries were considered and different contrast levels. The DNL of the problem was at 0.915, which is close to threshold 1 for the problem to start to get very non-linear. The parameters that describe the problem domains are present in Table 4.2. All other settings for synthesizing the scattered field data are the same as in the previous case study, except now the original image resolution is  $120 \times 120$ .

Tabela 4.2: Parameters for problem specification of the multiple scatterers case study.

$N_M$	$N_S$	$\lambda_b$	$R_O$	$L_X, L_Y$	$\epsilon_{rb}$
20	20	1 [m]	5 [ $\lambda_b$ ]	0.8 [ $\lambda_b$ ]	1

In this case study, the configuration of the algorithms was similar to the previous one, but some adjustments were necessary to explore the behavior of the algorithms more effectively. For the algorithms based on problem transformation, some changes were made, including increasing the maximum limit for the contrast variable to 7 since the true contrast is now 4, setting the stopping criterion to 50 evaluations, and using an initial sample size of 25 solutions. SAEA2 and EA were designed with populations consisting of 20 individuals. As for the deterministic methods, some modifications were made, including 150 iterations for CGM, 200 iterations for ECSI, 4 iterations for DBIM, 20 iterations for BIM, and 200 iterations for SOM, with a cut-off index equal to 5.

The results are presented in Fig. 4.7, which displays the best reconstructions of the algorithms that were executed multiple times following the same criteria as the previous case study, along with images of the deterministic methods. In the case of algorithms based on the transformation of the problem (Figs. 4.7b-4.7g), the scatterers appeared a little more displaced from the center of the reconstructed image, and they were very close to the edges of the image. However, the best estimates of the contrast were excellent. BIM (Fig. 4.7h) was not successful in detecting the scatterers, while DBIM (Fig. 4.7i) displayed significant noise in the background region, even though it might look like there are three scatterers in the image. CGM, ECSI, and SOM (Figs. 4.7j-4.7l) were able to detect three scatterers with values less close to the exact one than the proposed algorithms, although CGM had more difficulty with background noise.

Figure 4.8 presents the convergence of the objective function for each algorithm. Interestingly, the convergence of the SADM1 and SADM2 algorithms (Figs. 4.8d-4.8e) was less homogeneous in this case study, behaving more like a stochastic algorithm such as SAEAs. Although the decisions within the iterative process of SADM are deterministic, the differences in the convergence curves between runs could be due to the processes within the surrogate model training, which can be more complex in high-contrast scattering scenarios.

On the other hand, the convergence curves of the SAEAs algorithms were similar to those of the previous case study. SAEA1 (Fig. 4.8a) had slightly more homogeneous curves

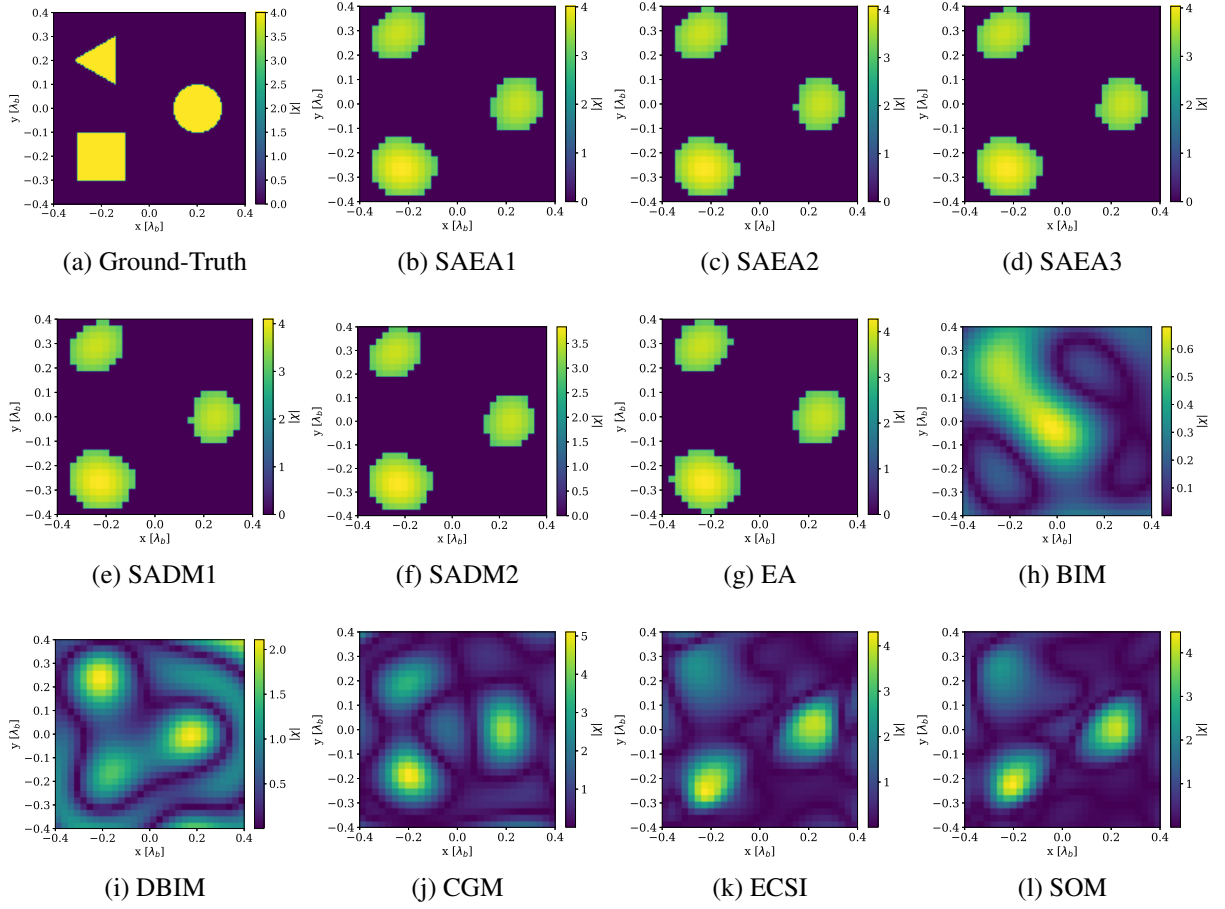


Figure 4.7: Comparison of image reconstructions using surrogate model-assisted algorithms and deterministic methods considering the multiple scatterers case study: (a) shows the ground-truth image; (b), (c), and (d) depict the best image recovered by SAEA1, SAEA2, and SAEA3, respectively, in 30 execution according to  $\zeta_{EOE}$  indicator; (e), (f) and (g) show the best image recovered by SADM1, SADM2, and EA, respectively, in 30 execution according to  $\zeta_{EOE}$  indicator; (g) shows the image recovered by BIM, and (h) shows the image recovered by DBIM; finally, (i), (k), and (l) show the image recovered by CGM, ECSI, and SOM, respectively.

than SAEA3 (Fig. 4.8c), and even though SAEA2 (Fig. 4.8b) had only 3 generations, some of the runs found solutions with the same objective function value as the best solutions found by the other two algorithms.

Finally, the convergence of the CGM, ECSI, and SOM algorithms (Figs. 4.8i-4.8k) indicates that they finished their runs with stable solutions. Therefore, even if more iterations were given, the reconstructed images would not significantly differ from those shown in Figures 4.7j-4.7l. In this scenario, these algorithms would not obtain a better reconstruction.

In Figure 4.9, the results of indicator  $\zeta_{EOE}$  for each algorithm are presented. The CGM algorithm had the lowest error in estimating the contrast of objects, but its reconstructed image was not as satisfactory as the other algorithms (Fig. 4.7j). However, even with a slight overestimation of the contrast compared to the surrogate model-assisted algorithms, the error may have been smaller due to the lack of distancing behavior observed for the proposed algorithm and that

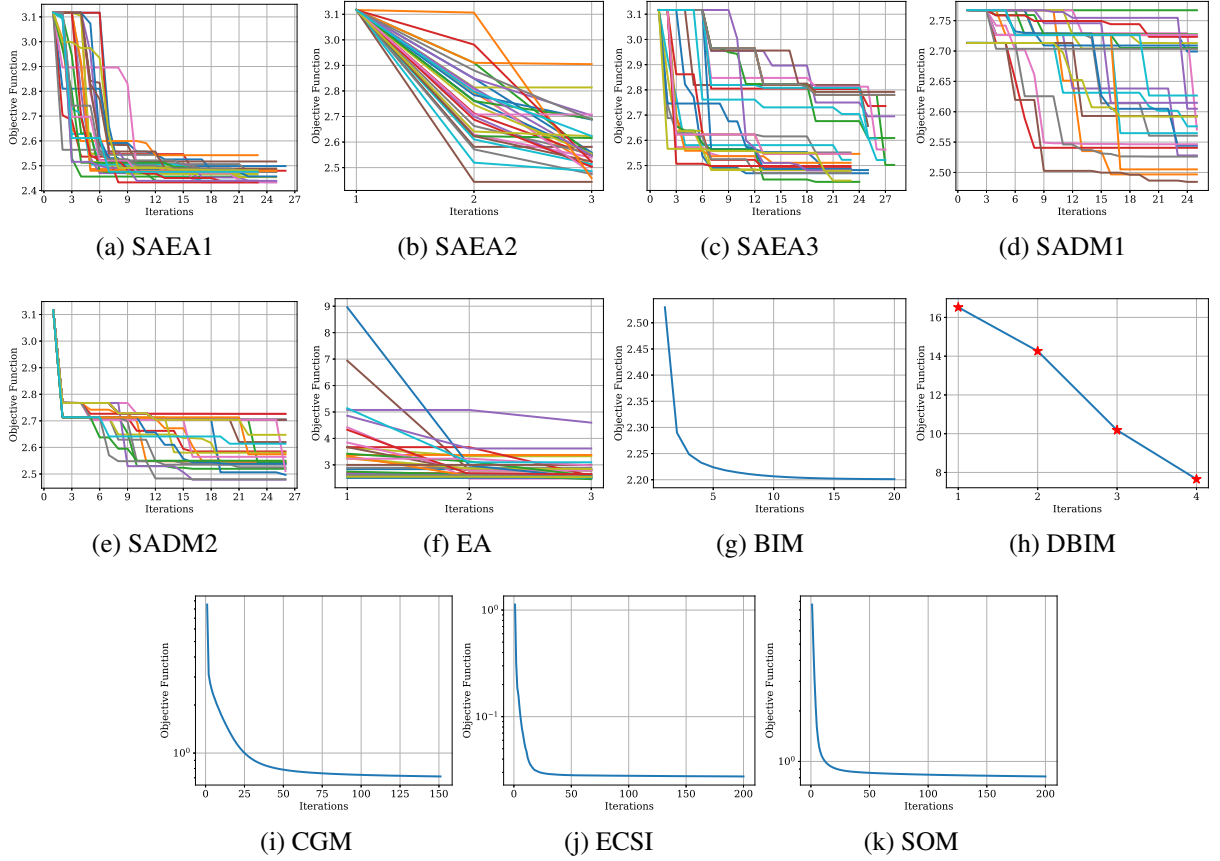


Figure 4.8: Convergence of the objective function for the multiple scatterers case obtained by the stochastic and deterministic algorithms. (a) to (k) show the curves obtained by SAEA1, SAEA2, SAEA3, SADM1, SADM2, EA, BIM, DBIM, CGM, ECSI, and SOM algorithms, respectively. The x-axis represents the number of iterations, and the y-axis represents the value of the objective function of the correspondent algorithm.

influences the error measure. The Kruskal-Wallis H-Test did not detect any differences in the median performance between the surrogate model-assisted algorithms, despite SAEA1 having a higher median position. The algorithms assisted by surrogate models had higher medians than the SOM, CGM, and ECSI methods, but the difference did not exceed 20 [%/pixel].

The results of the  $\zeta_S$  indicator that evaluates the shape recovery of the scatterers by the algorithms is presented in Fig. 4.10. The CGM algorithm had the lowest shape recovery error, with a significant difference of around 50 [%] compared to the second-best algorithm. However, none of the algorithms were able to reconstruct shapes that resembled the scatterers.

Regarding the surrogate model-assisted algorithms, the medians were very close to each other. When comparing the medians of SAEA2, SAEA3, SADM1, and SADM2 algorithms, the Kruskal-Wallis H-Test did not detect any difference at a significance level of 5% (p-value = 0.065). However, when including SAEA1 in the comparison, it showed a better median performance than the other algorithms (p-value < 0.001 in all post-hoc comparisons). Nonetheless, the difference is not significant enough from the point of view of the reconstructed image.

Figure 4.11 displays the results of the execution time of the algorithms. BIM and DBIM

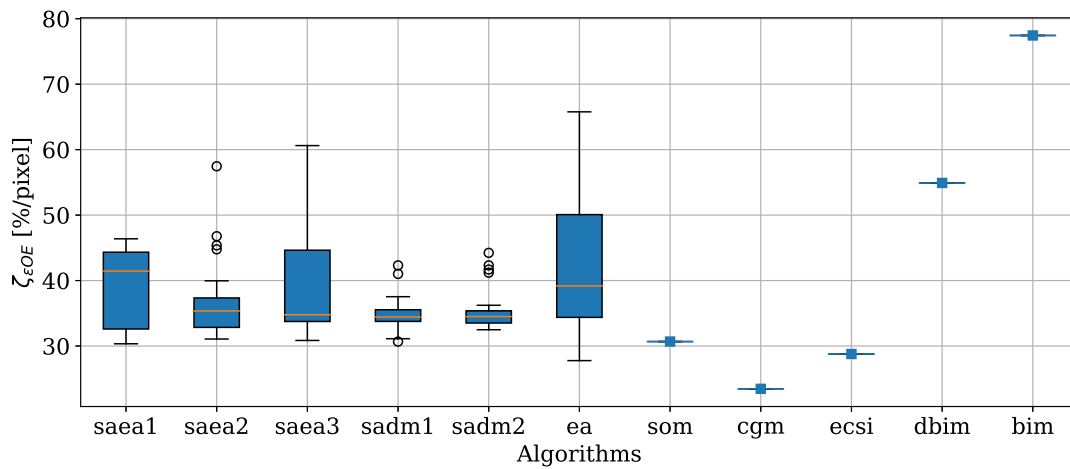


Figura 4.9: Performance of  $\zeta_{\epsilon OE}$  indicator for various algorithms in the multiple scatterers case study. Boxplots show quartiles of 30 executions for stochastic algorithms, and the solid line represents the deterministic algorithms.

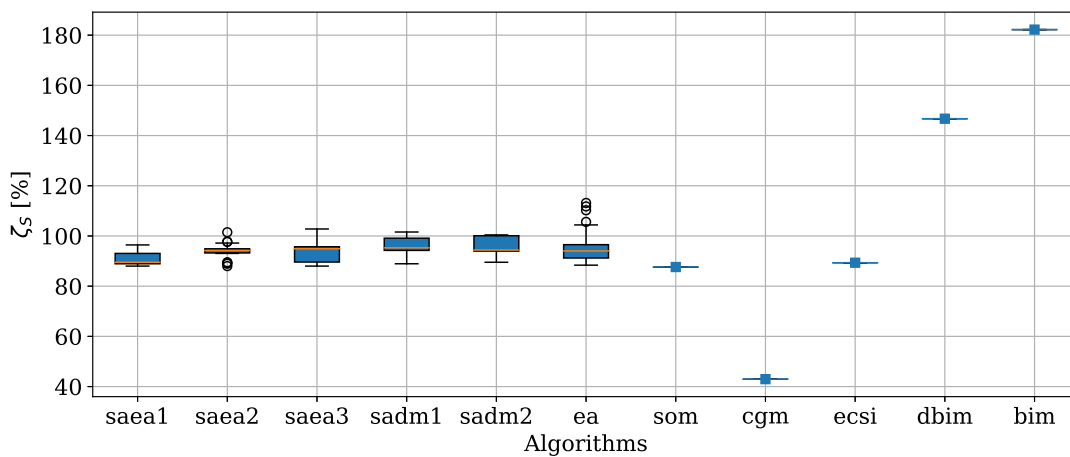


Figura 4.10: Performance of shape error estimation quantified by the  $\zeta_S$  indicator obtained by the set of algorithms considering the multiple scatterers case study. The boxes represent the quartiles of the 30 executions of the stochastic algorithms, while the other points indicate the obtained values by the deterministic ones. The shape error is calculated based on the ground-truth image and the reconstructed image obtained by each algorithm.

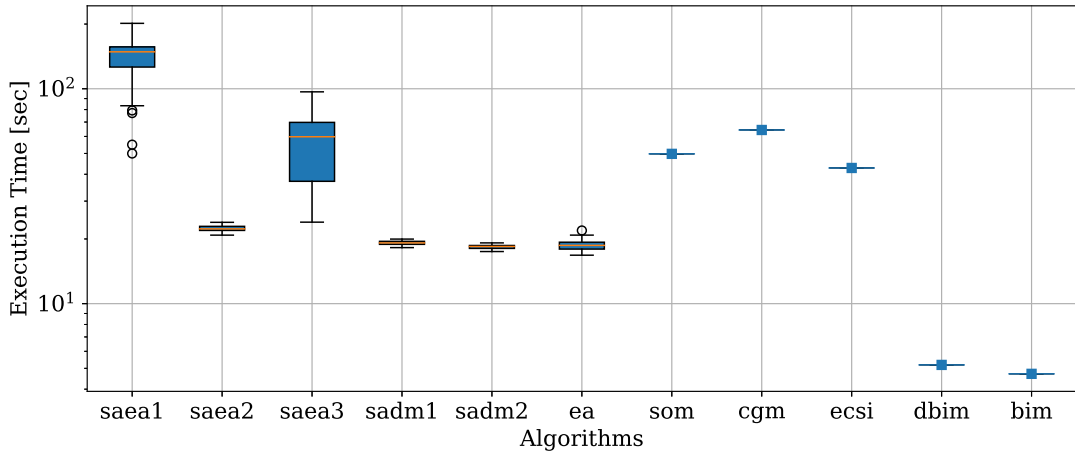


Figure 4.11: Box plot showing the execution time distribution of the set of algorithms considered for the multiple scatterers case study. The boxes represent the quartiles of the 30 executions of the stochastic algorithms, and the whiskers represent the minimum and maximum values. The deterministic algorithms are represented by individual points. The execution time results are presented in seconds.

had shorter execution times since fewer iterations were needed, which means the most expensive calculation was called fewer times during the algorithm execution. The median performances of the SADM2 and EA algorithms were quite similar, and no significant difference was detected based on the Welch Two Sample T-Test ( $p$ -value = 0.203). However, the medians of these two algorithms were below that of the other algorithms. By considering this indicator along with the  $\zeta_{EOE}$  and  $\zeta_S$  indicators, choosing between SADM2 and CGM in this case could be seen as a trade-off between reconstruction quality and execution time. In other words, while SADM2 may not achieve the same performance as CGM in shape and contrast estimation indicators, it can achieve slightly higher values in a much shorter time.

Figure 4.12 presents the surface of the objective function resulting from the transformation in a two-dimensional optimization problem, along with the location of the final solutions found by the algorithms in multiple runs. As the nonlinearity of the problem increased, the surface became less convex, and there was a certain grouping of solutions around the point  $T$ ,  $\chi = (0.75, 4)$  and a smaller one around  $(0.8, 5)$ . It is possible that the latter is a local minimum where some of the runs may have gotten stuck. The occurrence of more difficult to escape local minima may be more common as the problem becomes more non-linear or the contrast of the scatterers increases. The final solutions found for all algorithms were scattered, and only in the case of EA that solutions outside the lowest sublevel region were returned.

### 4.1.3 Non-Homogeneous Scatterer

The third case study presented in this work focuses on the imaging of a nonhomogeneous scatterer, which is a square of side length equals to  $\lambda_b$  with three different regions of contrast (0.4, 0.9, and 1.25) inside it. This scenario is relevant because it allows the qualitative identi-



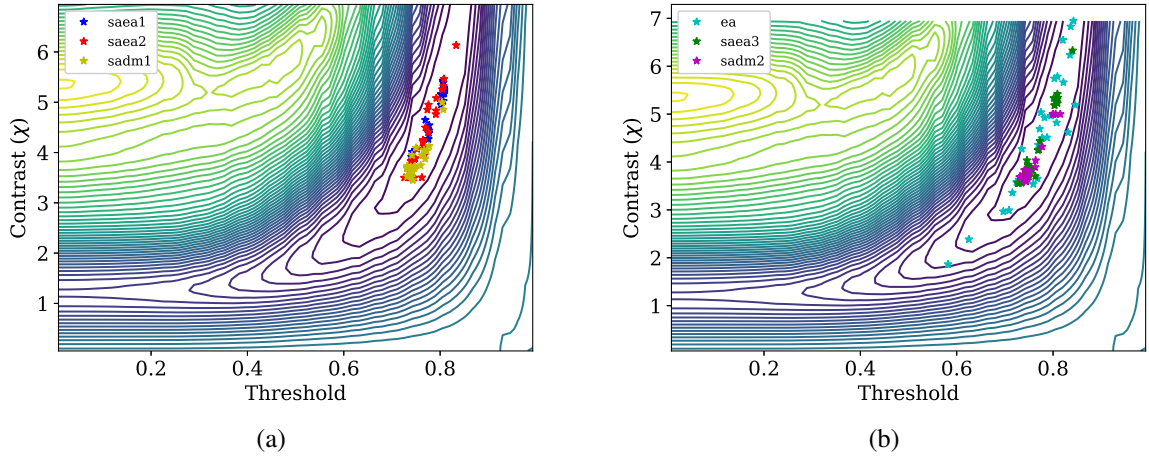


Figura 4.12: Surface of the two-dimensional optimization problem obtained from the transformation of the multiple scatterers case study and the final solutions obtained by different algorithms. Subfigure (a) shows the final solutions obtained by SAEA1, SAEA2, and SADM1 algorithms, while subfigure (b) shows the final solutions obtained by EA, SAEA3, and SADM2 algorithms.

fication of different levels of contrast using the OSM method. The inspiration for this study comes from a similar experiment presented by Bevacqua et al. (2020). The scatterer's detailed specifications can be found in the reference. Table 4.3 provides the specifications for measurement and imaging domains. Figure 4.13a illustrates the scatterer. The degree of non-linearity for this case is 1.396, which is above the threshold for cases where the Born Approximation can be applied. All settings for synthesizing the scattered field data are the same as in the previous case study.

Tabela 4.3: Parameters for problem specification of the nonhomogeneous scatterer case study.

$N_M$	$N_S$	$\lambda_b$	$R_O$	$L_X, L_Y$	$\epsilon_{rb}$
16	16	1 [m]	3.33 [ $\lambda_b$ ]	1.67 [ $\lambda_b$ ]	1

For this case study, adjustments were made to the algorithm configurations to more effectively explore their behavior. For the problem transformation-based algorithms, the maximum limit for the contrast variable was reduced to 3 since the maximum contrast in the true image is now 1.25. The stopping criterion was set to 60 evaluations. SAEA2 and EA utilized populations of 20 individuals as in the previous case study. Deterministic methods also underwent some modifications, such as CGM and ECSI using 50 iterations, DBIM using 3 iterations, BIM using 15 iterations, and SOM using 500 iterations with a cut-off index of 5.

Figure 4.13 presents the best reconstructions of the algorithms executed multiple times under the same criteria as the previous case study, as well as the images of the deterministic methods. The reconstructed images by the proposed algorithms (Figs. 4.13b-4.13g) were very similar to each other, suggesting that they were reconstructed from the same threshold level and

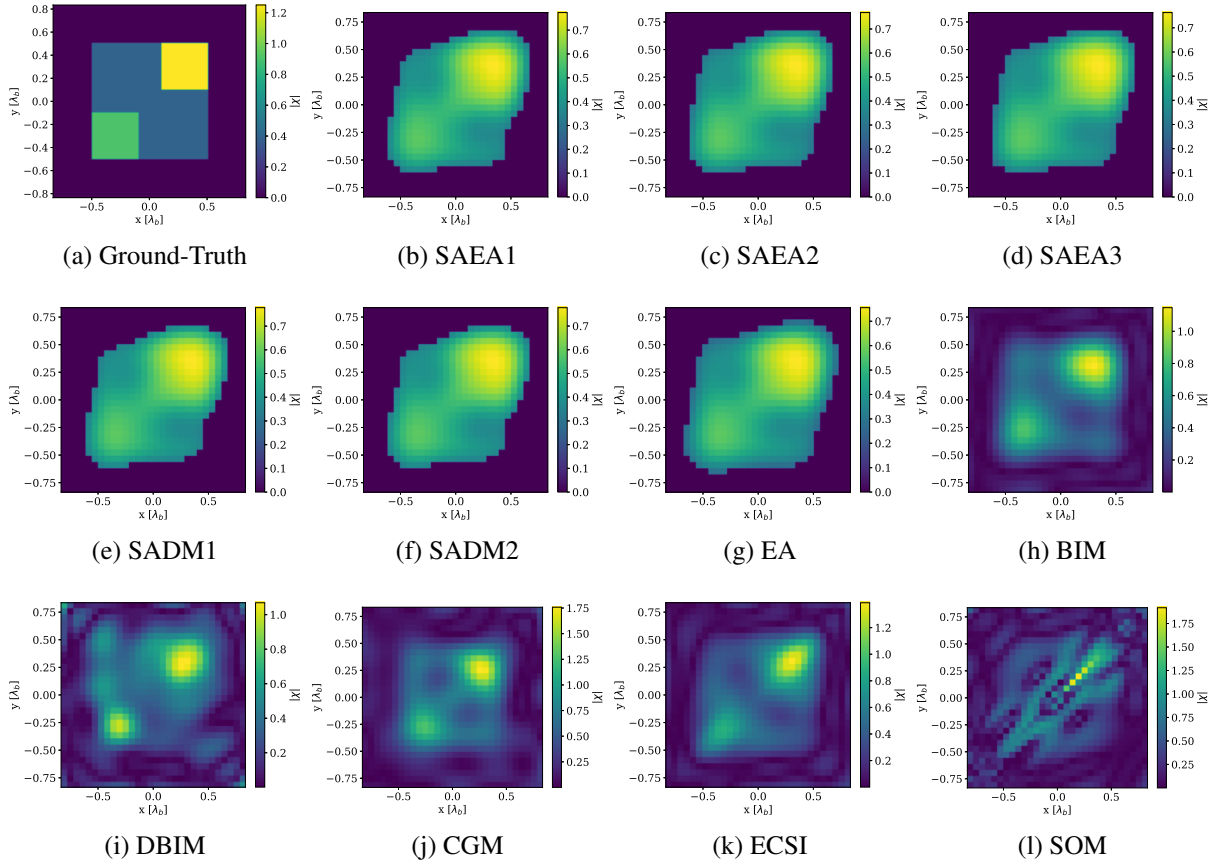


Figure 4.13: Comparison of image reconstructions using surrogate model-assisted algorithms and deterministic methods considering the nonhomogeneous scatterer case study: (a) shows the ground-truth image; (b), (c), and (d) depict the best image recovered by SAEA1, SAEA2, and SAEA3, respectively, in 30 execution according to  $\zeta_{\epsilon OE}$  indicator; (e), (f) and (g) show the best image recovered by SADM1, SADM2, and EA, respectively, in 30 execution according to  $\zeta_{\epsilon OE}$  indicator; (g) shows the image recovered by BIM, and (h) shows the image recovered by DBIM; finally, (i), (k), and (l) show the image recovered by CGM, ECSI, and SOM, respectively.

contrast estimation. However, the lowest level of contrast in the scatterer appeared to be proportionately higher than in the original image, resulting in a relatively blurred image with the second level. This may be attributed to the difficulty of the OSM method in estimating differences when they become distant from each other. As a result, the contrast was underestimated in all results since the increment in the contrast multiplication factor would represent an object with a higher average contrast and a higher error in the data equation.

BIM had a satisfactory reconstruction with a notable contour of the scatterer and well-estimated contrast levels. On the other hand, DBIM did not perform well. CGM and ECSI performed reconstructions that resembled the real scatterer, but with some distortions. In CGM, the contrast was overestimated, and in ECSI, the highest contrast region was slightly distorted. Finally, SOM did not perform well, possibly because the noise level greatly affected its performance in this scenario.

Figure 4.14 presents the convergence curves of the considered algorithms in this study.



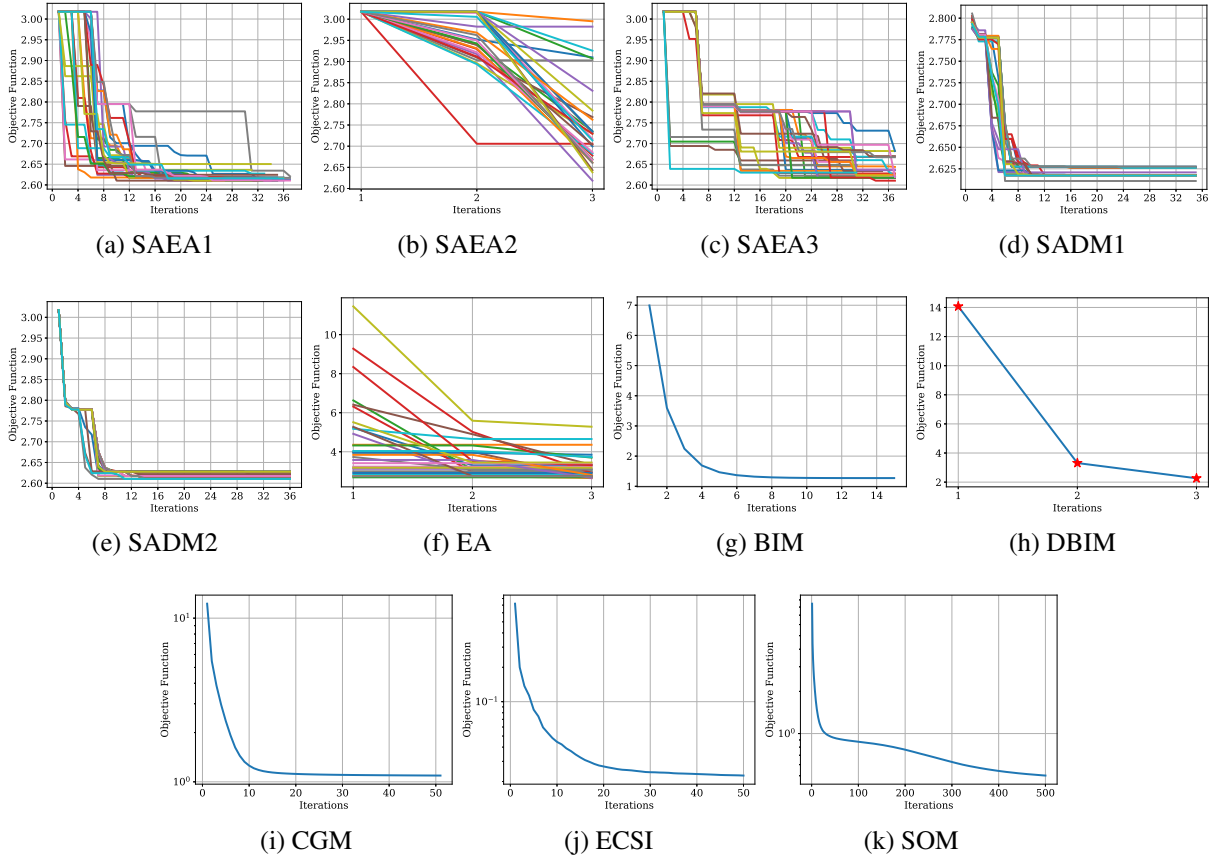


Figure 4.14: Convergence of the objective function for the nonhomogeneous scatterer case obtained by the stochastic and deterministic algorithms. (a) to (k) show the curves obtained by SAEA1, SAEA2, SAEA3, SADM1, SADM2, EA, BIM, DBIM, CGM, ECSI, and SOM algorithms, respectively. The x-axis represents the number of iterations, and the y-axis represents the value of the objective function of the correspondent algorithm.

The figure shows that BIM, CGM, ECSI, and SOM reached a reasonable level of stability in the convergence process and ended their executions, indicating that further iterations would not significantly improve the quality of the reconstructed images. Meanwhile, SADM1 and SADM2 had slight variations between runs, and although SAEA2 had 3 generations, some of the runs were able to arrive at solutions with low objective function values like the final solutions of SAEA1 and SAEA3.

The performance of the algorithms regarding the contrast estimation in the scatterer area was analyzed based on the results of indicator  $\zeta_{EOE}$  presented in Figure 4.15. Despite the fact that the image reconstructed by BIM was the most satisfactory, with a well-estimated contrast and reasonably clear scatterer contour, ECSI was the algorithm with the lowest contrast estimation error, although the shape was slightly distorted. Nevertheless, the difference in performance between BIM and ECSI was not significant, with approximately 1 [%/pixel]. The performance medians of the proposed algorithms were very similar, and the Kruskal-Wallis H-Test failed to reject the hypothesis of equality between them ( $p$ -value = 0.08). The performance difference between the proposed algorithms and ECSI was not too large, at around 3 [%/pixel].

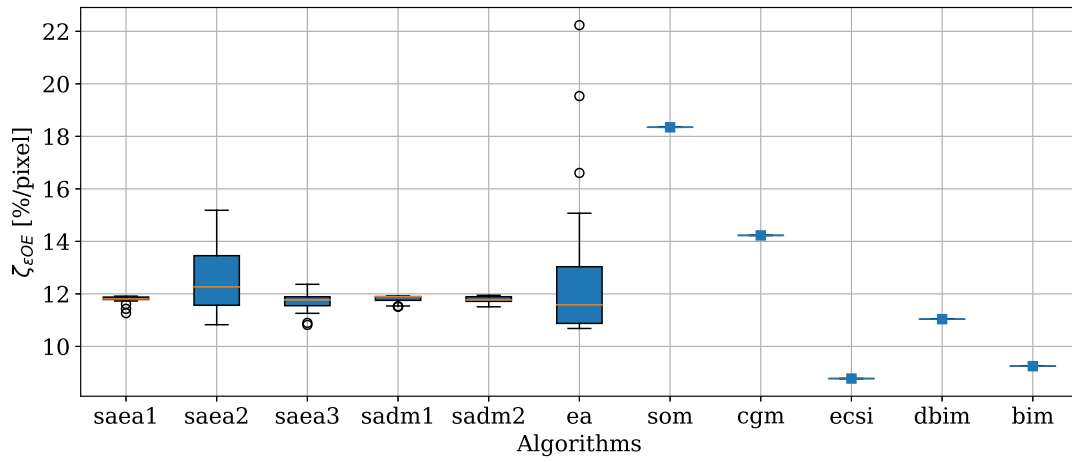


Figure 4.15: Performance of  $\zeta_{\epsilon OE}$  indicator for various algorithms in the nonhomogeneous scatterer case study. Boxplots show quartiles of 30 executions for stochastic algorithms, and the solid line represents the deterministic algorithms.

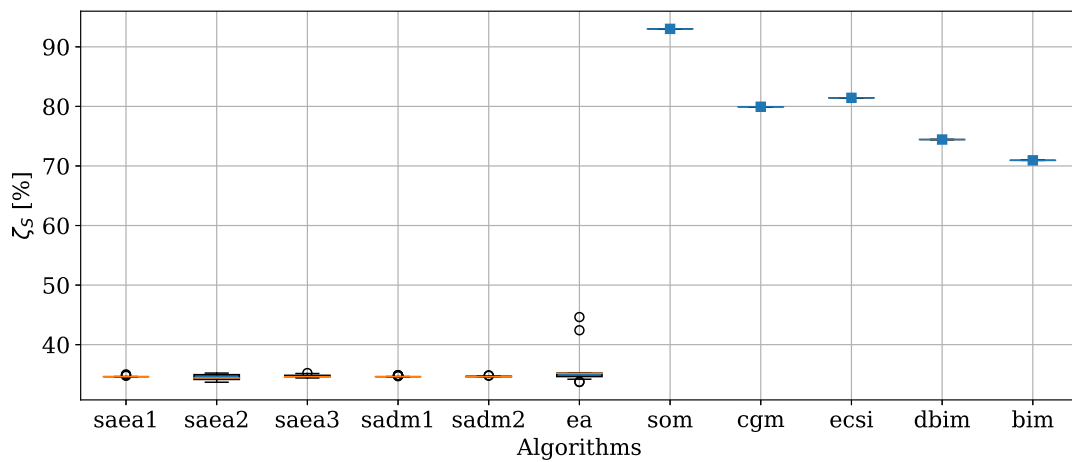


Figure 4.16: Performance of shape error estimation quantified by the  $\zeta_S$  indicator obtained by the set of algorithms considering the nonhomogeneous scatterer study. The boxes represent the quartiles of the 30 executions of the stochastic algorithms, while the other points indicate the obtained values by the deterministic ones. The shape error is calculated based on the ground-truth image and the reconstructed image obtained by each algorithm.

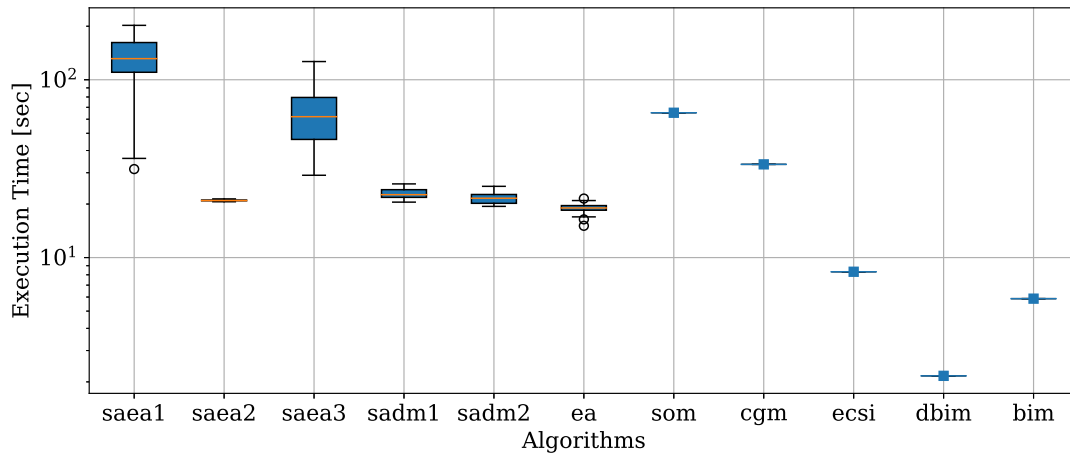


Figure 4.17: Box plot showing the execution time distribution of the set of algorithms considered for the nonhomogeneous scatterer case study. The boxes represent the quartiles of the 30 executions of the stochastic algorithms, and the whiskers represent the minimum and maximum values. The deterministic algorithms are represented by individual points. The execution time results are presented in seconds.

Figure 4.16 shows the results obtained by the algorithms considering the  $\zeta_S$  indicator. It was observed that the proposed algorithms outperformed the deterministic methods in terms of this indicator. However, it is interesting to note that BIM performed relatively worse than the other proposed algorithms, and this may be related to the difficulty of applying the indicator to significantly heterogeneous images. On the other hand, the proposed algorithms performed better possibly due to the smaller heterogeneity of the scatterer and the difference in respect to the background medium. Among the surrogate model-assisted algorithms, there was no evidence of a significant difference in the median performance of the indicator, as confirmed by the Kruskal-Wallis H-Test (p-value = 0.088). This suggests that the performance of the proposed algorithms in terms of this indicator is similar, and none of them stands out significantly from the others.

Figure 4.17 displays the running time of the algorithms analyzed in the study. As expected, some of the deterministic methods required less computational time than the proposed algorithms that use surrogate models. Among them, DBIM had the shortest time, thanks to the low number of iterations in which it can run without diverging. The second shortest time was taken by BIM, which was able to reconstruct the image adequately in a reasonably short time. Among the proposed algorithms, some executions had shorter times than others. Specifically, SAEA2, SADM1, SADM2, and EA required less time than SOM and CGM.

Figure 4.18 shows the surface of the objective function along with the location of the final solutions found by the algorithms in multiple runs. The surface of the objective function is similar to that obtained in the Austria profile case study (Fig. 4.6). The figure shows that only EA did not have all the final solutions within the sublevel region with the lowest value in the graph. This suggests that the EA algorithm may not be as efficient as the other algorithms

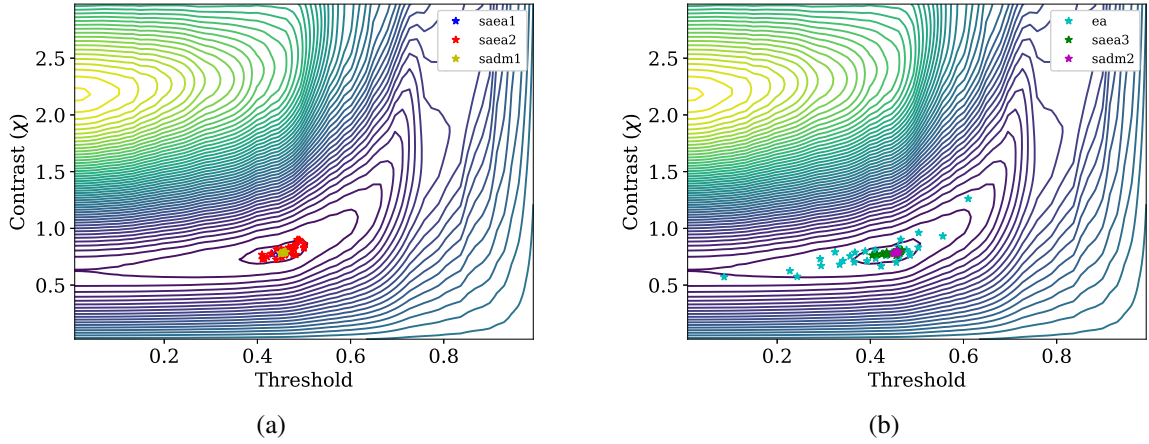


Figure 4.18: Surface of the two-dimensional optimization problem obtained from the transformation of the nonhomogeneous scatterer case study and the final solutions obtained by different algorithms. Subfigure (a) shows the final solutions obtained by SAEA1, SAEA2, and SADM1 algorithms, while subfigure (b) shows the final solutions obtained by EA, SAEA3, and SADM2 algorithms.

in finding the optimal solutions. In contrast, the final solutions of the SADM s were more concentrated, as expected because of their respective convergence graphs.

#### 4.1.4 Strong Scatterer

In the final case study, we explore the reconstruction of a strong scatterer, aiming to showcase the applicability of the proposed methodology in a more challenging scenario where traditional methods often struggle. The scatterer in focus is a 5-pointed star with a radius from the center to the farthest vertex approximately  $0.4\lambda_b$  (see Fig. 4.19a). To emphasize the difficulty, the object contrast has been set to 4, making it even more challenging to accurately reconstruct. Detailed information about the measurement and imaging domains can be found in Table 4.4, providing essential specifications for the experimental setup.

To ensure higher precision in data synthesis, we increased the image resolution to  $120 \times 120$ . This resolution enhancement was chosen to minimize errors during the synthesis of the scattered field, considering the complexity of the problem at hand. Other parameters for data synthesis remained consistent with those used in the previous case studies.

The DNL for this particular problem is notably high, measuring 7.39. Such a high DNL value indicates the significant nonlinearity of the problem, further accentuating the challenge in accurately reconstructing the strong scatterer. The combination of the intricate scatterer shape and the high object contrast poses a substantial test for the proposed methodology.

In order to tackle the increased complexity of the problem, several adjustments were made to the operating parameters of both the surrogate model-assisted algorithms and the deterministic methods. These modifications aimed to enhance the performance and adaptability of the algorithms to the more nonlinear nature of the scenario.

Tabela 4.4: Parameters for problem specification of the strong scatterer case study.

$N_M$	$N_S$	$\lambda_b$	$R_O$	$L_X, L_Y$	$\varepsilon_{rb}$
50	50	1 [m]	5 [ $\lambda_b$ ]	1 [ $\lambda_b$ ]	1

For the surrogate model-assisted algorithms, the upper bound of the contrast variable was set to 7, reflecting the higher contrast range present in the problem. Additionally, the maximum number of iterations for the MoM-CG-FFT in the evaluation of solutions remained at 20, despite this representing a greater error in the field approximation. This choice was deliberate to showcase the methodology's robustness even in challenging scenarios, where highly precise field calculations are not necessary. Furthermore, the maximum number of evaluations, serving as a stopping criterion, was increased to 80. To provide a more comprehensive initial sample, the number of solutions was increased to 36. These adjustments, while increasing the computational cost, were essential to address the growing complexity of the problem and obtain accurate results.

The remaining parameters for the surrogate model-assisted algorithms remained consistent with the previous study, ensuring continuity and comparability. Similarly, adjustments were made to the deterministic methods. For SOM and CGM, the maximum number of iterations was extended to 1000, allowing for more comprehensive convergence. ECSI iterations were adjusted to 50. BIM iterations were set to 4, while DBIM iterations were limited to 2, considering the nature of the problem and the desired accuracy of the reconstructions. The number of iterations of the last three algorithms were chosen according to their own limitation in this scenario.

The Fig. 4.19 provides a visual representation of the best reconstructions obtained from the stochastic algorithms, as evaluated by the  $\zeta_{EOE}$  indicator, alongside the reconstructions produced by the deterministic algorithms. It is noteworthy that the best images generated by the algorithms based on problem transformation exhibited variations in both contrast estimation and the application of the thresholding operator. Despite these variations, the reconstructed images still bear some resemblance to the geometry of the original image. This suggests that the qualitative method was able to capture certain structural characteristics despite the challenges posed by the problem. However, the contrast was underestimated in some cases. On the other hand, the deterministic algorithms failed to achieve satisfactory image reconstructions, although CGM was able to detect a region similar to a star with reasonable contrast estimation close to the boundaries and considerable overestimation at the center.

Figure 4.20 provides a visual representation of the convergence behavior of the objective function for all algorithms employed in the study. Similar to the observations made in the case study involving multiple scatterers, this analysis reveals notable differences in the convergence patterns of the SADMs algorithms across multiple executions. This finding suggests that as the problem becomes more non-linear, the behavior of these algorithms tends to exhibit stochastic

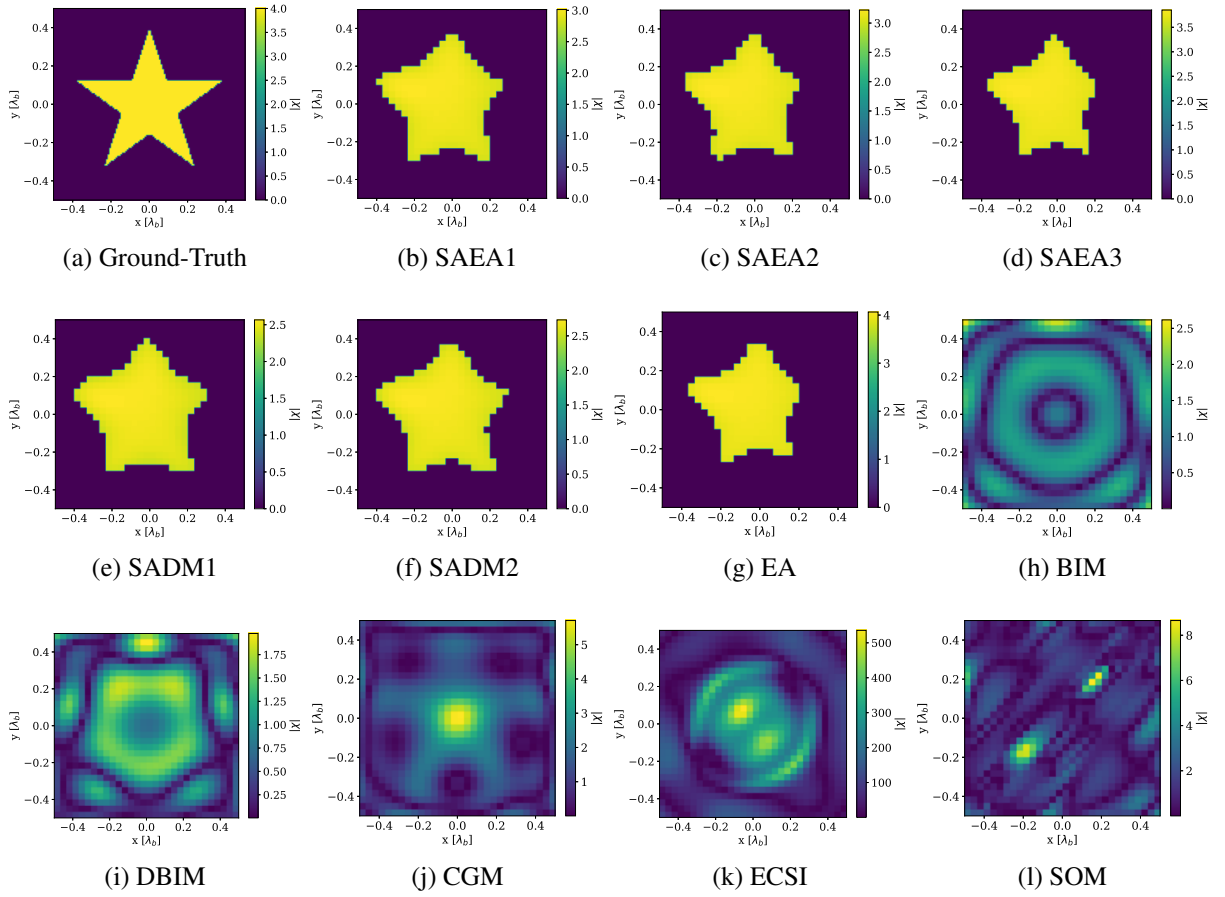


Figure 4.19: Comparison of image reconstructions using surrogate model-assisted algorithms and deterministic methods considering the strong scatterer case study: (a) shows the ground-truth image; (b), (c), and (d) depict the best image recovered by SAEA1, SAEA2, and SAEA3, respectively, in 30 execution according to  $\zeta_{EOE}$  indicator; (e), (f) and (g) show the best image recovered by SADM1, SADM2, and EA, respectively, in 30 execution according to  $\zeta_{EOE}$  indicator; (g) shows the image recovered by BIM, and (h) shows the image recovered by DBIM; finally, (i), (k), and (l) show the image recovered by CGM, ECSI, and SOM, respectively.

characteristics.

Notably, ECSI exhibits an atypical behavior characterized by oscillations in its convergence curve. This observation highlights the algorithm's limitation when confronted with highly non-linear scenarios. The oscillatory nature of the convergence indicates the algorithm's struggle to converge to a stable and accurate solution, impairing its performance in such challenging scenarios.

On the other hand, the convergence curves of the CGM and SOM algorithms exhibit a different pattern. These algorithms demonstrate a stabilized behavior towards the end of the run, suggesting that further iterations would have minimal impact on the reconstructed images depicted in Figs. 4.19j and 4.20k. This stabilization indicates that the algorithms have reached a reasonably stable state, and additional iterations would not significantly enhance the quality of the reconstructions.

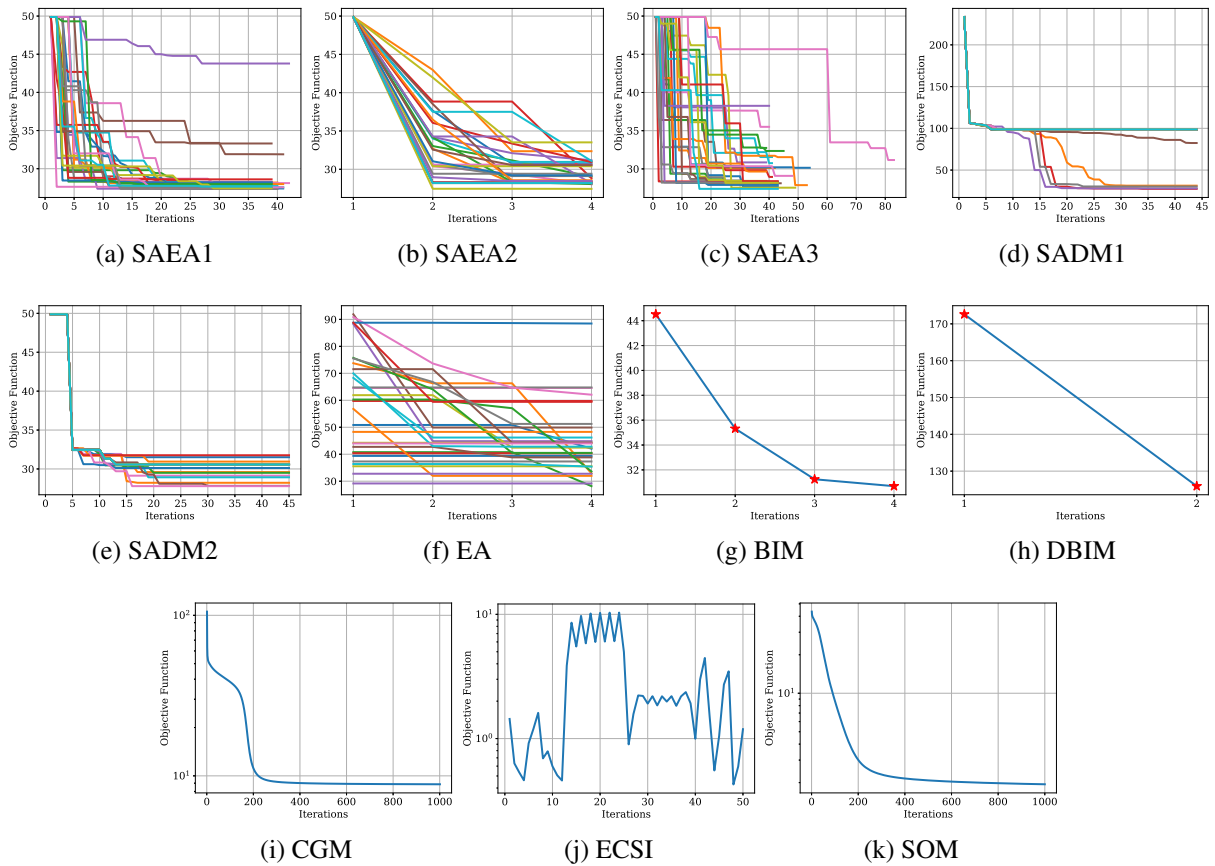


Figure 4.20: Convergence of the objective function for the strong scatterer case obtained by the stochastic and deterministic algorithms. (a) to (k) show the curves obtained by SAEA1, SAEA2, SAEA3, SADM1, SADM2, EA, BIM, DBIM, CGM, ECSI, and SOM algorithms, respectively. The x-axis represents the number of iterations, and the y-axis represents the value of the objective function of the correspondent algorithm.

Initialization by the Backpropagation algorithm and the Born Approximation can be very bad in strong scattering scenarios, which can compromise all convergence of the deterministic algorithms. Therefore, one of the questions that may arise from the results is the impact of starting with the OSM qualitative method solution, i.e., how the deterministic algorithms would perform if they also received the image obtained by OSM as initial guess.

Figure 4.21 showcases the reconstructions and convergence behavior of the deterministic algorithms when initialized with the normalized image from the qualitative method. Interestingly, the initialization strategy does not yield improvements for BIM, ECSI, and SOM algorithms. This indicates that relying solely on the qualitative method's image is insufficient to ensure better performance of these methods in such challenging scenarios. However, the DBIM and CGM algorithms demonstrate similar images resembling a smaller star, with a contrast estimate comparable to the surrogate model-assisted methods.

Analyzing the respective convergence graphs, it can be observed that the CGM image would not undergo significant changes beyond 1000 iterations, suggesting limited improvement in eliminating middle background noises. On the other hand, DBIM exhibits divergence with



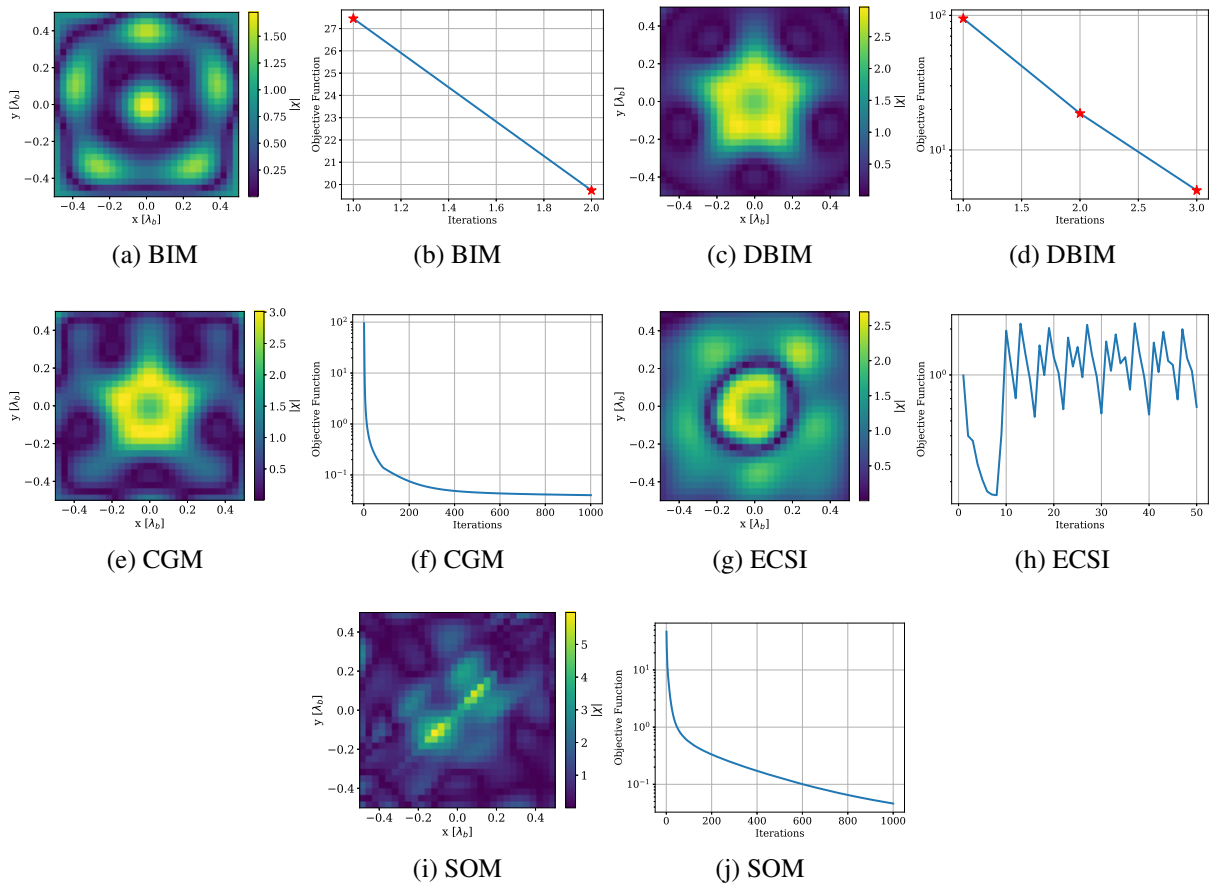


Figure 4.21: Reconstruction and convergence of the objective function for BIM (a)-(b), DBIM (c)-(d), CGM (e)-(f), ECSI (g)-(h), and SOM (i)-(j) algorithms with initial guess from the qualitative method.



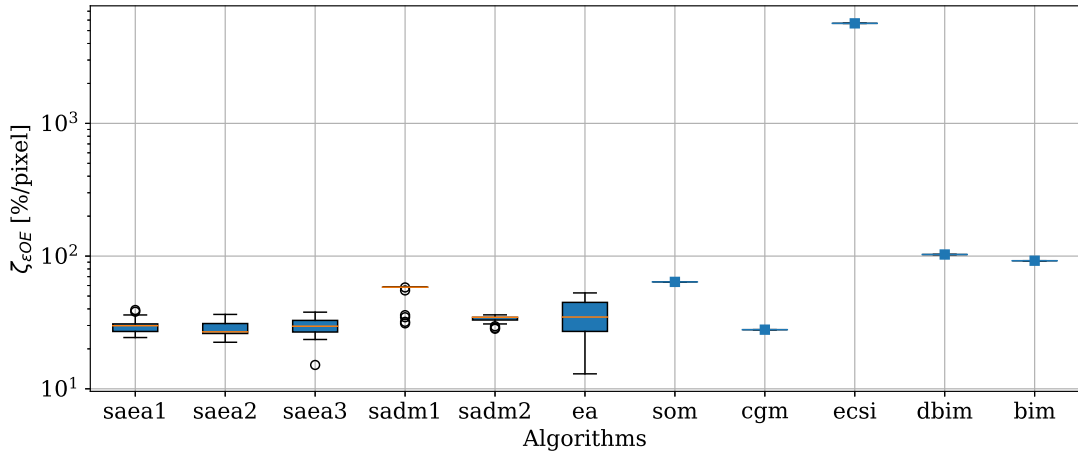


Figure 4.22: Performance of  $\zeta_{\epsilon OE}$  indicator for various algorithms in the strong scatterer case study. Boxplots show quartiles of 30 executions for stochastic algorithms, and the solid line represents the deterministic algorithms.

additional iterations. These findings highlight the importance of transforming the problem into a two-variable optimization framework, which proves to be the most effective approach for leveraging the reconstructed image provided by the qualitative method.

In Fig. 4.22, we can observe the results of the  $\zeta_{\epsilon OE}$  indicator obtained by the different algorithms. Although the CGM algorithm did not produce reconstructions as visually clear as the proposed algorithms, its performance in terms of the contrast error indicator was comparable to the median value of most surrogate model-assisted algorithms. Despite the slightly blurred nature of its reconstructions, CGM was able to provide a reasonable estimation of the contrast value in the object region.

To further analyze the performance of the algorithms, a statistical comparison was conducted through Kruskal-Wallis H-Test. Comparing the median performance of the SAEAs and SADM2, evidence of a difference in performance was found ( $p\text{-value} < 10^{-6}$ ). Post-hoc comparisons revealed that the difference in performance is found when each SAEA is compared against SADM2 ( $p\text{-value} < 0.001$  in each case). In each case, the performance of the corresponding SAEA formulation overcame SADM2's performance.

In Fig. 4.23, it is observed the results of the  $\zeta_S$  indicator obtained by the algorithms. The median values of the SAEAs were now found to be lower than the median value achieved by the CGM algorithm. No evidence for differences in the median performance among the SAEAs formulation was found according to the Kruskal-Wallis H-Test ( $p\text{-value} = 0.1983$ ). Furthermore, the Wilcoxon signed-rank test detected evidence for a worst median performance of SADM2 when compared against CGM.

Figure 4.24 displays the running time results of the algorithms used in the study. Among the algorithms, ECSI, DBIM, and BIM exhibited the lowest running times. This can be attributed to their poor convergence, which led to a lower number of iterations required for completion.

Notably, there is a significant difference in running time between the SAEA2 and SADM2

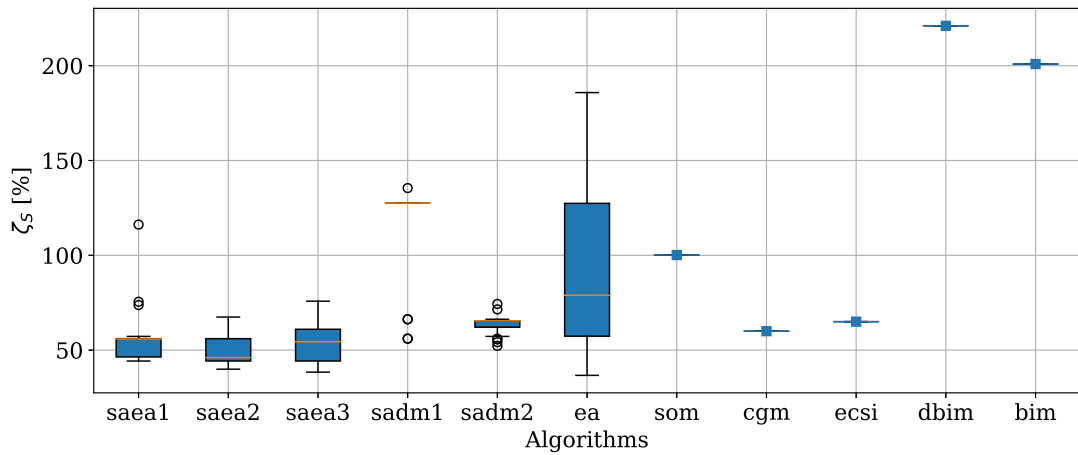


Figura 4.23: Performance of shape error estimation quantified by the  $\zeta_S$  indicator obtained by the set of algorithms considering the strong scatterer study. The boxes represent the quartiles of the 30 executions of the stochastic algorithms, while the other points indicate the obtained values by the deterministic ones. The shape error is calculated based on the ground-truth image and the reconstructed image obtained by each algorithm.

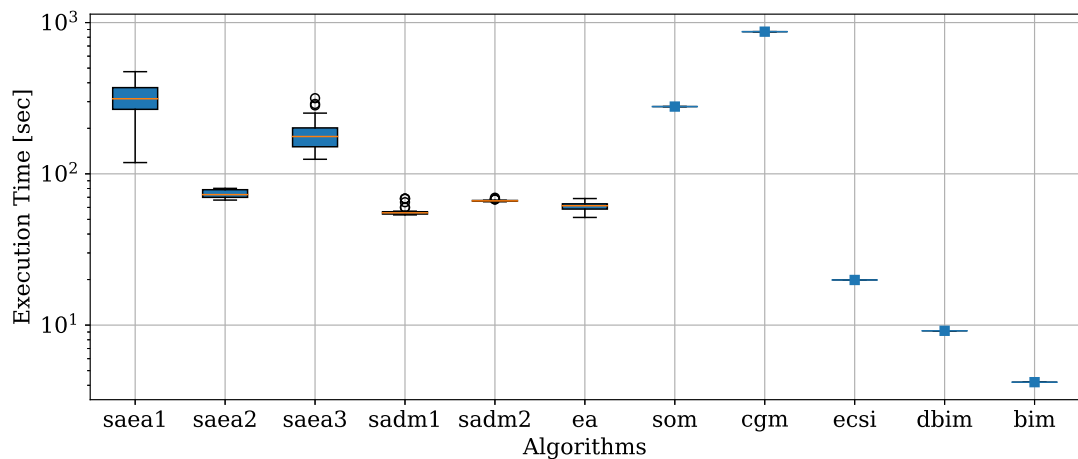


Figura 4.24: Box plot showing the execution time distribution of the set of algorithms considered for the strong scatterer case study. The boxes represent the quartiles of the 30 executions of the stochastic algorithms, and the whiskers represent the minimum and maximum values. The deterministic algorithms are represented by individual points. The execution time results are presented in seconds.

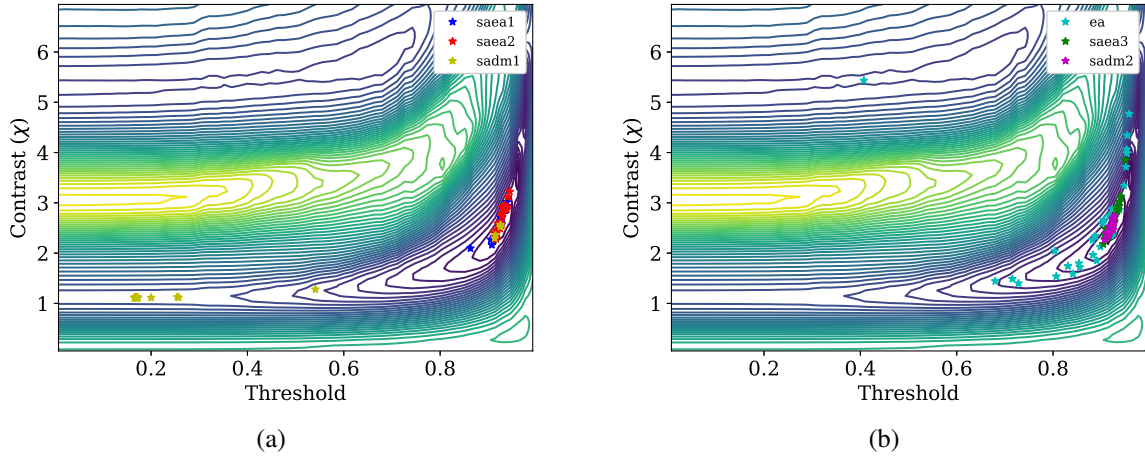


Figura 4.25: Surface of the two-dimensional optimization problem obtained from the transformation of the strong scatterer case study and the final solutions obtained by different algorithms. Subfigure (a) shows the final solutions obtained by SAEA1, SAEA2, and SADM1 algorithms, while subfigure (b) shows the final solutions obtained by EA, SAEA3, and SADM2 algorithms.

algorithms when compared against CGM. It is important to note that although CGM achieved a better value for the  $\zeta_{\epsilon OE}$  indicator, the other two algorithms, SAEA2 and SADM2, demonstrated the ability to produce satisfactory reconstructions within a significantly shorter time frame.

Figure 4.25 showcases the surface of the objective function resulting from the transformation in a two-dimensional optimization problem, providing insights into the behavior of the algorithms and the location of their final solutions in multiple runs. Upon observing the surface, it becomes apparent that the objective function exhibits two macro basins of attraction.

The distribution of the final solutions found by the algorithms reveals a scattering pattern, suggesting the location of the global optimum and the presence of small basins of attraction associated with local minima. Notably, such region appears to be very narrow, indicating a challenging optimization scenario. Therefore, the algorithms encountered greater difficulty converging to a single point in this particular instance. Furthermore, it is important to consider that the contrast value in the region of the global optimum is significantly underestimated. This outcome aligns with the expected behavior of qualitative methods when reconstructing the shape of strong scatterers, as demonstrated in this case study.

## 4.2 Benchmarking

This section presents a benchmarking experiment designed to evaluate the performance of the algorithms proposed in this thesis. While studying specific instances can provide valuable insights into experimental effects, a broader study with a larger number of instances enables a more comprehensive evaluation. To ensure a thorough analysis of the methods' performance, it is crucial to identify and consider influential factors when designing the experiment.

The experiment aims to isolate certain factors while varying others of interest, creating a

diverse range of test scenarios represented by the selected problem samples. By employing a set of quality indicators, the performance of the techniques can be objectively measured and rigorously compared. The study focuses on evaluating the quality of contrast estimation and shape recovery while varying the contrast level of objects. Additionally, the number of evaluations required by each algorithm will be investigated to identify the most efficient approaches.

Unlike the case studies that examine specific instances, this benchmarking experiment encompasses multiple test sets. Within each set, scatterers possess a fixed contrast value, while their position and geometry vary. As a result, each set represents a collection of scatterers with the same contrast value but different configurations and positions within the images.

By analyzing the median behavior through statistical analysis, valuable insights into performance can be derived. This approach enables the identification of the strengths and weaknesses of the proposed techniques in a more robust and comparative manner, facilitating informed conclusions about their efficacy.

#### 4.2.1 Test Sets and Algorithms Parameters Considerations

The overview of the general settings and parameters used in the generation of the test sets is presented as follows. The formulation and generation process followed the *TestSet* class structure implemented in the *eispy2d* library. Five test sets have been created where each set consisted of instances with a single scatterer, all sharing the same contrast value.

The selected contrast levels for the test sets were 0.5, 1, 2, 3, and 4, representing a range of different scattering strengths. The scatterers are random polygons that varied in geometry and position within the image, ensuring diversity in the test scenarios. Additionally, the size of the scatterers was controlled, with the size parameter defined as the distance from the center of the scatterer to its farthest vertex. For each contrast level, a specific size value was assigned. The size values for each contrast level, in increasing order of contrast, were 1.06, 0.8, 0.41, 0.33, and 0.27  $[\lambda_b]$ .

The choice of object size values was based on an extensive preliminary study that examined the accuracy of the shape reconstruction by the qualitative method for different scatterer sizes at a given contrast value. The selected sizes represent the optimal scenarios for applying OSM in terms of shape quality.

Tabela 4.5: Parameters for measurement and imaging domains specification of benchmark study.

$N_M$	$N_S$	$R_O$	$\lambda_b$	$\epsilon_{rb}$
20	20	5 $[\lambda_b]$	1 [m]	1

Table 4.5 presents specifications of the measurement and imaging domains used in the test sets. The size of the imaging domain ( $L_X, L_Y$ ) varied depending on the contrast value, with

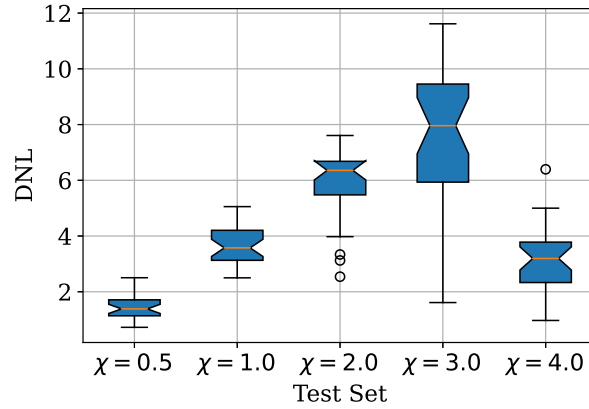


Figura 4.26: Box plot depicting the DNL across test sets: Test Set 1 (Contrast: 0.5), Test Set 2 (Contrast: 1), Test Set 3 (Contrast: 2), Test Set 4 (Contrast: 3), and Test Set 5 (Contrast: 4). The box plots showcase the distribution of non-linearity values, with the notches roughly indicating differences between medians. Non-overlapping notches mean significant differences between the medians.

smaller domain size corresponding to higher contrast levels. The specific imaging domain sizes for each set, in ascending order of contrast values, were  $4 \times 4$ ,  $4 \times 4$ ,  $2 \times 2$ ,  $2 \times 2$ , and  $1 \times 1$  [ $\lambda_b^2$ ].

Each test set consisted of 30 individual tests. To generate the scattered field data, we employed the MoM-CG-FFT forward solver with 5000 iterations and a tolerance level of 0.001. Additionally, a noise level of 20 [%/sample] was added to all synthesized data to simulate realistic measurement conditions. Finally, the original images of each test had a resolution of  $120 \times 120$  pixels, ensuring sufficient detail for accurate analysis and evaluation.

Fig. 4.26 presents the distribution of the DNL for each test set, showcasing the variability in DNL despite the same contrast level across tests. The confidence interval for the median in each case is also displayed. The diversity in scatterer geometry within each set contributes to the observed variability in DNL. Notably, the median DNL increases with contrast level up to  $\chi = 3$ , after which a significant decrease in scatterer size for the  $\chi = 4$  contrast set leads to a smaller median DNL. However, it is important to note that even in this case, the DNL remains above 1, indicating the challenging nature of the problem. To further explore the range of DNL values, Fig. 4.27 showcases the instances with the smallest and largest DNL within each test set.

For this comparative evaluation, only algorithms assisted by surrogate models will be considered. By narrowing down the scope to these specific methods, we can delve deeper into understanding their unique characteristics and distinguishing features. This selection allows us to explore the differences between the proposed algorithms and observe their effectiveness and suitability.

To ensure a fair evaluation, the algorithms will be configured with identical parameters across all test sets. The maximum value of the contrast variable has been set to 7 in all cases, providing a wide range of contrast levels that covers each test set adequately. Additionally,

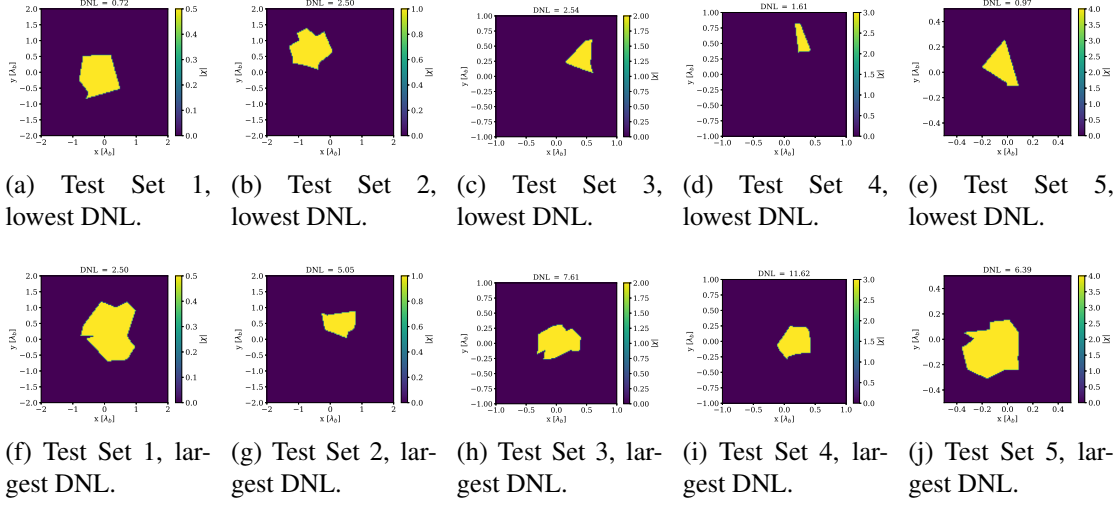


Figure 4.27: Instances with the lowest and largest DNL for each test set. Figures (a) to (e) display the instances with the lowest DNL for Test Sets 1 to 5, respectively. Conversely, figures (f) to (j) showcase the instances with the largest DNL for the corresponding test sets.

the stopping criterion for the algorithms will be based on either a lack of improvement for 10 iterations or a maximum of 1000 evaluations. This criterion ensures that the algorithms have a reasonable time frame to converge or identify a lack of progress.

In all test sets, the number of initial samples used for model generation will be fixed at 36. This choice ensures a reasonable number of samples to train the surrogate models accurately in the hardest scenario. Furthermore, for SAEAs, a population size of 20 individuals has been determined. This population size was chosen aiming a balance between exploration and exploitation within the evolutionary search process.

## 4.2.2 Discussion

In this subsection, the results of the benchmarking study will be presented and discussed. The study aimed to evaluate the performance of different algorithms based on diverse performance indicator data. These indicators were obtained at the end of the algorithm executions and will be organized in a boxplot format.

For each algorithm, it is showcased the performance evolution based on the contrast value that defines each test set. To better understand the performance evolution, a straight line obtained through linear regression will be displayed. This line represents an estimate of the expectation of the average performance as the contrast value increases. By considering the averages in the test sets of an algorithm, we can approximate the average performance along the growth of the contrast.

It's important to note that each algorithm was executed 30 times for each test in each set. This approach was taken to ensure reliable and consistent results. To determine the final performance of an algorithm in a specific test, we will consider the average of the respective

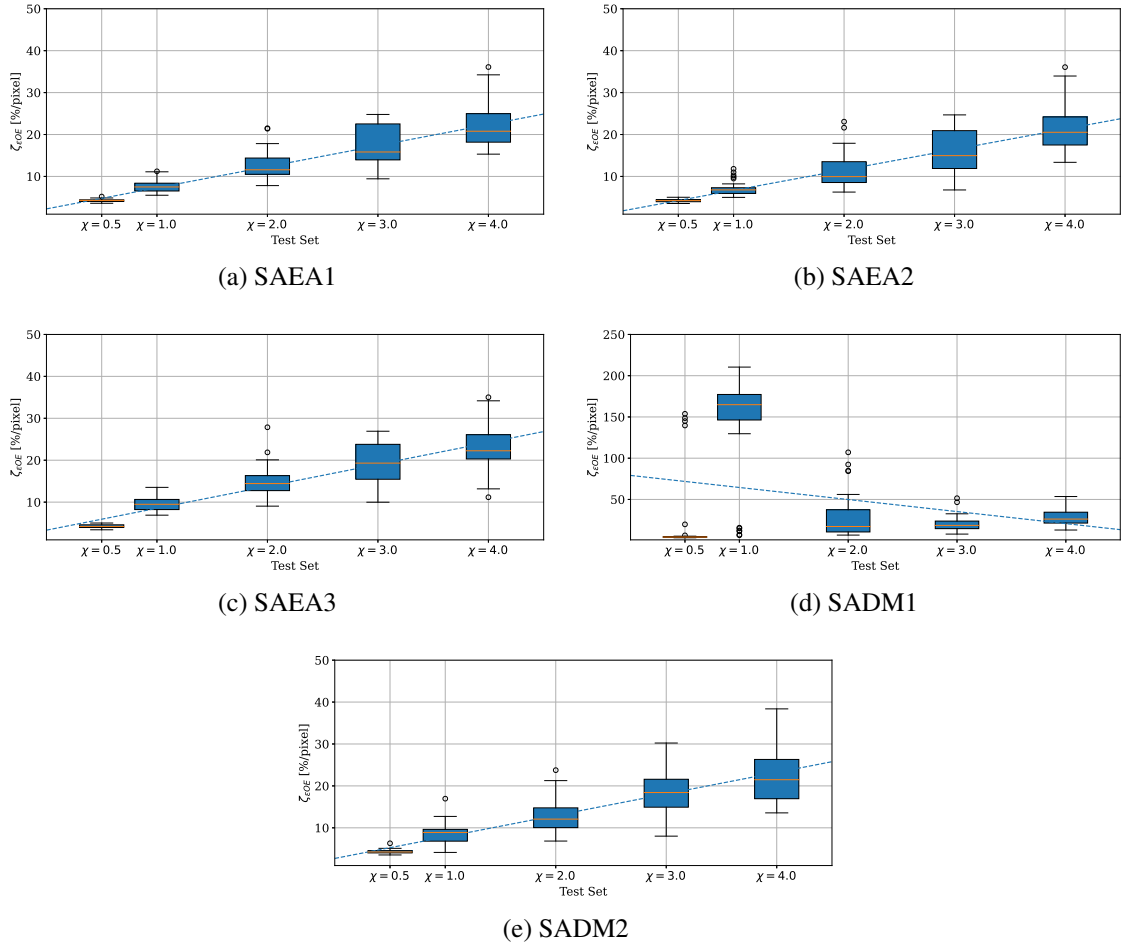


Figure 4.28: Evolution of the contrast estimation error ( $\zeta_{\epsilon OE}$ ) in the object region for the proposed algorithms (a)-(e): SAEA1, SAEA2, SAEA3, SADM1, and SADM2, respectively. Additionally, a straight line obtained through linear regression is overlaid on each subfigure. This line represents the estimated evolution of the average performance, based on the means of each test set.

indicator based on these 30 executions. This averaging process helps mitigate the impact of any outliers or random variations that might occur during individual executions. In the same fashion, 30 executions will return 30 recovered images for each test and the final one will be chosen as the one which has the median value according to  $\zeta_{\epsilon OE}$  indicator.

Figure 4.28 displays the contrast estimation error indicator in the object region for each algorithm. The y-axis range is consistent among all algorithms, except for SADM1. Due to significantly larger errors obtained by SADM1, the range had to be increased for this particular algorithm.

The distinctive performance of SADM1, specially on the test set  $\chi = 1$ , raises curiosity. To investigate this occurrence, the reconstructed images generated by SADM1 for each test in the set were analyzed. Figure 4.29 provides visual evidence, presenting the true image from the first test set alongside the corresponding reconstruction by the method. It is apparent that the contrast estimate in SADM1's reconstruction is much higher than the true value, nearing

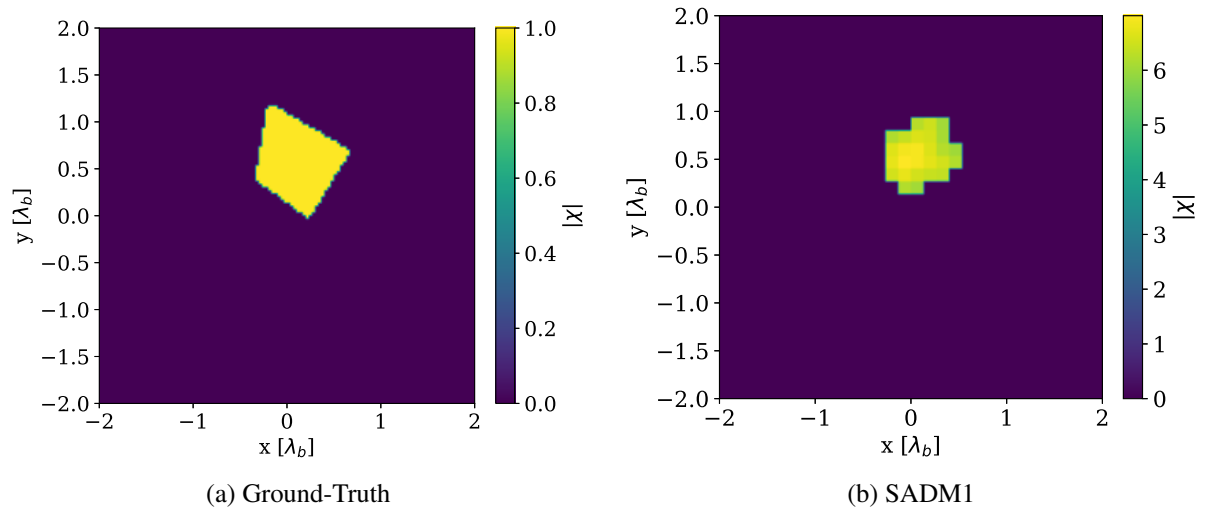


Figure 4.29: (a) Ground-truth and (b) recovered images by SADMM1 in test 1 for Test Set  $\chi = 1$ . It is evident from the figure that SADMM1 has overestimated the contrast of the object in its reconstruction.

the maximum limit of the contrast variable. This effect persists across all reconstructions of the algorithm in the same test set. Thus, these results suggest that the algorithm had a tendency to become trapped in a local minimum region, unlike the other algorithms. This behavior may be associated with the performance of the Differential Evolution (DE) as a solution initialization strategy.



Tabela 4.6: P-values for posthoc multiple pairwise comparisons considering the  $\zeta_{OE}$  indicator, with the compatible statistical test for each test set. The significance level has been corrected using the Bonferroni method, resulting in 0.0083. Detected differences are indicated in bold format. Confidence intervals are compute for means when Paired T-Test are evaluated and for medians when the Wilcoxon Signed-Rank Test is evaluated.

Pairs	$\chi = 0.5$				$\chi = 1$				$\chi = 2$				$\chi = 3$			
	Wilcoxon		Paired T-Test		Wilcoxon		Paired T-Test		Wilcoxon		Paired T-Test		Wilcoxon		Paired T-Test	
	p-value	Conf. In.	p-value	Conf. In.	p-value	Conf. In.	p-value	Conf. In.	p-value	Conf. In.	p-value	Conf. In.	p-value	Conf. In.	p-value	Conf. In.
SAEA1-SAEA2	0.2988	(-0.031, 0.034)	<b>&lt;0.0001</b>	(0.322, 0.895)	<b>&lt;0.0001</b>	(0.675, 1.576)	<b>&lt;0.0001</b>	(0.4, 1.484)	<b>&lt;0.0001</b>	(0.675, 1.576)	<b>&lt;0.0001</b>	(0.4, 1.484)	<b>&lt;0.0001</b>	(0.675, 1.576)	<b>&lt;0.0001</b>	(0.4, 1.484)
SAEA1-SAEA3	0.1706	(0.012, 0.124)	<b>&lt;0.0001</b>	(-2.5, -1.33)	<b>&lt;0.0001</b>	(-2.165, -0.916)	<b>&lt;0.0001</b>	(-2.574, -1.019)	<b>&lt;0.0001</b>	(-2.165, -0.916)	<b>&lt;0.0001</b>	(-2.574, -1.019)	<b>&lt;0.0001</b>	(-2.165, -0.916)	<b>&lt;0.0001</b>	(-2.574, -1.019)
SAEA1-SADM2	0.0577	(-0.089, 0.002)	<b>0.003</b>	(-1.99, -0.132)	0.6702	(-0.804, 0.842)	0.2054	(-1.35, 0.862)	0.6702	(-0.804, 0.842)	0.2054	(-1.35, 0.862)	0.6702	(-0.804, 0.842)	0.2054	(-1.35, 0.862)
SAEA2-SAEA3	0.2988	(-0.017, 0.148)	<b>&lt;0.0001</b>	(-3.18, -1.87)	<b>&lt;0.0001</b>	(-4.152, -2.3)	<b>&lt;0.0001</b>	(-4.301, -2.237)	<b>&lt;0.0001</b>	(-4.152, -2.3)	<b>&lt;0.0001</b>	(-4.301, -2.237)	<b>&lt;0.0001</b>	(-4.152, -2.3)	<b>&lt;0.0001</b>	(-4.301, -2.237)
SAEA2-SADM2	0.0164	(-0.109, -0.009)	<b>&lt;0.0001</b>	(-2.71, -0.634)	<b>0.0008</b>	(-1.542, -0.063)	<b>0.0015</b>	(-2.494, 0.137)	<b>0.0008</b>	(-1.542, -0.063)	<b>0.0015</b>	(-2.494, 0.137)	<b>0.0008</b>	(-1.542, -0.063)	<b>0.0015</b>	(-2.494, 0.137)
SAEA3-SADM2	0.1347	(-0.21, -0.023)	0.023	(-0.153, 1.86)	0.0113	(0.912, 3.128)	0.1642	(-0.886, 2.103)	0.0113	(0.912, 3.128)	0.1642	(-0.886, 2.103)	0.0113	(0.912, 3.128)	0.1642	(-0.886, 2.103)

Tabela 4.7: P-values for posthoc multiple pairwise comparisons obtained by Wilcoxon Signed-Rank tests considering the  $\zeta_S$  indicator. The significance level has been corrected using the Bonferroni method, resulting in 0.0083. Detected differences are indicated in bold format. The confidence interval for medians is also presented.

Pairs	$\chi = 0.5$				$\chi = 1$				$\chi = 2$				$\chi = 3$				$\chi = 4$			
	Wilcoxon		Paired T-Test		Wilcoxon		Paired T-Test		Wilcoxon		Paired T-Test		Wilcoxon		Paired T-Test		Wilcoxon		Paired T-Test	
	p-value	Conf. In.	p-value	Conf. In.	p-value	Conf. In.	p-value	Conf. In.	p-value	Conf. In.	p-value	Conf. In.	p-value	Conf. In.	p-value	Conf. In.	p-value	Conf. In.	p-value	Conf. In.
SAEA1-SAEA2	<b>&lt;0.0001</b>	(0.34, 0.92)	<b>&lt;0.0001</b>	(0.49, 1.09)	<b>&lt;0.0001</b>	(1.02, 2.04)	<b>0.0002</b>	(0.67, 2.01)	<b>0.0002</b>	(1.02, 2.04)	<b>0.0002</b>	(0.67, 2.01)	<b>0.0002</b>	(1.02, 2.04)	<b>0.0002</b>	(0.67, 2.01)	<b>0.0002</b>	(1.02, 2.04)	<b>0.0002</b>	(0.67, 2.01)
SAEA1-SAEA3	<b>0.0002</b>	(-1.32, -0.49)	<b>&lt;0.0001</b>	(-5.38, -3.52)	<b>&lt;0.0001</b>	(-2.46, -1.34)	<b>&lt;0.0001</b>	(-3.16, -1.28)	<b>&lt;0.0001</b>	(-2.46, -1.34)	<b>&lt;0.0001</b>	(-3.16, -1.28)	<b>&lt;0.0001</b>	(-2.46, -1.34)	<b>&lt;0.0001</b>	(-3.16, -1.28)	<b>&lt;0.0001</b>	(-2.46, -1.34)	<b>&lt;0.0001</b>	(-3.16, -1.28)
SAEA1-SADM2	<b>0.0012</b>	(0.02, 0.69)	<b>0.0081</b>	(-2.38, 0.37)	0.3931	(-0.85, 0.59)	0.1706	(-1.72, 1.16)	0.3931	(-0.85, 0.59)	0.1706	(-1.72, 1.16)	0.3931	(-0.85, 0.59)	0.1706	(-1.72, 1.16)	0.3931	(-0.85, 0.59)	0.1706	(-1.72, 1.16)
SAEA2-SAEA3	<b>&lt;0.0001</b>	(-2.15, -0.97)	<b>&lt;0.0001</b>	(-5.80, -3.40)	<b>&lt;0.0001</b>	(-4.69, -1.97)	<b>&lt;0.0001</b>	(-5.73, -2.71)	<b>&lt;0.0001</b>	(-4.69, -1.97)	<b>&lt;0.0001</b>	(-5.73, -2.71)	<b>&lt;0.0001</b>	(-4.69, -1.97)	<b>&lt;0.0001</b>	(-5.73, -2.71)	<b>&lt;0.0001</b>	(-4.69, -1.97)	<b>&lt;0.0001</b>	(-5.73, -2.71)
SAEA2-SADM2	0.1996	(-0.20, 0.15)	<b>&lt;0.0001</b>	(-2.64, -0.17)	<b>&lt;0.0001</b>	(-2.70, -0.66)	<b>0.0007</b>	(-3.61, 0.08)	<b>0.0007</b>	(-2.70, -0.66)	<b>0.0007</b>	(-3.61, 0.08)	<b>0.0007</b>	(-2.70, -0.66)	<b>0.0007</b>	(-3.61, 0.08)	<b>0.0007</b>	(-2.70, -0.66)	<b>0.0007</b>	(-3.61, 0.08)
SAEA3-SADM2	<b>&lt;0.0001</b>	(0.51, 1.82)	<b>0.0081</b>	(0.91, 3.32)	0.0087	(0.83, 2.88)	0.2801	(-0.62, 1.93)	0.0087	(0.83, 2.88)	0.2801	(-0.62, 1.93)	0.0087	(0.83, 2.88)	0.2801	(-0.62, 1.93)	0.0087	(0.83, 2.88)	0.2801	(-0.62, 1.93)

On the other hand, the remaining algorithms exhibit similar average performances when analyzing the regression curves based on the averages of each set. As expected, the error increases with higher contrasts. The average error ranges from approximately 5 to 25 [%/pixel] within the considered contrast range.

However, statistical pairwise comparison tests have revealed some differences. Only in the highest contrast test set ( $\chi = 4$ ) there was no evidence of a significant difference (Friedman Rank Sum Test p-value = 0.0693).

Table 4.30 provides the p-values for all post-hoc comparisons, along with their respective tests. Considering the significance level corrected by the Bonferroni method (= 0.0083), no difference was detected in the first test set. Therefore, it is possible that a Type I error occurred during the test with multiple samples. The confidence intervals for means (in case of Paired T-Test) and for medians (in case of Wilcoxon Signed-Rank Test) are also shown in Table 4.30. It is worth noting that SAEA2 exhibits superior performance compared to other SAEAs. However, SAEA2 did not outperform SADM2 in the third and fourth test sets. Summarizing, when considering indicator  $\zeta_{EOE}$ , SAEA2 tends to perform at an equivalent or superior level compared to the other algorithms in all cases.

Figure 4.30 showcases the results of the shape recovery indicator ( $\zeta_S$ ). Anomalous behavior in the test set  $\chi = 1$ , similar to what was observed previously, is once again apparent in the SADM1 method. However, this behavior is significantly attenuated compared to previous indicator. It is notable that all algorithms exhibit an increase in error as the contrast level rises. This outcome is expected since the qualitative method employed to generate the initial image tends to loose performance with higher contrast levels. In terms of indicator samples, test sets  $\chi = 1$  and  $\chi = 2$  demonstrate considerable similarity across all algorithms, with the exception of SADM1.

Regarding the lines obtained through regression analysis for the means in each test set, they demonstrate high similarity between the algorithms, with the exception of SADM1. However, when applying pairwise statistical comparisons using the Friedman Rank Sum Test, differences are found between the SAEA1, SAEA2, SAEA3, and SADM2 algorithms in each test set. In the first four test sets, the hypothesis of equal performance was rejected with a p-value less than 0.0001 at a 95% confidence level. Even in the fifth test set, where the p-value was slightly higher (0.0015), the null hypothesis was still rejected.

Table 4.7 displays the results of the post-hoc analysis, presenting the p-values for multiple pairwise comparisons obtained by Wilcoxon Signed-Rank Test in all cases. The table reveals that differences in performance are more frequently detected in the first four test sets. As for the latter test set, the difference is detected in only two of the six cases. An examination of the confidence interval of the medians for each pairwise comparison was accomplished and showed that SAEA2 demonstrates better performance in the first four test sets compared to the other SAEAs. Furthermore, in the second, third, and fourth test sets, SAEA2 outperforms SADM2 as well.

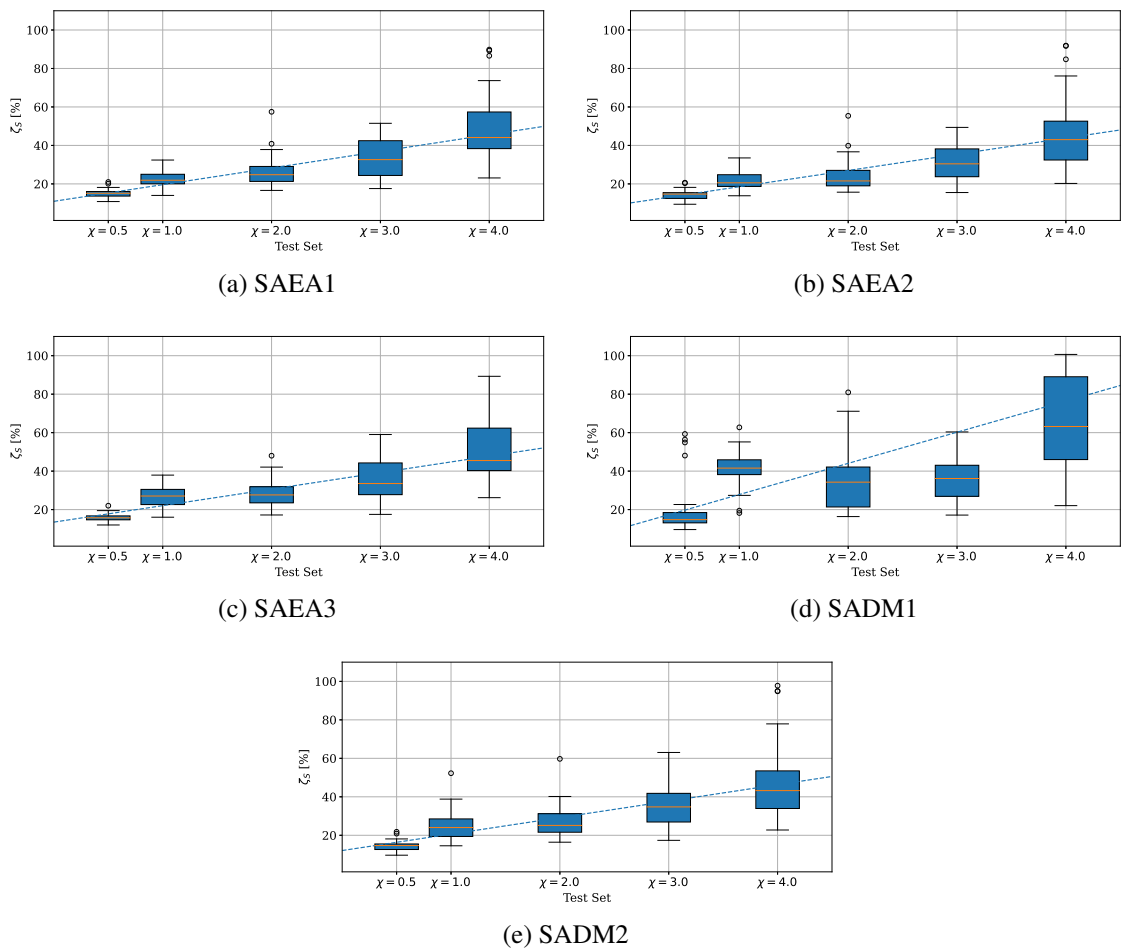


Figure 4.30: Evolution of the shape recovering error ( $\zeta_S$ ) for the proposed algorithms (a)-(e): SAEA1, SAEA2, SAEA3, SADM1, and SADM2, respectively. Additionally, a straight line obtained through linear regression is overlaid on each subfigure. This line represents the estimated evolution of the average performance, based on the means of each test set.

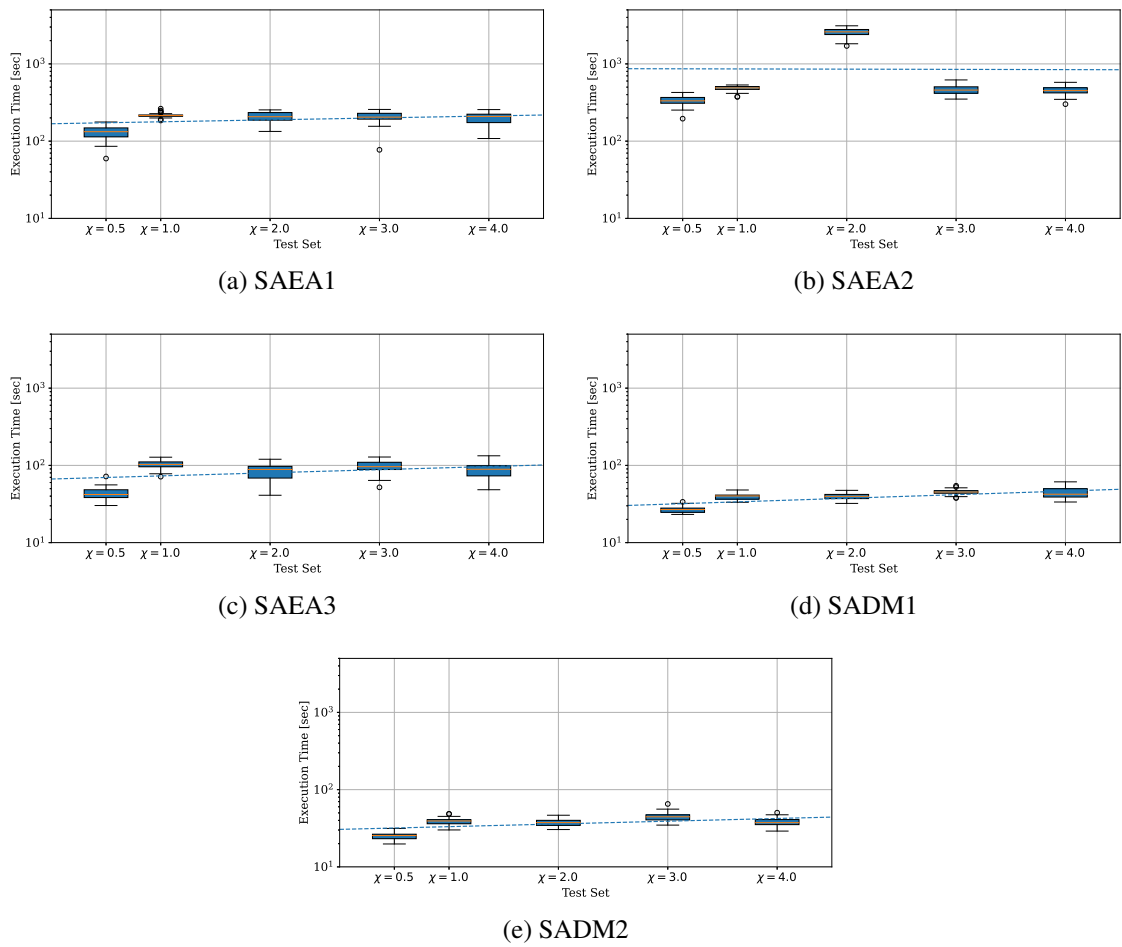


Figura 4.31: Evolution of execution time for the proposed algorithms (a)-(e): SAEA1, SAEA2, SAEA3, SADM1, and SADM2, respectively. Additionally, a straight line obtained through linear regression is overlaid on each subfigure. This line represents the estimated evolution of the average performance, based on the means of each test set.

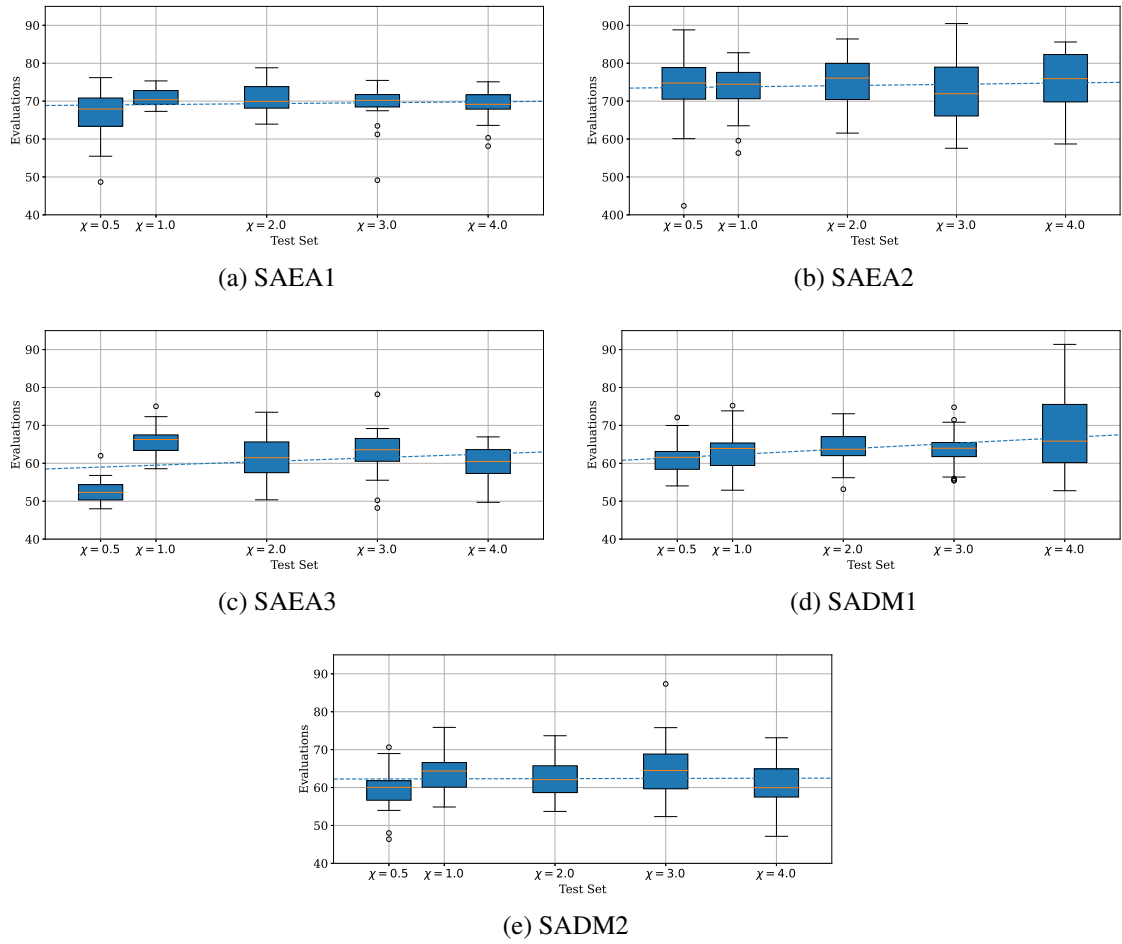


Figura 4.32: Evolution of the number of evaluations for the proposed algorithms (a)-(e): SAEA1, SAEA2, SAEA3, SADM1, and SADM2, respectively. Additionally, a straight line obtained through linear regression is overlaid on each subfigure. This line represents the estimated evolution of the average performance, based on the means of each test set.

Figure 4.31 displays the running time of the algorithms for each test set. The curve obtained through linear regression of the means reveals that the execution time of the algorithms exhibits minimal variation as the contrast increases. This finding suggests that the growth of contrast does not have a significant impact on the running time of the algorithms. A notable exception is observed in the results of the third test set for the SAEA2 algorithm. In this case, the running time differs significantly from the other test sets. There is no clear reason for this anomalous behavior and an unexpected process in the used computer might be a hypothesis. Comparatively, the execution time of the SADM1 and SADM2 algorithms tends to be shorter than that of the other algorithms. On the other hand, the SAEA2 algorithm generally exhibits the longest execution time among the tested algorithms.

Figure 4.32 illustrates the number of evaluations performed by each algorithm in each test set. Similar to the runtime results, the number of evaluations shows minimal variation as the contrast increases. This indicates that the algorithms' ability to converge is largely unaffected by increasing contrast levels.

Tabela 4.8: P-values for post-hoc multiple pairwise comparisons considering the number of evaluations, with the compatible statistical test for each test set. The significance level has been corrected using the Bonferroni method, resulting in a significance threshold of 0.0167. Detected differences are indicated in bold format. Confidence intervals for means are also available.

Pairs	$\chi = 0.5$		$\chi = 4$	
	p-value	Confi. In.	p-value	Confi. In.
SAEA3-SADM1	<b>&lt;0.0001</b>	(-11.1, -6.27)	<b>0.0004</b>	(-12.7, -2.84)
SAEA3-SADM2	<b>&lt;0.0001</b>	(-10.3, -4.62)	0.6238	(-3.75, 2.53)
SADM1-SADM2	0.2693	(-1.52, 3.95)	<b>0.0005</b>	(2.48, 11.8)

Among the algorithms, SAEA2 exhibits the highest number of evaluations, approximately 10 times more than the other algorithms. This outcome was expected since SAEA2 requires more iterations to converge. Interestingly, in contrast to the runtime results, the number of evaluations for SAEA2 in the third test set aligns with the other sets. This suggests that the unexpected increase in execution time observed in the third set was unrelated to the number of evaluations. This finding can support the hypothesis that an external factor, such as an unexpected process on the computer running the experiments, might have influenced the execution time.

In terms of the algorithms with the lowest number of evaluations, SAEA3, SADM1, and SADM2 stand out. Statistical tests rejected the hypothesis of equal performance among these three algorithms under the 95% confidence level only in the test sets  $\chi = 0.5$  and  $\chi = 4$ , with p-values smaller than 0.0001 obtained by the Randomized Complete Block Design. Subsequent post hoc analysis through multiple pairwise comparisons (Table 4.8) reveals that, for  $\chi = 0.5$ , SAEA3 had from 4 to 11 fewer evaluations than SADM1 or SADM2, in average. For  $\chi = 4.0$ , SAEA3 had from 3 to 13 fewer evaluations than SADM1, in average, and SADM1 had from 2 to 12 more evaluations than SADM2, in average. Therefore, there is no clear tendency of superiority among these three algorithms.

# Capítulo 5

## Conclusion

This chapter concludes the thesis. Firstly, a recapitulation of the main topics explored in the thesis is presented in Section 5.1. This serves as a concise summary, highlighting the main ideas, proposals, key findings, and their significance within the research context. By revisiting the main research questions and objectives, the recapitulation provides a holistic view of the thesis's scope and accomplishments.

Following the recapitulation, a critical analysis of the research methodology, limitations, and potential biases is presented in Section 5.2. Self-criticism plays a crucial role in research as it allows for a reflective assessment of the strengths and weaknesses of the study. By acknowledging any limitations or areas for improvement, this section contributes to the overall integrity and maturity of the research project.

Next, the chapter discusses the proposal continuity in Section 5.3. In the continuity proposals, different ideas are described that can be addressed after this project. The topics are developments of subjects that were part of the work, which could receive more attention and could contribute to the literature. Lastly, the chapter concludes with a list of the bibliographic production generated during the project (Section 5.4).

### 5.1 Recapitulation

Microwave imaging is a significant inverse problem with applications in various fields such as defect identification in structures, through-wall imaging, cancer detection, among others. It involves reconstructing the interior of inaccessible regions based on field measurements at microwave frequencies and images derived from the electrical properties of the materials within the investigated space.

This thesis aimed to comprehensively review the mathematical aspects of the problem, recognizing that microwave imaging is an electromagnetic inverse scattering problem. The objective is to determine the cause, i.e., one or more scatterers, of the observed effect, i.e., the scattered field. Maxwell's Equations provide integral equations that relate the observed

scattered field outside the region of interest with the unknown electromagnetic field and the mapping of electrical properties inside the region. However, this relationship is nonlinear due to the unknown nature of the electromagnetic field and the mapping of electrical properties, requiring simultaneous resolution of both variables.

The inverse problem is known to be ill-posed, lacking a unique solution or continuity in the relationship between the scattered field and the imaged medium. To address this, various formulas, including traditional integral formulas, have been developed to mitigate the inherent challenges of the problem. The degree of nonlinearity increases with the number of scatterers or their contrast, further complicating the solution process.

The thesis also presented an extensive overview of numerical methodologies to solve the problem, covering topics such as discretization, linear approximations, and regularization methods for ill-posed systems of equations. In the literature, numerical methods for the inverse electromagnetic scattering problem are classified into qualitative and quantitative methods. Qualitative methods focus on reconstructing the shape of scatterers, while quantitative methods aim to estimate the electrical properties in addition to recovering their geometries.

Noteworthy within qualitative methods is the Orthogonality Sampling Method (OSM), capable of recovering scatterer geometry and detecting different contrast levels. On the other hand, quantitative methods can be further categorized as deterministic or stochastic, depending on whether they rely on well-defined sequences of steps or stochastic processes. Deep Learning techniques have gained attention for their potential in enabling real-time imaging. Additionally, the application of Surrogate Models to assist algorithms for the problem, particularly those dependent on forward problem simulations, is an emerging area that holds promise in reducing computational costs while requiring effective representation methods.

The thesis also identified others shortcomings in the field, such as the lack of an integrated platform for algorithm development and testing, the need for standardized performance indicators, and limited generalization capacity in experimental designs. To address these issues, the thesis proposed two main propositions in the two-dimensional case of the electromagnetic inverse problem.

The first proposal involved applying Surrogate Models to assist Evolutionary Algorithms and Descent Methods, utilizing images generated by the OSM qualitative method for representing solutions. Such approach implies in transforming the inverse problem into a two-dimensional optimization problem, allowing for efficient treatment by Surrogate Models and achieving greater precision than similar proposals in the literature (Salucci et al., 2022). Five formulations for surrogate model-assisted algorithms were proposed, utilizing both evolutionary and descent algorithms.

The second proposal focused on implementing a comprehensive algorithm development and testing structure that supports experimental design, quantification, and performance comparison of algorithms for the problem. This structure included software with object-oriented features capable of conducting case studies and benchmarking, a less explored area in the lite-



ature. The software facilitated exploring different problem characteristics, measuring various aspects of obtained images, and performing statistical comparisons to evaluate results more robustly.

The computational experiments conducted in the thesis included both case studies and benchmarking. The case studies covered four problem scenarios: simple, multiple, nonhomogeneous, and strong scatterers. In these studies, the proposed methods were compared against traditional deterministic methods. The benchmarking study focused on evaluating the performance of the proposed algorithms, specifically considering increasing object contrast levels.

The computational experiments conducted in this thesis provided valuable insights into the performance of algorithms assisted by surrogate models for microwave imaging. In general, the results indicated that these proposed algorithms have the capability to obtain images with comparable or slightly better qualities than traditional methods in the simplest cases. However, this improvement comes at a slightly higher computational cost in some instances.

One of the notable findings was that in high-contrast scenarios, the methodology assisted by surrogate models was able to reconstruct objects that traditional methods struggled with, all while maintaining a reasonable computational cost. This suggests that the surrogate models have the potential to address the limitations of traditional techniques and enable the imaging of challenging objects. It was also observed that the limitations of OSM posed restrictions on the application of the proposed methodology, particularly when dealing with numerous scatterers and varying levels of contrast. This highlights the need to consider the limitations of the qualitative method when applying the proposed approach.

In terms of the performance comparison between different algorithm versions, one of the evolutionary versions (SAEA2) demonstrated better image quality indicators but at a higher computational cost. On the other hand, a version based on the descent method (SADM2) showed comparable results in terms of image quality indicators while requiring significantly fewer computational resources. This finding suggests that a descent-based approach may offer a good balance between performance and computational efficiency.

Based on these results, it is evident that the application of surrogate models in the transformation of the inverse problem into a two-dimensional optimization problem is highly feasible. The objective function becomes much easier to predict using surrogate models, enabling the solution of scenarios where traditional techniques struggle to reconstruct images. The advantage of the approach lies in the reduced number of variables, which can be effectively handled by surrogate models. However, it is important to acknowledge that the limitations of OSM in certain scenarios prevent a more general application of the proposed methodology, unlike what is achievable with existing techniques in the literature (Salucci et al., 2022).

These promising results encourage further development of the technique of applying surrogate models to strike a better balance between the number of variables that the surrogate model must handle and the ability to generalize to more complex scattering scenarios. By refining the application of surrogate models, it may be possible to overcome current limitations

and expand the scope of microwave imaging, opening new avenues for improved imaging performance in challenging environments.

## 5.2 Self-Criticism

Some critical points in conducting this research are commented below:

- In this work, a case study based on real measurements from the Fresnel Institute (Geffrin et al., 2005), which is commonly used in the literature, was not considered. Although including this case study could provide additional support for the real-world applicability of the proposed methodology, it was not feasible due to the slight differences in the electromagnetic propagation model used in the data. Adapting the model would require substantial time and effort, which was not available during the completion of this work.
- Regarding the benchmark study, the option was made to be more succinct and focus on the proposed methods. Therefore, the traditional deterministic methods were not included in the analysis. While including these methods would have allowed for a more comprehensive comparison, it would have increased the number of graphs and data to analyze, which was not the primary objective of this study.
- Salucci et al. (2022) presented the only methodology available in the literature that applied surrogate models to the problem, and this work frequently cites their contribution to contextualize its own. However, the methodology proposed by them was not implemented in this study. It would have been interesting to include their methodology in the comparison to evaluate the efficiency of the transformation into a two-dimensional optimization problem and identify scenarios where their approach may outperform the one proposed in this work.
- In the obtained results, it was observed that the formulations based on the SAEAs took longer to run, even when the number of evaluations had the same limit than SADMs. This suggests that the evolutionary operations employed in the algorithm may have a significant impact on the overall computational cost. Further investigation would be necessary to implement optimizations and improve the performance of these algorithms in terms of computational efficiency.

## 5.3 Continuity Proposals

There are some topics that can be further explored in a future work:

- **Improvements to the initial image approach:** In this work, one of the evident needs is to expand the scope of application of OSM to address more challenging scenarios effectively. This requires modifying equations (??)-(??) to enhance the method's robustness against highly nonlinear problems. One approach could be exploring new integral

equations (Bevacqua and Isernia, 2021) or investigating efficient domain decomposition techniques (Zhang et al., 2022). Another alternative could be developing more efficient ways to obtain an initial image while controlling the computational cost.

- **A better elaborated comparative study addressing traditional deterministic methods:** The implementation of a benchmark tool opens up possibilities for a more elaborate experimental design to quantitatively describe the average performance of traditional deterministic methods using the proposed indicators. This type of study is currently lacking in the literature and could provide valuable insights into the differences between these algorithms when subjected to a comprehensive comparison.
- **Creation of standard test sets:** Creating a standard test suite would be beneficial to the field, as it would enable researchers to compare their algorithms using well-defined and meaningful scenarios. This standardized approach would facilitate future studies by multiple authors, ensuring consistency and facilitating comparisons.
- **Creation of test sets based on DNL value:** Furthermore, it would be advantageous to design a problem generation mechanism based on a DNL target value. This mechanism would enable studies analyzing the variation of performance indicators of algorithms with varying DNL. Machine learning techniques could be employed to predict the DNL using only the characteristics of the desired problem, further enhancing the efficiency of these investigations.
- **Limits of application of the methods:** During the experiments in this work, it was observed that DNL alone is not always sufficient to quantify the difficulty of solving a particular problem for an algorithm. In some cases, algorithms may struggle to solve problems with lower DNL while being able to solve higher DNL problems. It would be valuable to develop a way to quantify the application limits of an algorithm, taking into account the problem's specific characteristics. This approach would provide a more comprehensive description of the operating limits of each method.
- **Implementation of the 3D model:** To continue this work, formulating a standard definition for the three-dimensional problem and implementing a library capable of supporting and adapting the development and testing of algorithms in this context would be valuable. Additionally, implementing the methodology proposed in this work in its three-dimensional version would further extend its applicability and provide insights into its performance in more complex scenarios.

## 5.4 Bibliographic Production

### Journals:

- Batista, A. C., Batista, L. S., & Adriano, R. (2021). A quadratic programming approach for microwave imaging. *IEEE Transactions on Antennas and Propagation*, 69(8), 4923-

4934.

- Vargas, J. O., Batista, A. C., Batista, L. S., & Adriano, R. (2021). On the computational complexity of the conjugate-gradient method for solving inverse scattering problems. *Journal of Electromagnetic Waves and Applications*, 35(17), 2323-2334.
- Batista, A. C., Adriano, R., & Batista, L. S. (2021). EISPY2D: An Open-Source Python Library for the Development and Comparison of Algorithms in Two-Dimensional Electromagnetic Inverse Scattering Problems. *arXiv preprint arXiv:2111.02185*. **Under review.**

#### Conferences:

- Vargas, J. O., Batista, A. C. ; Batista, L. S., Adriano, R. A Fast Conjugate Gradient Method for Solving Two-Dimensional Electromagnetic Inverse Scattering Problems. *XX Simpósio Brasileiro de Micro-Ondas e Optoeletrônica, 2022, Natal, RN. Anais do XX Simpósio Brasileiro de Micro-Ondas e Optoeletrônica, 2022.*

## Referências Bibliográficas

- Bartle, R. G. (1995). *The elements of integration and Lebesgue measure*, volume 27. John Wiley & Sons, Ltd.
- Batista, A. C., Batista, L. S., and Adriano, R. (2021). A quadratic programming approach for microwave imaging. *IEEE Transactions on Antennas and Propagation*.
- Bevacqua, M. T. and Isernia, T. (2021). Quantitative non-linear inverse scattering: A wealth of possibilities through smart rewritings of the basic equations. *IEEE Open Journal of Antennas and Propagation*, 2:335–348.
- Bevacqua, M. T., Isernia, T., Palmeri, R., Akıncı, M. N., and Crocco, L. (2020). Physical insight unveils new imaging capabilities of orthogonality sampling method. *IEEE Transactions on Antennas and Propagation*, 68(5):4014–4021.
- Chen, X. (2010). Subspace-based optimization method for solving inverse-scattering problems. *IEEE Transactions on Geoscience and Remote Sensing*, 48(1):42–49.
- Chen, X. (2017). *Computational Methods for Electromagnetic Inverse Scattering*. Wiley-IEEE Press.
- Chew, W. (2009). *Integral equation methods for electromagnetic and elastic waves*. Morgan & Claypool Publishers, San Rafael, Calif.
- Chew, W. C. (1995). *Waves and Fields in Inhomogeneous Media*. IEEE Press.
- Deb, K., Pratap, A., Agarwal, S., and Meyarivan, T. (2002). A fast and elitist multiobjective genetic algorithm: Nsga-ii. *IEEE transactions on evolutionary computation*, 6(2):182–197.
- Geffrin, J.-M., Sabouroux, P., and Eyraud, C. (2005). Free space experimental scattering database continuation: experimental set-up and measurement precision. *Inverse Problems*, 21(6):S117–S130.
- Kellogg, O. D. (1953). *Foundations of potential theory*, volume 31. Courier Corporation.
- Kirsch, A. (2011). *An Introduction to the Mathematical Theory of Inverse Problems*. Number 120 in Applied Mathematical Science. Springer, Verlag, NY, 2 edition.
- Lebedev, L. P., Vorovich, I. I., and Gladwell, G. (1996). *Functional Analysis - Applications*

- in Mechanics and Inverse Problems*. Number 41 in Solid Mechanics and Its Applications. Springer, Netherlands, 1 edition.
- Maxwell, J. C. (1865). Viii. a dynamical theory of the electromagnetic field. *Philosophical transactions of the Royal Society of London*, (155):459–512.
- Milgram, S., Bickman, L., and Berkowitz, L. (1969). Note on the drawing power of crowds of different size. *Journal of personality and social psychology*, 13(2):79.
- Salucci, M., Poli, L., Rocca, P., and Massa, A. (2022). Learned global optimization for inverse scattering problems: Matching global search with computational efficiency. *IEEE Transactions on Antennas and Propagation*, 70(8):6240–6255.
- Shah, P. and Moghaddam, M. (2015). Fast level set based method for high contrast microwave imaging. In *Proc. PIERS*, pages 253–257.
- Shung-Wu Lee, Boersma, J., Chak-Lam Law, and Deschamps, G. (1980). Singularity in green’s function and its numerical evaluation. *IEEE Transactions on Antennas and Propagation*, 28(3):311–317.
- Van Bladel, J. (1961). Some remarks on green’s dyadic for infinite space. *IRE Transactions on Antennas and Propagation*, 9(6):563–566.
- van den Berg, P. M., van Broekhoven, A. L., and Abubakar, A. (1999). Extended contrast source inversion. *Inverse Problems*, 15(5):1325–1344.
- Van Dyke, M. C. C., Teixeira, M. M., and Barker, B. M. (2019). Fantastic yeasts and where to find them: the hidden diversity of dimorphic fungal pathogens. *Current opinion in microbiology*, 52:55–63.
- Yaghjian, A. D. (1980). Electric dyadic green’s functions in the source region. *Proceedings of the IEEE*, 68(2):248–263.
- Zhang, Y., Yin, T., Zhao, Z., Nie, Z., and Chen, X. (2022). An iterative domain decomposition technique based on subspace-based optimization method for solving highly nonlinear inverse problem. *IEEE Transactions on Geoscience and Remote Sensing*, 60:1–13.

## Apêndice A

### Como fazer citações

Você pode fazer uma citação de diversas formas. Se você quiser fazer uma citação entre parênteses, você pode fazer assim: (Milgram et al., 1969). Se você quiser mencionar o número da página, você pode fazer assim: (Deb et al., 2002, p. 10). Agora, se você quiser fazer uma citação onde o autor é parte da sentença, você pode fazer assim: Maxwell (1865) afirma que... Se você quiser fazer uma citação com mais de um autor, você pode fazer assim: (Maxwell, 1865; Van Dyke et al., 2019).

## Apêndice B

### Como escrever equações

Um exemplo básico de equação:

$$\mathcal{F}(\mathbf{r}, t) = \Re\{\mathbf{F}(\mathbf{r})e^{j\omega t}\} \quad (\text{B.1})$$

Um exemplo sobre como escrever múltiplas equações e o uso de fonte cursiva nas letras:

$$\nabla \times \mathcal{E}(\mathbf{r}, t) = -\frac{\partial \mathcal{B}}{\partial t}(\mathbf{r}, t) \quad (\text{B.2})$$

$$\nabla \times \mathcal{H}(\mathbf{r}, t) = \frac{\partial \mathcal{D}}{\partial t}(\mathbf{r}, t) + \mathcal{J}(\mathbf{r}, t) \quad (\text{B.3})$$

$$\nabla \cdot \mathcal{D}(\mathbf{r}, t) = \rho(\mathbf{r}, t) \quad (\text{B.4})$$

$$\nabla \cdot \mathcal{B}(\mathbf{r}, t) = 0 \quad (\text{B.5})$$

Um exemplo de desenvolvimento de equação:

$$\nabla \times \mathbf{H}(\mathbf{r}) = j\omega\epsilon_0\epsilon_r\mathbf{E}(\mathbf{r}) + \boldsymbol{\sigma}(\mathbf{r})\mathbf{E}(\mathbf{r}) + \mathbf{J}_i(\mathbf{r}) \quad (\text{B.6})$$

$$= j\omega\epsilon_0 \left( \epsilon_r(\mathbf{r}) - j\frac{\boldsymbol{\sigma}(\mathbf{r})}{\omega\epsilon_0} \right) \mathbf{E}(\mathbf{r}) + \mathbf{J}_i(\mathbf{r}) \quad (\text{B.7})$$

$$= j\omega\mathcal{E}(\mathbf{r})\mathbf{E}(\mathbf{r}) + \mathbf{J}_i(\mathbf{r}) \quad (\text{B.8})$$

Um exemplo de equação quebrada em mais de uma linha:

$$\begin{aligned} \chi(\boldsymbol{\rho})E_{z_i}(\boldsymbol{\rho}) = J_{z_{eq}}(\boldsymbol{\rho}) + \frac{jk_b^2}{4}\chi(\boldsymbol{\rho}) \int_S dS' J_0(k_b|\boldsymbol{\rho} - \boldsymbol{\rho}'|)J_{z_{eq}}(\boldsymbol{\rho}') \\ + \frac{jk_b^2}{4}\chi(\boldsymbol{\rho}) \int_S dS' Y_0(k_b|\boldsymbol{\rho} - \boldsymbol{\rho}'|)J_{z_{eq}}(\boldsymbol{\rho}') \end{aligned} \quad (\text{B.9})$$



Um exemplo de equação com somatórios e integrais:

$$\begin{aligned} \iint_D E_{z_s}(\theta, \phi) w_u^{(\theta)}(\theta) w_v^{(\phi)}(\phi) d\theta d\phi = \\ - \frac{jk_b^2}{4} \sum_{i=1}^{N_I} \sum_{j=1}^{N_J} \sum_{p=1}^{N_P} \sum_{q=1}^{N_Q} \sum_{r=1}^{N_R} a_{ij} b_{pqr} \iint_D \iint_S d\theta d\phi dx dy \left[ G_{2D}^D(\theta, x, y) \right. \\ \left. f_i^{(x)}(x) f_j^{(y)}(y) g_p^{(x)}(x) g_q^{(y)}(y) g_r^{(\phi)}(\phi) w_u^{(\theta)}(\theta) w_v^{(\phi)}(\phi) \right], \\ u = 1, \dots, N_U, v = 1, \dots, N_V \quad (\text{B.10}) \end{aligned}$$

Um exemplo de definição de matriz:

$$\bar{\mathbf{\Lambda}} = \begin{bmatrix} \Lambda_{11} & \Lambda_{12} & \cdots & \Lambda_{1N_V} \\ \Lambda_{21} & \Lambda_{22} & \cdots & \Lambda_{2N_V} \\ \vdots & \vdots & \ddots & \vdots \\ \Lambda_{u1} & \Lambda_{u2} & \cdots & \Lambda_{uN_V} \\ \vdots & \vdots & \ddots & \vdots \\ \Lambda_{N_U1} & \Lambda_{N_U2} & \cdots & \Lambda_{N_UN_V} \end{bmatrix} \quad (\text{B.11})$$

Um exemplo de definição de casos:

$$w_{uv} = \begin{cases} 1, & \text{in } D_{uv}, \\ 0, & \text{outside, } D_{uv} \end{cases} \quad (\text{B.12})$$

Um exemplo para organização de três matrizes em uma mesma linha:

$$\bar{\mathbf{\chi}} = \begin{bmatrix} \chi_{11} & 0 & \cdots & 0 \\ 0 & \chi_{12} & \cdots & 0 \\ \vdots & \vdots & \ddots & \vdots \\ 0 & 0 & \cdots & \chi_{N_I N_J} \end{bmatrix} \quad \bar{\mathbf{\beta}} = \begin{bmatrix} \beta_{11} & 0 & \cdots & 0 \\ 0 & \beta_{12} & \cdots & 0 \\ \vdots & \vdots & \ddots & \vdots \\ 0 & 0 & \cdots & \beta_{N_I N_J} \end{bmatrix} \quad \bar{\mathbf{R}} = \begin{bmatrix} R_{11} & 0 & \cdots & 0 \\ 0 & R_{12} & \cdots & 0 \\ \vdots & \vdots & \ddots & \vdots \\ 0 & 0 & \cdots & R_{N_I N_J} \end{bmatrix} \quad (\text{B.13})$$

Note que você pode referenciar equações das seguintes formas:

- Quando ela estiver no meio da frase, você pode usar simplesmente o comando `\eqref{}`.  
Por exemplo: “...como mostrado em (B.2), ...”
- Quando você estiver no início da frase, você pode escrever: “A Eq. (B.2) mostra que...”

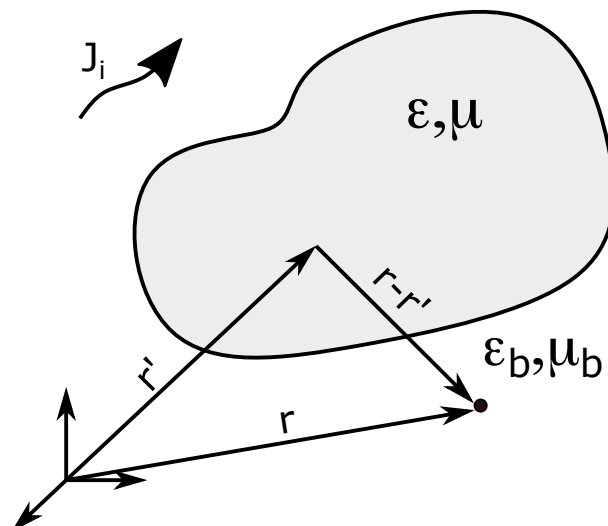


Figura C.1: General scattering problem.

## Apêndice C

### Como inserir figuras

Um exemplo sobre como inserir figuras simples pode ser visto em C.1. Você pode referenciar figuras através do comando `\ref{}` ou do comando `\autoref{}`. O primeiro comando apenas referencia o número da figura, enquanto o segundo comando referencia o número da figura e o nome dela. Por exemplo, você pode escrever: “...como mostrado na Figura C.1, ...”.

Um exemplo de múltiplas figuras pode ser visto na Figura C.2.

Um outro exemplo de múltiplas figuras pode ser visto na Figura C.3.

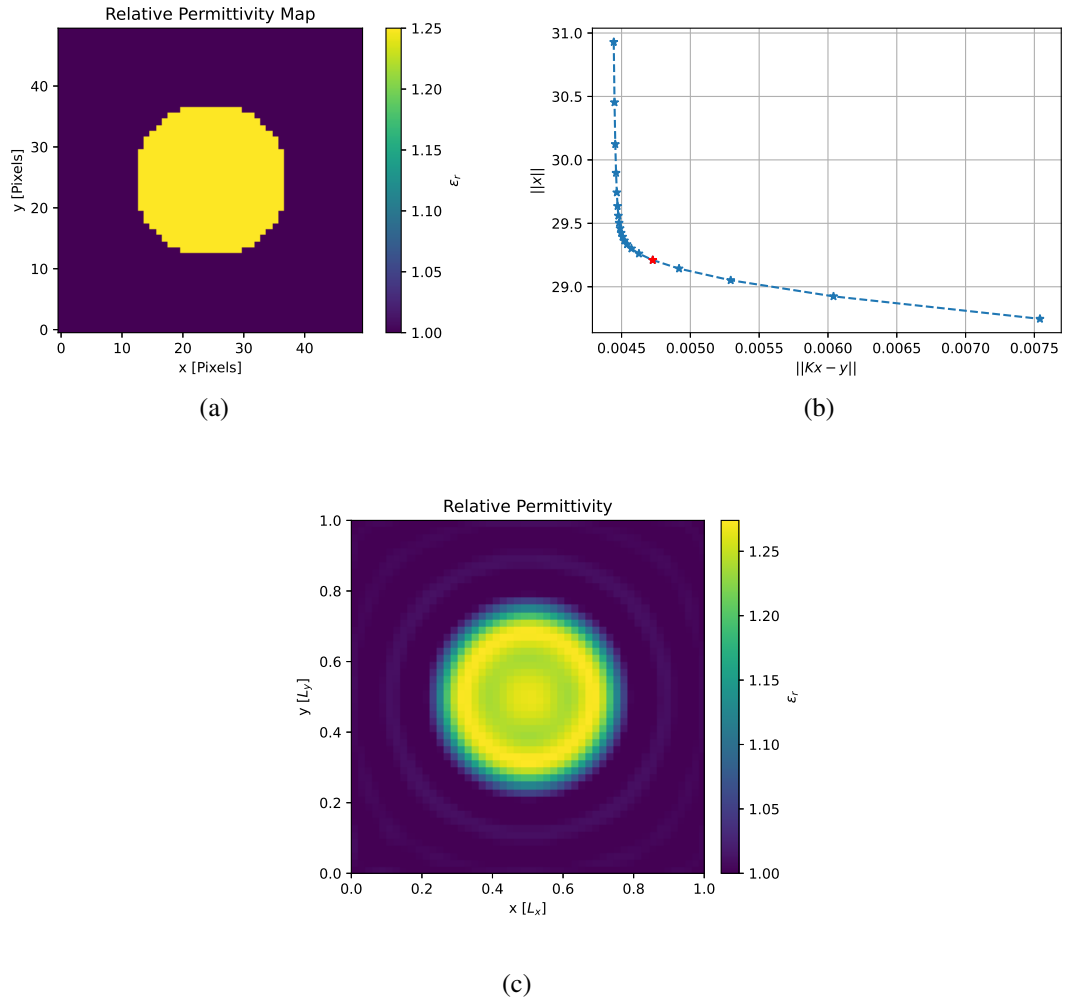


Figura C.2: Example of applying the L-curve Method to a linear problem where it presupposes knowledge of the total field. (a) A simple instance of a contrast dielectric circle  $\chi = 0.25$  and radius  $0.8\lambda_b$ . Respecting the degrees of freedom, the scattered field was sampled in 45 positions for 45 incidence angles at a distance of  $10\lambda_b$  from the center of the image. (b) L-curve considering 20 values of  $\alpha_T$  in a range of  $10^{-5}$  a  $10^{-2}$ . The red dot represents the solution with the shortest normalized distance to the origin. Its  $\alpha_T$  value is approximately  $2.3357 \times 10^{-3}$ . (c) Reconstruction of the image using the  $\alpha_T$  value from the red dot. No inverse crime was committed since the data were obtained from the analytical solution.

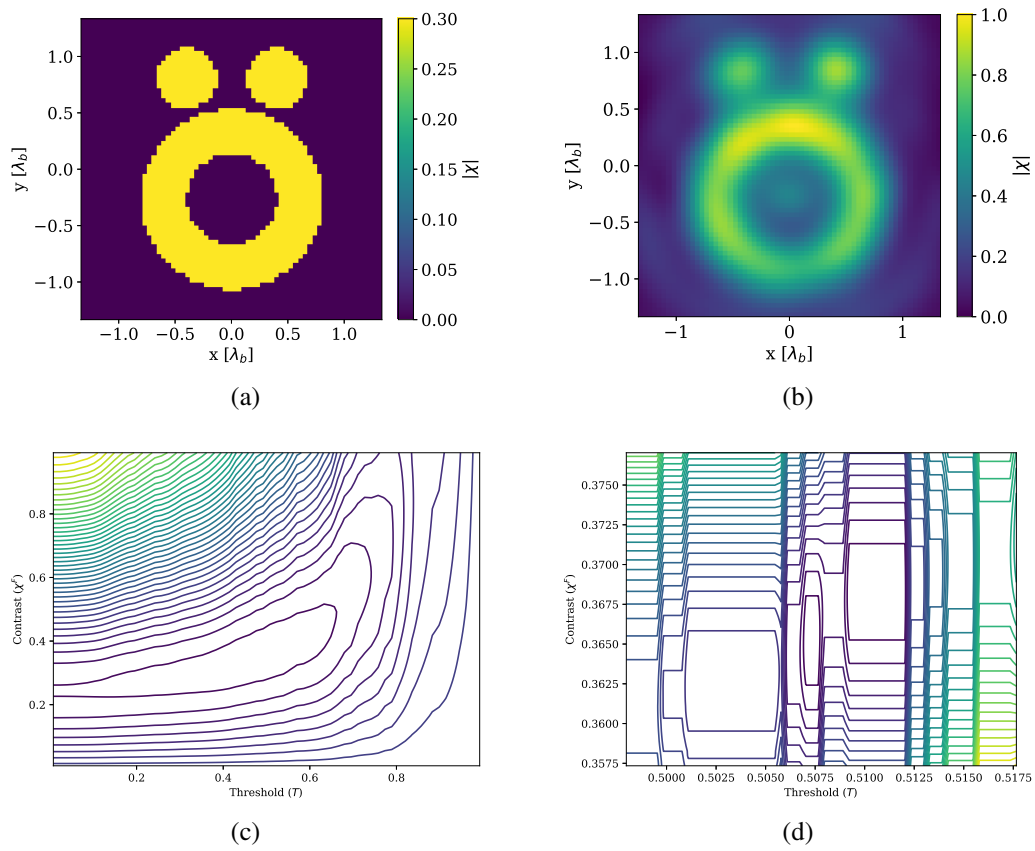


Figure C.3: Example of an objective function resulting from the transformation of the inversion problem into a two-dimensional optimization one: (a) the ground-truth image; (b) the image obtained by OSM; (c) the surface obtained by the transformation of the inversion problem into a two-dimensional optimization one; and (d) a zoom over the region close to the optimum.

## Apêndice D

### Como inserir tabelas

Um exemplo de tabela simples pode ser visto em D.1. Você pode referenciar tabelas da mesma forma que você referencia figuras. Por exemplo, você pode escrever: “...como mostrado na Tabela D.1, ...”.

Tabela D.1: Classification of methods by their properties.

Classes		Methods		
Qualitative	Linear Sampling Method			
	Orthogonality Sampling Method			
Quantitative	Deterministic	Linear	Born Approximation	
			Rytov Approximation	
			Back-Propagation Method	
			Dominant Current Scheme	
	Deterministic	Forward and inverse subproblems	Born Iterative Method	
			Distorted Born Iterative Method	
			Variational Born Iterative Method	
			Level-Set Method	
	Nonlinear	Gradient-based	Conjugated-Gradient Method	
			Contrast Source Inversion	
			Subspace-based	Optimization
			Method	
	Other	Other	Compressive Sensing	
			Regularization on $L_p$ Banach Spaces	
			Virtual Experiments	
Deep learning methods				
Stochastic	Representation	Known geometries		
		Contours		
		Pixel-based		
	Objective function	Data equation residual		
		Data and state equation residual		

# Apêndice E

## Como inserir algoritmos

Um exemplo de algoritmo é o seguinte:

---

**Algorithm 1:** Distorted Born Iterative Method.

---

**Input:**  $\bar{\mathbf{E}}^s, \bar{\mathbf{G}}^{2D}, \bar{\mathbf{G}}^S$

**Output:**  $\bar{\boldsymbol{\chi}}, \bar{\mathbf{E}}$

```

1 Compute an initial guess  $\bar{\boldsymbol{\chi}}^0$  based on available information
2  $t \leftarrow 0$ 
3 while some criterion is not reached do
4   Solve  $(\bar{\mathbf{I}} - \bar{\mathbf{G}}^S \bar{\boldsymbol{\chi}}^t) \bar{\mathbf{G}}^{\text{in},t} = \bar{\mathbf{G}}^{2D}$  for  $\bar{\mathbf{G}}^{\text{in},t}$ 
5   Solve the direct problem for  $\bar{\mathbf{E}}^t$  and  $\bar{\mathbf{E}}^{s,t}$ 
6    $\Delta \bar{\mathbf{E}}^s = \bar{\mathbf{E}}^s - \bar{\mathbf{E}}^{s,t}$ 
7   Solve the inverse linear problem  $\Delta \bar{\mathbf{E}}^s = \bar{\mathbf{G}}^{\text{in},t} \Delta \bar{\boldsymbol{\chi}} \bar{\mathbf{E}}^t$  for  $\Delta \bar{\boldsymbol{\chi}}$ 
8    $\bar{\boldsymbol{\chi}}^t \leftarrow \bar{\boldsymbol{\chi}}^{t-1} + \Delta \bar{\boldsymbol{\chi}}^t$ 
9    $t \leftarrow t + 1$ 
10 end
```

---

## Apêndice F

# Como inserir definições e outras coisas especiais

Um exemplo de definição:

**Definição 1.** *Projection Operator*

*Let  $X$  be a normed space over the field  $\mathbb{K} = \mathbb{R}$  or  $\mathbb{K} = \mathbb{C}$ . Let  $U \subset X$  be a closed subspace. A linear bounded operator  $\mathcal{P} : X \rightarrow X$  is called a projection operator on  $U$  if*

- $\mathcal{P}\{x\} \in U, \forall x \in X$  and
- $\mathcal{P}\{x\} = x, \forall x \in U$ .



# Apêndice G

## Dyadic Green's Function

The dyadic Green's function is an important tool for solving electromagnetic problems that include the radiation phenomenon. For this reason, this appendix aims to briefly discuss its definition and singularity. This text is based on chapter 7 of the book written by Chew (1995), which deepens the discussion and provides a better bibliographical reference on the topic.

### G.1 Dyadic Green's Function for Homogeneous Medium

A very general and essential problem for electromagnetic theory is that of radiation from a point source. This problem is fundamental for integral equations since the radiation of a current distribution is based on the contribution of all points at which the current is defined. That is, considering a generic scalar problem such as:

$$(\nabla^2 + k^2)\phi(\mathbf{r}) = s(\mathbf{r}) \quad (\text{G.1})$$

defined in a homogeneous region  $V$ , the solution can be obtained through:

$$\psi(\mathbf{r}) = - \int_V d\mathbf{r}' g(\mathbf{r}, \mathbf{r}') s(\mathbf{r}') \quad (\text{G.2})$$

where  $g(\mathbf{r}, \mathbf{r}')$  is the Green's function which is the solution to the equation:

$$(\nabla^2 + k^2)g(\mathbf{r}, \mathbf{r}') = -\delta(\mathbf{r} - \mathbf{r}') \quad (\text{G.3})$$

Particularly, this solution follows from the interpretation that  $s(\mathbf{r})$  is a linear superposition of point sources.

To obtain Green's function for a homogeneous and infinite medium, we will change the source position in the problem of eq.(G.3) to the origin of spherical coordinates:

$$(\nabla^2 + k^2)g(\mathbf{r}) = -\delta(\mathbf{r}) = -\delta(x)\delta(y)\delta(z) \quad (\text{G.4})$$

For  $\mathbf{r} \neq 0$ , the solution of (G.4) is given by:

$$g(\mathbf{r}) = C \frac{e^{jkr}}{r} + D \frac{e^{-jkr}}{r} \quad (\text{G.5})$$

where  $r = |\mathbf{r}|$ . Assuming that there are no sources at infinity, only the first term on the right-hand side of (G.5) is a solution:

$$g(\mathbf{r}) = C \frac{e^{jkr}}{r} \quad (\text{G.6})$$

The constant  $C$  is determined by calculating both sides of (G.4) in the singularity. To do this, we combine (G.6) into (G.4) and integrated into a small volume around the origin:

$$\int_{\Delta V} dV \nabla \cdot \nabla \frac{C e^{jkr}}{r} + \int_{\Delta V} dV k^2 \frac{C e^{jkr}}{r} = -1 \quad (\text{G.7})$$

The second integral of (G.7) tends to zero if  $\Delta V \rightarrow 0$ , since  $dV = 4\pi r^2 dr$ . Besides, Gauss' theorem can be used to transform the first integral into a surface one, and with that, we obtain:

$$\lim_{r \rightarrow 0} 4\pi r^2 \frac{d}{dr} C \frac{e^{jkr}}{r} = -1 \quad (\text{G.8})$$

or  $C = 1/4\pi$ . Also, the solution (G.6) can be generalized for the case in which the source is shifted to a point  $\mathbf{r}'$ . In this case, eq.(G.6) can be rewritten as:

$$g(\mathbf{r}, \mathbf{r}') = g(\mathbf{r} - \mathbf{r}') = \frac{e^{jk|\mathbf{r} - \mathbf{r}'|}}{4\pi|\mathbf{r} - \mathbf{r}'|} \quad (\text{G.9})$$

Solution (32) can be used to obtain Green's dyadic<sup>1</sup> function for the vector wave equation in a homogeneous and isotropic medium:

$$\nabla \times \nabla \times \mathbf{E}(\mathbf{r}) - k^2 \mathbf{E}(\mathbf{r}) = -j\omega\mu \mathbf{J}(\mathbf{r}) \quad (\text{G.10})$$

Since  $\nabla \times \nabla \times \mathbf{E} = -\nabla^2 \mathbf{E} + \nabla \nabla \cdot \mathbf{E}$  and that, according to the continuity equation,  $\nabla \cdot \mathbf{E} = \rho/\epsilon = \nabla \cdot \mathbf{J}/j\omega\epsilon$ , eq.(G.10) can be rewritten as:

$$\nabla^2 \mathbf{E}(\mathbf{r}) + k^2 \mathbf{E}(\mathbf{r}) = j\omega\mu \left[ \bar{\mathbf{I}} + \frac{\nabla \nabla}{k^2} \right] \cdot \mathbf{J}(\mathbf{r}) \quad (\text{G.11})$$

where  $\bar{\mathbf{I}}$  is the identity operator. In Cartesian coordinates, eq.(G.11) is actually three equations that can be solved just as it was done for the scalar equation. Thus, the solution for (G.11) is:

$$\mathbf{E}(\mathbf{r}) = -j\omega\mu \int_V d\mathbf{r}' g(\mathbf{r}' - \mathbf{r}) \left[ \bar{\mathbf{I}} + \frac{\nabla' \nabla'}{k^2} \right] \cdot \mathbf{J}(\mathbf{r}') \quad (\text{G.12})$$

---

<sup>1</sup>Dyad is an example of a second rank tensor, formed from two vectors and maps one vector field to another. Besides, they have the property of having nullspace of rank two. For a deeper discussion of tensors and their mathematical properties, we recommend reading Appendix B of (Chew, 1995).

Taking into account the vector identities  $\nabla g f = f \nabla g + g \nabla f$  and  $\nabla \cdot g \mathbf{F} = g \nabla \cdot \mathbf{F} + (\nabla g) \cdot \mathbf{F}$ , the following integrals can be rewritten as:

$$\int_V d\mathbf{r}' g(\mathbf{r}' - \mathbf{r}) \nabla' f(\mathbf{r}') = - \int_V [\nabla' g(\mathbf{r}' - \mathbf{r})] f(\mathbf{r}') \quad (\text{G.13})$$

$$\int_V d\mathbf{r}' [\nabla' g(\mathbf{r}' - \mathbf{r})] \nabla' \cdot \mathbf{J}(\mathbf{r}') = - \int_V d\mathbf{r}' \mathbf{J}(\mathbf{r}') \cdot \nabla' \nabla' g(\mathbf{r}' - \mathbf{r}) \quad (\text{G.14})$$

which allows us to rewrite (G.12) as:

$$\mathbf{E}(\mathbf{r}) = -j\omega\mu \int_V d\mathbf{r}' \mathbf{J}(\mathbf{r}') \cdot \left[ \bar{\mathbf{I}} + \frac{\nabla' \nabla'}{k^2} \right] g(\mathbf{r}', \mathbf{r}) \quad (\text{G.15})$$

However, as demonstrated in chapter 7 of (Chew, 1995), it is also possible to write eq.(G.15) as follows:

$$\mathbf{E}(\mathbf{r}) = j\omega\mu \int_V d\mathbf{r}' \mathbf{J}(\mathbf{r}') \cdot \bar{\mathbf{G}}(\mathbf{r}, \mathbf{r}') \quad (\text{G.16})$$

where:

$$\bar{\mathbf{G}}(\mathbf{r}, \mathbf{r}') = - \left[ \bar{\mathbf{I}} + \frac{\nabla \nabla}{k^2} \right] \frac{e^{jk|\mathbf{r} - \mathbf{r}'|}}{4\pi|\mathbf{r} - \mathbf{r}'|} \quad (\text{G.17})$$

## G.2 The Singularity of the Dyadic Green's Function

As can be seen in equation (G.13), Green's dyadic function has singularity for  $\mathbf{r} = \mathbf{r}'$ . That is, to calculate the field at a point within the region of the source  $\mathbf{J}$ , it is necessary to rewrite the integral equation (G.16) with the support of the exclusion volume  $V_\delta$  around the singularity point:

$$\mathbf{E}(\mathbf{r}) = \lim_{V_\delta \rightarrow 0} j\omega\mu \int_{V-V_\delta} d\mathbf{r}' \mathbf{J}(\mathbf{r}') \cdot \bar{\mathbf{G}}(\mathbf{r}', \mathbf{r}) \quad (\text{G.18})$$

In this way, the equation is defined in terms of an improper integral. Generally, improper integrals converge if there is a fixed limit regardless the shape of  $V_\delta$ . However, in the case of (G.18), a necessary condition for convergence is that  $\mathbf{J}$  must satisfy Holder's condition (Kellogg, 1953) in  $\mathbf{r} = \mathbf{r}'$ , in which there must be constants  $c$ ,  $A$ , and  $\alpha$  such that  $|\mathbf{J}(\mathbf{r}) - \mathbf{J}(\mathbf{r}')| \leq A|\mathbf{r}' - \mathbf{r}|^\alpha$  for  $|\mathbf{r}' - \mathbf{r}| < c$ . This condition is slightly stronger than general continuity. In addition, the derivatives of (G.17) do not allow the integral to converge in a traditional fashion, i.e., the principal value of the integral exists but depends on the chosen shape for  $V_\delta$ .

To calculate the limit of the term that includes those derived in eq.(G.18), we need to take into account both the integral over the region without the singularity and the region with

the singularity:

$$\begin{aligned} \nabla \nabla \cdot \int_V d\mathbf{r}' g(\mathbf{r}, \mathbf{r}') \mathbf{J}(\mathbf{r}') &= \lim_{V_\delta \rightarrow 0} \left[ \nabla \nabla \cdot \int_{V-V_\delta} d\mathbf{r}' g(\mathbf{r}, \mathbf{r}') \mathbf{J}(\mathbf{r}') \right. \\ &\quad \left. + \nabla \nabla \cdot \int_{V_\delta} d\mathbf{r}' g(\mathbf{r}, \mathbf{r}') \mathbf{J}(\mathbf{r}') \right] \end{aligned} \quad (\text{G.19})$$

where  $\mathbf{r} \in V_\delta$ . The first integral on the right-hand side of the equation does not contain  $\mathbf{r}$ , so the operator  $\nabla \nabla \cdot$  might enter into the integral. The second integral converges only if an operator  $\nabla$  is introduced in the integral. In this way, eq.(G.19) can be rewritten as:

$$\begin{aligned} \nabla \nabla \cdot \int_V d\mathbf{r}' g(\mathbf{r}, \mathbf{r}') \mathbf{J}(\mathbf{r}') &= \lim_{V_\delta \rightarrow 0} \left[ \int_{V-V_\delta} d\mathbf{r}' \nabla \nabla \cdot g(\mathbf{r}, \mathbf{r}') \mathbf{J}(\mathbf{r}') \right. \\ &\quad \left. - \nabla \int_{V_\delta} d\mathbf{r}' \nabla' g(\mathbf{r}, \mathbf{r}') \cdot \mathbf{J}(\mathbf{r}') \right] \end{aligned} \quad (\text{G.20})$$

Therefore, the two integrals on the right-hand side of (G.20) converge to a value that depends on the shape of  $V_\delta$ . However, the sum of the two integrals must be equal to the left-hand side, which does not depend on the shape chosen for  $V_\delta$ .

If we use the integration by parts and the relation  $\nabla \cdot \mathbf{J} = j\omega\rho$ , the second integral of (46) can be rewritten as:

$$\nabla \int_{V_\delta} d\mathbf{r}' \nabla' g(\mathbf{r}, \mathbf{r}') \cdot \mathbf{J}(\mathbf{r}') = \int_{S_\delta} dS' \mathbf{n} \cdot \mathbf{J}(\mathbf{r}') g(\mathbf{r}, \mathbf{r}') - j\omega \int_{V_\delta} g(\mathbf{r}, \mathbf{r}') \rho(\mathbf{r}') \quad (\text{G.21})$$

The second integral of (G.21) will tend to zero when  $V_\delta \rightarrow 0$  assuming that, for a volumetric current,  $\rho(\mathbf{r})$  is continuous. The first integral, on the other hand, has the term  $\mathbf{n} \cdot \mathbf{J}(\mathbf{r}')$  which is the surface charge on  $S_\delta$ , the surface of  $V_\delta$ . Because of this surface charge, the first integral is proportional to the field in  $\mathbf{r}$  and does not vary depending on the scale. In other words, it does not disappear when  $V_\delta \rightarrow 0$ , but depends on the shape of  $V_\delta$ . At the limit, eq.(G.21) is linearly proportional to  $\mathbf{J}(\mathbf{r})$ . Therefore, with the aid of  $\bar{\mathbf{L}}$ , a dyad which depends on the shape of  $V_\delta$ , we can rewrite (G.20) as:

$$\nabla \nabla \cdot \int_V d\mathbf{r}' g(\mathbf{r}, \mathbf{r}') \mathbf{J}(\mathbf{r}') = \lim_{V_\delta \rightarrow 0} \int_{V-V_\delta} d\mathbf{r}' \nabla \nabla \cdot g(\mathbf{r}, \mathbf{r}') \cdot \mathbf{J}(\mathbf{r}') - \bar{\mathbf{L}} \cdot \mathbf{J}(\mathbf{r}) \quad (\text{G.22})$$

Using this result in (G.16), we will obtain:

$$\mathbf{E}(\mathbf{r}) = j\omega\mu \lim_{V_\delta \rightarrow 0} \int_{V-V_\delta} d\mathbf{r}' \tilde{\mathbf{G}}(\mathbf{r}, \mathbf{r}') \cdot \mathbf{J}(\mathbf{r}') + \frac{\tilde{\mathbf{L}} \cdot \mathbf{J}(\mathbf{r})}{j\omega\epsilon} \quad (\text{G.23})$$

The integral of (G.23) is equivalent to the principal value integral operator whose notation is expressed by  $P.V. \int_V$ , that is:

$$\mathbf{E}(\mathbf{r}) = j\omega\mu P.V. \int_V d\mathbf{r}' \tilde{\mathbf{G}}(\mathbf{r}, \mathbf{r}') \cdot \mathbf{J}(\mathbf{r}') + \frac{\tilde{\mathbf{L}} \cdot \mathbf{J}(\mathbf{r})}{j\omega\epsilon}, \quad \forall \mathbf{r} \in V \quad (\text{G.24})$$

Therefore, although the two terms on the right-hand side of (G.24) are dependent on the choice of  $V_\delta$ , the  $\mathbf{E}$  field is unique. This method for determining the field value in the region of singularity is known as the Principal Volume Method (Van Bladel, 1961).

Physically, this method of solution corresponds to opening a space around the observation point within the current region. Since this current is discontinuous on the surface of that space, the surface accumulates charges which, when decreasing the space to an infinitesimal volume, have an electrostatic nature. This electrostatic field satisfies the Laplace equation and depends on the shape of that space, no matter how small it is. Therefore, the second term in eq.(G.24) aims to remove the contribution from this electrostatic field, since it is not part of the problem but has been added as a mathematical resource.

Finally, some values for  $\tilde{\mathbf{L}}$  for certain types of exclusion volumes have already been determined in the literature (Shung-Wu Lee et al., 1980; Yaghjian, 1980). In addition, generally, the trace  $[\tilde{\mathbf{L}}] = 1$  (Yaghjian, 1980). Board G.1 shows some values for  $\tilde{\mathbf{L}}$  considering some geometric shapes:

Tabela G.1: Dyad  $\tilde{\mathbf{L}}$  values for different shapes of exclusion volume applied to the singularity of dyadic Green's function. Sources: (Shung-Wu Lee et al., 1980; Yaghjian, 1980).

Geometric shape	$\tilde{\mathbf{L}}$
Spheres or cubes	$\frac{\tilde{\mathbf{I}}}{3}$
Disks	$\mathbf{zz}$
Needles	$\frac{\mathbf{xx} + \mathbf{yy}}{2}$

### G.3 Dyadic Green's Function for Inhomogeneous Medium

To determine the dyadic Green function for a non-homogeneous medium, we will assume a region  $V_1$  and another  $V_2 \subset V_1$ . The contrasts of these media in relation to the vacuum

will be denominated  $\chi_1$  and  $\chi_2$ , respectively. We can write  $\chi_2$  as:

$$\chi_2(\mathbf{r}) = \chi_1(\mathbf{r}) + \Delta\chi(\mathbf{r}) \quad (\text{G.25})$$

Consequently, the integral equation for the electric field at any point in space can be written as:

$$\mathbf{E}(\mathbf{r}) = \mathbf{E}_i(\mathbf{r}) + k_0^2 \int_{V_1} d\mathbf{r}' \bar{\mathbf{G}}(\mathbf{r}, \mathbf{r}') \cdot \chi_1(\mathbf{r}') \mathbf{E}(\mathbf{r}') + k_0^2 \int_{V_1} d\mathbf{r}' \bar{\mathbf{G}}(\mathbf{r}, \mathbf{r}') \cdot \chi_2(\mathbf{r}') \mathbf{E}(\mathbf{r}') \quad (\text{G.26})$$

However,  $\mathbf{E}$  can be interpreted as the sum of the scattered field and by  $\chi_1$  for  $\mathbf{r} \in V_1$ . The former is due to the *excess* of contrast in  $V_2$  when the incident field is the field that propagates in an inhomogeneous medium characterized by  $\epsilon_0$  for  $\mathbf{r} \notin V_1$ . Mathematically, this is equivalent to:

$$\mathbf{E}(\mathbf{r}) = \mathbf{E}_1(\mathbf{r}) + k_0^2 \int_{V_2} d\mathbf{r}' \bar{\mathbf{G}}_{\text{in}}(\mathbf{r}, \mathbf{r}') \cdot \chi_2(\mathbf{r}') \mathbf{E}(\mathbf{r}') \quad (\text{G.27})$$

where  $\mathbf{E}_1$  is given by:

$$\mathbf{E}_1(\mathbf{r}) = \mathbf{E}_i(\mathbf{r}) + k_0^2 \int_{V_1} d\mathbf{r}' \bar{\mathbf{G}}(\mathbf{r}, \mathbf{r}') \cdot \chi_1(\mathbf{r}') \mathbf{E}(\mathbf{r}') \quad (\text{G.28})$$

and the Green's function for the inhomogeneous medium satisfies:

$$\bar{\mathbf{G}}_{\text{in}}(\mathbf{r}, \mathbf{r}') = \bar{\mathbf{G}}(\mathbf{r}, \mathbf{r}') + k_0^2 \int_{V_1} d\mathbf{r}'' \bar{\mathbf{G}}(\mathbf{r}, \mathbf{r}'') \cdot \chi_1(\mathbf{r}'') \bar{\mathbf{G}}_{\text{in}}(\mathbf{r}'', \mathbf{r}') \quad (\text{G.29})$$

Analytical solutions for (G.29) are rarely available. Frequently, when inhomogeneous modeling for Green's function is necessary, numerical methods are employed to estimate this function.

## Apêndice H

### Integral Equation Formulation

Integral equations are an important method for electromagnetic theory. In this appendix, the derivation of the Electric Field Integral Equation from wave equation and dyadic Green's function will be discussed. The text is based on section 3.4 of (Chew, 2009).

Let us suppose a volume  $V_{inf}$  whose surface is  $S_{inf}$  in which there is a source  $J_2$  within a region  $V_2$  and another source  $J_1$  for a region  $V_1$  separate from  $V_2$  for a closed surface  $S$  (see Figure H.1). Assuming that the medium in  $V_1$  is homogeneous with properties  $\epsilon_1$  and  $\mu_1$ , the relationship between electric field  $\mathbf{E}(\mathbf{r})$  and a current distribution  $\mathbf{J}(\mathbf{r})$  representing currents  $J_1$  and  $J_2$  is given by the wave equation:

$$\nabla \times \nabla \times \mathbf{E}(\mathbf{r}) - \omega^2 \epsilon_1 \mu_1 \mathbf{E}(\mathbf{r}) = -j\omega \mu_1 \mathbf{J}(\mathbf{r}) \quad (\text{H.1})$$

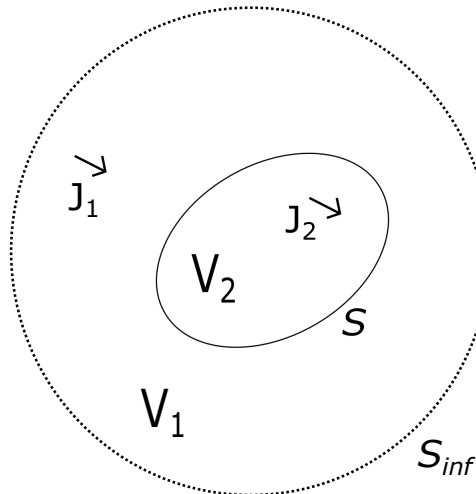


Figura H.1: Derivation of integral equation.

The solution to this equation is obtained with the support of the dyadic Green's function  $\bar{\mathbf{G}}(\mathbf{r}, \mathbf{r}')$  for a homogeneous and isotropic medium, where  $\mathbf{r}'$  is an observation point in the source

region. Under these conditions, the Green's function is a solution to the following equation:

$$\nabla \times \nabla \times \bar{\mathbf{G}}(\mathbf{r}, \mathbf{r}') - \omega^2 \varepsilon_1 \mu_1 \bar{\mathbf{G}}(\mathbf{r}, \mathbf{r}') = -\bar{\mathbf{I}} \delta(\mathbf{r} - \mathbf{r}') \quad (\text{H.2})$$

Postmultiplying (H.1) by  $\bar{\mathbf{G}}(\mathbf{r}, \mathbf{r}')$ , premultiplying (H.2) by  $\mathbf{E}(\mathbf{r})$ , and then subtracting the resultant equations, we will obtain:

$$\begin{aligned} \mathbf{E}(\mathbf{r}) \cdot \nabla \times \nabla \times \bar{\mathbf{G}}(\mathbf{r}, \mathbf{r}') - \nabla \times \nabla \times \mathbf{E}(\mathbf{r}) \cdot \bar{\mathbf{G}}(\mathbf{r}, \mathbf{r}') \\ = j\omega\mu_1 \mathbf{J}(\mathbf{r}) \cdot \bar{\mathbf{G}}(\mathbf{r}, \mathbf{r}') - \mathbf{E}(\mathbf{r}) \delta(\mathbf{r} - \mathbf{r}') \end{aligned} \quad (\text{H.3})$$

If we integrate both sides of the equation (H.3) in the volume  $V_1$ , we get:

$$\int_{V_1} dV [\mathbf{E}(\mathbf{r}) \cdot \nabla \times \nabla \times \bar{\mathbf{G}}(\mathbf{r}, \mathbf{r}') - \nabla \times \nabla \times \mathbf{E}(\mathbf{r}) \cdot \bar{\mathbf{G}}(\mathbf{r}, \mathbf{r}')] = \mathbf{E}_1(\mathbf{r}') - \mathbf{E}(\mathbf{r}')$$

in which:

$$\mathbf{E}(\mathbf{r}') = \int_{V_1} d\mathbf{r} \delta(\mathbf{r} - \mathbf{r}') \mathbf{E}(\mathbf{r}) \quad (\text{H.4})$$

$$\mathbf{E}_1(\mathbf{r}') = j\omega\mu_1 \int_{V_1} d\mathbf{r} \mathbf{J}_1(\mathbf{r}) \cdot \bar{\mathbf{G}}(\mathbf{r}, \mathbf{r}') \quad (\text{H.5})$$

The field  $\mathbf{E}_1$  is produced by the source  $\mathbf{J}_1$  in  $V_1$ . Since  $\mathbf{J}_2$  is not in  $V_1$ , it does not contribute to the integral.

Through the identity:

$$\begin{aligned} -\nabla \cdot [\mathbf{E}(\mathbf{r}) \times \nabla \times \bar{\mathbf{G}}(\mathbf{r}, \mathbf{r}') + \nabla \times \mathbf{E}(\mathbf{r}) \times \bar{\mathbf{G}}(\mathbf{r}, \mathbf{r}')] \\ = \mathbf{E}(\mathbf{r}) \cdot \nabla \times \nabla \times \bar{\mathbf{G}}(\mathbf{r}, \mathbf{r}') - \nabla \times \nabla \times \mathbf{E}(\mathbf{r}) \cdot \bar{\mathbf{G}}(\mathbf{r}, \mathbf{r}') \end{aligned} \quad (\text{H.6})$$

we can apply Gauss' theorem and rewrite eq. (H.4) as:

$$\mathbf{E}_1(\mathbf{r}') - \mathbf{E}(\mathbf{r}') = \oint_{S+S_{inf}} dS \mathbf{n} \cdot [\mathbf{E}(\mathbf{r}) \times \nabla \times \bar{\mathbf{G}}(\mathbf{r}, \mathbf{r}') + \nabla \times \mathbf{E}(\mathbf{r}) \times \bar{\mathbf{G}}(\mathbf{r}, \mathbf{r}')] \quad (\text{H.7})$$

$$\begin{aligned} = \oint_{S+S_{inf}} dS \cdot [\mathbf{n} \times \mathbf{E}(\mathbf{r}) \cdot \nabla \times \bar{\mathbf{G}}(\mathbf{r}, \mathbf{r}') \\ - j\omega\mu_1 \mathbf{n} \times \mathbf{H}(\mathbf{r}) \cdot \bar{\mathbf{G}}(\mathbf{r}, \mathbf{r}')] \end{aligned} \quad (\text{H.8})$$

where  $\mathbf{n}$  is the normal vector on the surface  $S$  which points outwards. Depending on the position of  $\mathbf{r}'$ , we have different results for eq.(H.8):

$$\mathbf{E}_1(\mathbf{r}') - \oint_{S+S_{inf}} dS [\mathbf{n} \times \mathbf{E}(\mathbf{r}) \cdot \nabla \times \bar{\mathbf{G}}(\mathbf{r}, \mathbf{r}') - j\omega\mu_1 \mathbf{n} \times \mathbf{H}(\mathbf{r}) \cdot \bar{\mathbf{G}}(\mathbf{r}, \mathbf{r}')] = \begin{cases} \mathbf{E}(\mathbf{r}'), & \mathbf{r}' \in V_1 \\ 0, & \mathbf{r}' \notin V_1 \end{cases} \quad (\text{H.9})$$



As the distance between the field observation point and the source point increases, the integral over  $S_{inf}$  vanishes. Although the surface of  $S_{inf}$  increases with this distance, the two terms on the left-hand side of the eq.(H.9) will cancel each other out so that the integrator decays.

Swapping the observations points  $\mathbf{r}$  and  $\mathbf{r}'$ , we get:

$$\mathbf{E}_1(\mathbf{r}) - \oint_S dS' [\mathbf{n}' \times \mathbf{E}(\mathbf{r}') \cdot \nabla' \times \bar{\mathbf{G}}(\mathbf{r}', \mathbf{r}) - j\omega\mu_1 \mathbf{n}' \times \mathbf{H}(\mathbf{r}') \cdot \bar{\mathbf{G}}(\mathbf{r}', \mathbf{r})] = \begin{cases} \mathbf{E}(\mathbf{r}), & \mathbf{r} \in V_1 \\ 0, & \mathbf{r} \in V_2 \end{cases} \quad (\text{H.10})$$

From the following transposition properties:

$$\nabla \times \bar{\mathbf{G}}(\mathbf{r}, \mathbf{r}') = [\nabla' \times \bar{\mathbf{G}}(\mathbf{r}', \mathbf{r})]^t \quad (\text{H.11})$$

$$\bar{\mathbf{G}}(\mathbf{r}, \mathbf{r}') = [\bar{\mathbf{G}}(\mathbf{r}', \mathbf{r})]^t \quad (\text{H.12})$$

we can calculate the transpose of eq.(H.10) by:

$$\mathbf{E}_1(\mathbf{r}) - \oint_S dS' [\nabla \times \bar{\mathbf{G}}(\mathbf{r}', \mathbf{r}) \cdot \mathbf{n}' \times \mathbf{E}(\mathbf{r}') - j\omega\mu_1 \bar{\mathbf{G}}(\mathbf{r}', \mathbf{r}) \cdot \mathbf{n}' \times \mathbf{H}(\mathbf{r}')] = \begin{cases} \mathbf{E}(\mathbf{r}), & \mathbf{r} \in V_1 \\ 0, & \mathbf{r} \in V_2 \end{cases} \quad (\text{H.13})$$

Letting  $\mathbf{M}_s(\mathbf{r}') = -\mathbf{n}' \times \mathbf{E}(\mathbf{r}')$  and  $\mathbf{J}_s(\mathbf{r}') = \mathbf{n}' \times \mathbf{H}(\mathbf{r}')$ , we may write the eq.(H.13) in terms of equivalent surface electric and magnetic currents imposed on the  $S$  surface. Thus, the equation becomes:

$$\mathbf{E}_1(\mathbf{r}) + \oint_S dS' [\bar{\mathbf{G}}(\mathbf{r}', \mathbf{r}) \cdot \mathbf{M}_s(\mathbf{r}') + j\omega\mu_1 \bar{\mathbf{G}}(\mathbf{r}', \mathbf{r}) \cdot \mathbf{J}_s(\mathbf{r}')] = \begin{cases} \mathbf{E}(\mathbf{r}), & \mathbf{r} \in V_1 \\ 0, & \mathbf{r} \in V_2 \end{cases} \quad (\text{H.14})$$

In other words, the field observed at a point in the region  $V_1$  is due to the source  $\mathbf{J}_1$  in  $V_1$  and the equivalent currents  $\mathbf{M}_s$  and  $\mathbf{J}_s$  on the surface of  $S$  which has the same effect as  $\mathbf{J}_2$ . It is also worth noting that (H.14) also applies to other types of equivalent currents, such as induction currents due to the penetration of an incident field in a dielectric material. In these cases, eq.(H.14) can simply be written as:

$$\mathbf{E}(\mathbf{r}) = \mathbf{E}^i(\mathbf{r}) + j\omega\mu \oint_S dS' \bar{\mathbf{G}}(\mathbf{r}', \mathbf{r}) \cdot \mathbf{J}(\mathbf{r}') \quad (\text{H.15})$$

# Apêndice I

## Functional Analysis

An important issue within the scope of integral equations is functional analysis since it is a problem composed of an operator applied to functions of a vector space. Therefore, this chapter is a brief approach to the concepts of normed spaces and operators which will be a reference for discussions found in the dissertation. This text was written based on Appendix A of (Kirsch, 2011). Therefore, more information can be found in this reference and a more in-depth study can also be found in (Lebedev et al., 1996).

### I.1 Normed and Hilbert Spaces

Let us start with some basic definitions:

**Definição 2. Inner Product**

Let  $X$  be a vector space defined on  $\mathbb{K} = \mathbb{R}$  or  $\mathbb{K} = \mathbb{C}$ . The scalar product is a mapping

$$\langle \cdot, \cdot \rangle : X \times X \rightarrow \mathbb{K}$$

with the following properties:

1.  $\langle x + y, z \rangle = \langle x, z \rangle + \langle y, z \rangle, \forall x, y, z \in X;$
2.  $\langle x, y + z \rangle = \langle x, y \rangle + \langle x, z \rangle, \forall x, y, z \in X;$
3.  $\langle \alpha x, y \rangle = \alpha \langle x, y \rangle, \forall x, y \in X \text{ and } \alpha \in \mathbb{K};$
4.  $\langle x, y \rangle = \overline{\langle y, x \rangle}, \forall x, y \in X;$
5.  $\langle x, x \rangle \in \mathbb{R} \text{ and } \langle x, x \rangle \geq 0, \forall x \in X;$
6.  $\langle x, x \rangle > 0 \text{ if } x \neq 0;$
7.  $\langle x, \alpha y \rangle = \bar{\alpha} \langle x, y \rangle, \forall x, y \in X \text{ and } \alpha \in \mathbb{K}.$

**Definição 3. Pre-Hilbert space**

A vector space  $X$  over  $\mathbb{K}$  with inner product  $\langle \cdot, \cdot \rangle$  is called a pre-Hilbert space over  $\mathbb{K}$ .

**Definição 4. Norm**

Let  $X$  be a vector space over the field  $\mathbb{K} = \mathbb{R}$  or  $\mathbb{K} = \mathbb{C}$ . A norm on  $X$  is a mapping

$$\|\cdot\| : X \rightarrow \mathbb{R}$$

with the following properties:

1.  $\|x\| > 0$ ,  $\forall x \in X$  with  $x \neq 0$ ;
2.  $\|\alpha x\| = |\alpha| \|x\|$ ,  $\forall x \in X$  and  $\alpha \in \mathbb{K}$ ;
3.  $\|x+y\| \leq \|x\| + \|y\|$  and  $\|x-y\| \geq \left| \|x\| - \|y\| \right|$ ,  $\forall x, y \in X$  (Triangle Inequality).

A vector space  $X$  over  $\mathbb{K}$  with norm  $\|\cdot\|$  is called normed space over  $\mathbb{K}$

Now, the following theorem is introduced:

**Teorema 5.** Let  $X$  be a pre-Hilbert space. The mapping  $\|\cdot\| : X \rightarrow \mathbb{R}$  defined by

$$\|x\| := \sqrt{\langle x, x \rangle}, \quad x \in X$$

is a norm. Furthermore:

1.  $|(x, y)| \leq \|x\| \|y\|$ ,  $\forall x, y \in X$  (Cauchy-Schwarz inequality);
2.  $\|x \pm y\|^2 = \|x\|^2 + \|y\|^2 \pm 2\Re\{\langle x, y \rangle\}$ ,  $\forall x, y \in X$  (binomial formula);
3.  $\|x+y\|^2 + \|x-y\|^2 = 2\|x\|^2 + 2\|y\|^2$ ,  $\forall x, y \in X$ .

An example of a pre-Hilbert space over  $\mathbb{R}$  is the space of real or complex continuous functions over the interval  $[a, b]$ , denoted by  $C[a, b]$ , whose internal product is:

$$(x, y)_{L^2} := \int_a^b x(t) \overline{y(t)} dt, \quad x, y \in C[a, b] \quad (\text{I.1})$$

and whose norm is Euclidean, i.e.:

$$\|x\|_{L^2} := \sqrt{\langle x, x \rangle} = \sqrt{\int_a^b |x(t)|^2 dt}, \quad x \in C[a, b] \quad (\text{I.2})$$

When a norm is defined for a vector space, it introduces as well a topology. Based on the norm definition, it is also possible to define open, closed, compact sets, and others features. Firstly, we will introduce the definition of a ball with radius  $r$  and center  $x \in X$  which will be useful for the next definitions:

$$K(x, r) := \{y \in X : \|y - x\| < r\}, \quad K[x, r] := \{y \in X : \|y - x\| \leq r\}$$

**Definição 6.** Let  $X$  be a normed space over the field  $\mathbb{K} = \mathbb{R}$  or  $\mathbb{C}$ .

1. A subset  $M \subset X$  is called bounded if there exists  $r > 0$  with  $M \subset K(x, r)$ . The set  $M \subset X$  is called open if for every  $x \in M$  there exists  $\varepsilon > 0$  such that  $K(x, \varepsilon) \subset M$ . The set  $M \subset X$  is called closed if the complement  $X \setminus M$  is open.
2. A sequence  $(x_k)_k \subset X$  is called bounded if there exists  $c > 0$  such that  $\|x_k\| < c$  for all  $k$ . The sequence  $(x_k)_k \subset X$  is called convergent if there exist  $x \in X$  such that  $\|x - x_k\|$

converges to zero in  $\mathbb{R}$ . We denote the limit by  $x = \lim_{k \rightarrow \infty} x_k$ , or we write  $x_k \rightarrow x$  as  $k \rightarrow \infty$ . The sequence  $(x_k)_k \subset X$  is called a *Cauchy sequence* if for every  $\varepsilon > 0$  there exists  $N \in \mathbb{N}$  with  $\|x_m - x_k\| < \varepsilon$  for all  $m, k \geq N$ .

3. Let  $(x_k)_k \subset X$  be a sequence.  $x \in X$  is called an *accumulation point* if there exists a subsequence  $(a_{k_n})_n$  that converges to  $x$ .
4. A set  $M \subset X$  is called *compact* if every sequence in  $M$  has an accumulation point in  $M$ .

A property derived from these concepts is that a set  $M$  is closed if and only if the limit of each convergent sequence  $(x_k)_k \subset M$  also belongs to  $M$ . Furthermore, we call the sets  $M^\circ := \{x \in M : \text{there exists } \varepsilon > 0 \text{ with } K(x, \varepsilon) \subset M\}$  and  $\overline{M} := \{x \in X : \text{there exists } (x_k)_k \subset M \text{ with } x = \lim_{k \rightarrow \infty} x_k\}$  interior and closure of  $M$ , respectively. In addition, the set  $M \subset X$  is said to be dense in  $X$  if  $\overline{M} = X$ .

We can exemplify some of these concepts defined through the set  $X = C[0,1]$  on  $\mathbb{R}$  and  $x_k(t) = t^k$ ,  $t \in [0,1]$ ,  $k \in \mathbb{N}$  with norm  $\|\cdot\|_{L^2}$ . In this case, the sequence  $(x_k)$  converges to zero. The dependence between topological properties and the definition of the norm of a set is usual; however, this is not the case with finite-dimensional spaces in which the properties are independent.

**Teorema 7.** *Let  $X$  be a finite-dimensional space with norms  $\|\cdot\|_1$  and  $\|\cdot\|_2$ . Then both norms are equivalent, i.e., there exist constants  $c_2 \geq c_1 > 0$  with*

$$c_1 \|x\|_1 \leq \|x\|_2 \leq c_2 \|x\|_1, \quad \forall x \in X.$$

Therefore, each ball defined on  $\|\cdot\|_1$  contains a ball defined on  $\|\cdot\|_2$  and vice versa.

**Teorema 8.** *Let  $X$  be a normed space over  $\mathbb{K}$  and  $M \subset X$  be a subset.*

1.  $M$  is closed if and only if  $M = \overline{M}$ , and  $M$  is open if and only if  $M = M^\circ$ .
2. If  $M \neq X$  is a linear subspace, then  $M^\circ = \emptyset$ , and  $\overline{M}$  is also a linear subspace.
3. In finite-dimensional spaces, every subspace is closed.
4. Every compact set is closed and bounded. In finite-dimensional spaces, the reverse is also true (Theorem of Bolzano-Weierstrass): In a finite-dimensional normed space, every closed and bounded set is compact.

From now on, we can introduce an important concept in functional analysis, which is completeness. This concept is a crucial feature of the set of real numbers, for example.

**Definição 9.** *Banach Space, Hilbert Space*

A normed space  $X$  over  $\mathbb{K}$  is called *complete* or a *Banach Space* if every Cauchy sequence converges in  $X$ . A complete pre-Hilbert space is called a *Hilbert space*.

The spaces  $\mathbb{C}^n$  and  $\mathbb{R}^n$  with their canonical inner products are examples of Hilbert spaces. The space  $C[a,b]$  with inner product  $\langle \cdot, \cdot \rangle_{L^2}$  is not an example. However, any normed or pre-Hilbert space can be “completed”, i.e., a smaller Banach or Hilbert space that extends  $X$  can be defined. Let us see in the next theorem:

**Teorema 10.** *Let  $X$  be a normed space with norm  $\|\cdot\|_X$ . There exist a Banach space  $(\tilde{X}, \|\cdot\|_{\tilde{X}})$*

and a injective linear operator  $\mathcal{J} : X \rightarrow \tilde{X}$  such that

1. The range  $J(X) \subset \tilde{X}$  is dense in  $\tilde{X}$ , and
2.  $\|\mathcal{J}\{x\}\|_{\tilde{X}} = \|x\|_X, \forall x \in X$ , i.e.,  $\mathcal{J}$  preserves the norm.

Furthermore,  $\tilde{X}$  is uniquely determined in the sense that if  $\tilde{X}$  is a second space with properties 1 and 2 with respect to a linear injective operator  $\hat{\mathcal{J}}$ , then the operator  $\hat{\mathcal{J}}\mathcal{J}^{-1} : \mathcal{J}(X) \rightarrow \hat{\mathcal{J}}(X)$  has an extension to a norm-preserving isomorphism from  $\tilde{X}$  onto  $\hat{X}$ . In other words,  $\tilde{X}$  and  $\hat{X}$  can be identified.

For the pre-Hilbert space  $(C[a,b], \langle \cdot, \cdot \rangle_{L^2})$  to be complete, it is necessary to make use of Lebesgue's integration theory (Bartle, 1995). From the Lebesgue measure and its definitions of measurability and integrability, the complete space of  $(C[a,b], \langle \cdot, \cdot \rangle_{L^2})$  will be denoted as  $L^2(a,b)$ . For this, we first define the vector space  $\mathcal{L}^2(a,b) := \{x : (a,b) \rightarrow \mathbb{C} : x \text{ is measurable and } |x|^2 \text{ integrable}\}$ , in which scalar addition and multiplication are defined pointwise in almost everywhere. From this,  $\mathcal{L}^2(a,b)$  is a vector space since for  $x, y \in \mathcal{L}^2(a,b)$  and  $\alpha \in \mathbb{C}$ ,  $x+y$  and  $\alpha x$  are also measurable and  $\alpha x, x+y \in \mathcal{L}^2(a,b)$ . We define a sesquilinear form on  $\mathcal{L}^2(a,b)$  by:

$$\langle x, y \rangle := \int_a^b x(t) \overline{y(t)} dt, \quad x, y \in \mathcal{L}^2(a,b) \quad (\text{I.3})$$

However, (I.3) is not an inner product on  $\mathcal{L}^2(a,b)$  since  $\langle x, y \rangle = 0$  only implies that  $x$  vanishes almost everywhere, i.e., that  $x \in \mathcal{N}$ , where  $\mathcal{N} := \{x \in \mathcal{L}^2(a,b) : x(t) = 0 \text{ almost everywhere on } (a,b)\}$ . Now, we define  $L^2(a,b)$  as the factor space

$$L^2(a,b) := \mathcal{L}^2(a,b) \setminus \mathcal{N} \quad (\text{I.4})$$

and equip  $L^2(a,b)$  with the inner product

$$\langle [x], [y] \rangle_{L^2} := \int_a^b x(t) \overline{y(t)} dt, \quad x \in [x], y \in [y]$$

where  $[x], [y] \in L^2(a,b)$  are equivalence classes of functions in  $\mathcal{L}^2(a,b)$ . From now on, we will write  $x \in L^2(a,b)$  instead of  $x \in [x] \in L^2(a,b)$ . Finally,  $L^2(a,b)$  is a Hilbert space and contains  $C[a,b]$  as a dense subspace.

## I.2 Linear Bounded and Compact Operators

In this section, for all definitions and theorems, we will assume that  $X$  and  $Y$  are normed spaces and  $\mathcal{A} : X \rightarrow Y$  is a linear operator.

**Definição 11.** *Boundedness, Norm of  $\mathcal{A}$*

The linear operator  $\mathcal{A}$  is called bounded if there exists  $c > 0$  such that

$$\|\mathcal{A}\{x\}\| \leq c\|x\|, \quad \forall x \in X.$$

The smallest of these constants is called the norm of  $\mathcal{A}$ , i.e.,

$$\|\mathcal{A}\| := \sup_{x \neq 0} \frac{\|\mathcal{A}\{x\}\|}{\|x\|}.$$

**Teorema 12.** *The following assertions are equivalent:*

1.  $\mathcal{A}$  is bounded.
2.  $\mathcal{A}$  is continuous at  $x = 0$ , i.e,  $x_j \rightarrow 0$  implies that  $\mathcal{A}\{x_j\} \rightarrow 0$ .
3.  $\mathcal{A}$  is continuous for every  $x \in X$ .

Hence,  $\mathcal{L}(X, Y)$  can be understood as all bounded linear mappings from  $X$  to  $Y$  in which the operator norm is a normed space.

**Teorema 13.** 1. Let  $k \in L^2((c, d) \times (a, b))$ . The operator

$$\mathcal{A}\{x(t)\} := \int_a^b k(t, s)x(s)ds, \quad t \in (c, d), \quad x \in L^2(a, b) \quad (\text{I.5})$$

is well-defined, linear, and bounded from  $L^2(a, b)$  into  $L^2(c, d)$ . Furthermore,

$$\|\mathcal{A}\|_{L^2} \leq \int_c^d \int_a^b |k(t, s)| ds dt.$$

2. Let  $k$  be continuous on  $[c, d] \times [a, b]$ . Then  $\mathcal{A}$  is also well-defined, linear, and bounded from  $C[a, b]$  into  $C[c, d]$  and

$$\|\mathcal{A}\|_{\infty} = \max_{t \in [c, d]} \int_a^b |k(t, s)| ds.$$

Within the context of integral operators, those whose kernel is weakly singular are also of interest. Mathematically, a kernel  $k$  is weakly singular in  $[a, b] \times [a, b]$  if  $k$  is defined and continuous for every  $t, s \in [a, b]$ ,  $t \neq s$ , and there is a  $c > 0$  and  $\alpha \in [0, 1)$  such that

$$|k(t, s)| \leq c|t - s|^{-\alpha}, \quad \forall t, s \in [a, b], t \neq s.$$

**Teorema 14.** Let  $k$  be weakly singular on  $[a, b]$ . Then the integral operator  $\mathcal{A}$  defined by (I.5) for  $[c, d] = [a, b]$ , is well-defined and bounded as an operator in  $L^2(a, b)$  as well as in  $C[a, b]$ .

Another important definition for the study is the adjunct operator:

**Teorema 15.** *Adjoint Operator*

Let  $\mathcal{A} : X \rightarrow Y$  be a linear and bounded operator between Hilbert spaces. Then there exists one and only linear bounded operator  $\mathcal{A}^* : Y \rightarrow X$  with the property

$$\langle \mathcal{A}\{x\}, y \rangle = \langle x, \mathcal{A}^*\{y\} \rangle \quad \forall x \in X, y \in Y.$$

This operator  $\mathcal{A}^* : Y \rightarrow X$  is called the adjoint operator to  $\mathcal{A}$ . For  $X = Y$ , the operator  $\mathcal{A}$  is

called self-adjoint if  $\mathcal{A}^* = \mathcal{A}$ .

To exemplify the adjoint operators, let  $X = L^2(a,b)$ ,  $Y = L^2(c,d)$ , and  $k \in L^2((c,d) \times (a,b))$ . The adjoint operator  $\mathcal{A}^*$  of the integral operator

$$\mathcal{A}\{x(t)\} = \int_a^b k(t,s)x(s)ds, \quad t \in (c,d), x \in L^2(a,b)$$

which is given by

$$\mathcal{A}^*\{y(t)\} = \int_c^d \overline{k(s,t)}y(s)ds, \quad t \in (a,b), y \in L^2(c,d).$$

Finally, a final important definition is the compact operators:

**Definição 16.** *Compact Operator*

The operator  $\mathcal{K} : X \rightarrow Y$  is called compact if it maps every bounded set  $S$  into a relatively compact set  $\mathcal{K}(S)$ .

A set  $M \subset Y$  is called relatively compact if every bounded sequence  $(y_j) \subset M$  has an accumulation point in  $\overline{M}$ , i.e., if the closure  $\overline{M}$  is compact. The set of all compact operators from  $X$  to  $Y$  is a closed subspace of  $\mathcal{L}(X,Y)$ . In respect to integral operators:

**Teorema 17.** *Compactness of integral operators*

1. Let  $k \in L^2((c,d) \times (a,b))$ . The operator  $\mathcal{K} : L^2(a,b) \rightarrow L^2(c,d)$ , defined by

$$\mathcal{K}\{x(t)\} := \int_a^b k(t,s)x(s)ds, \quad t \in (c,d), x \in L^2(a,b) \tag{I.6}$$

is compact from  $L^2(a,b)$  into  $L^2(c,d)$ .

2. Let  $k$  be continuous on  $[c,d] \times [a,b]$  or weakly singular on  $[a,b] \times [a,b]$  (in this case  $[c,d] = [a,b]$ ). Then  $\mathcal{K}$  defined by (I.6) is also compact as an operator from  $C[a,b]$  into  $C[c,d]$ .

## Apêndice J

### Shape metrics

In an Electromagnetic Inverse Scattering (EISP) problem, we are interested in detecting objects in an image. These objects have three characteristics: position, shape and contrast value. In the literature of this problem, there are measures to evaluate the error of a method when estimating the contrast of an object. However, up to the date of this thesis, there is no reference for measuring position and shape. This appendix aims to investigate and develop ways to measure the quality of an algorithm in recovering shapes. In addition, this annex is dedicated to analyzing the case of reconstructing a single object within the image.

The identification of objects in an image is a classic problem in the area of Image Processing. Traditionally, the goal is to recognize patterns in figures and to identify those patterns. In EISP, identifying the object is not the purpose, in the sense of comparing it with a database, but only to retrieve shapes. This kind of problem can be addressed with methods known as Marching Squares, which generate contours from a threshold process.

Suppose an algorithm designed to recover an image. The original and the recovered images are show in Figure J.1. If we apply the Marching Squares algorithm do obtain the contours using the same threshold for the recovered image as in Algorithm ??, we will obtain the results which are in J.2.

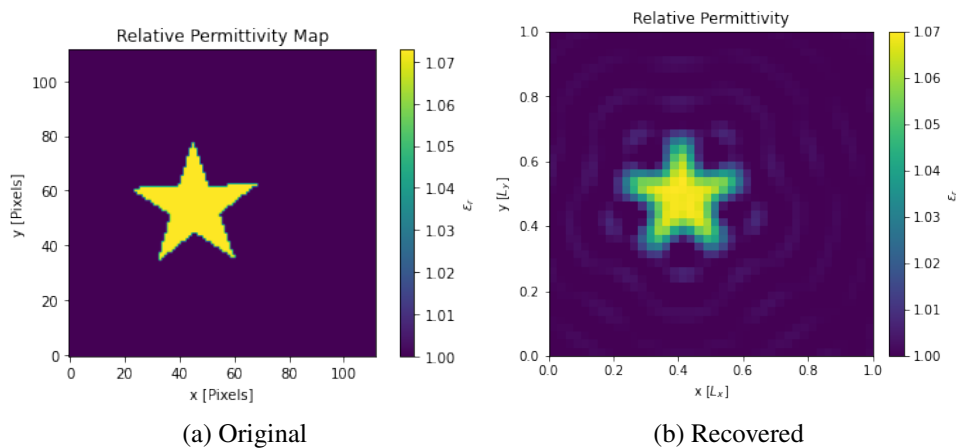


Figura J.1: Example images for shape metrics.



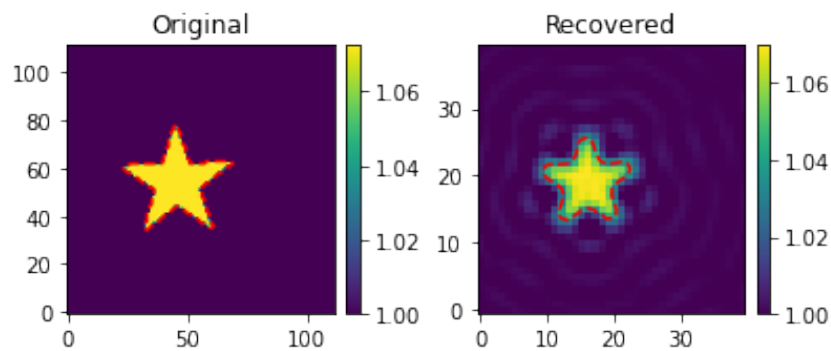


Figura J.2: Contours of original and recovered images.

The main idea is to calculate the difference area of the two contours. Of course, the area of one minus the area of the other would not work because the two forms might have equal areas but completely different forms. The following algorithm calculates the area of the difference:

1. Calculate the contours;
2. Correct the scale of the recovered contour to be equivalent to the size of the original image;
3. Center the image to isolate the object's position effect;
4. Check which pixels of the image are on each of the objects;
5. Separate those pixels that are in one of the objects and not in the other;
6. Calculate the quantity and multiply by an area element considering the limits equal to 0 and 1.

This algorithm is implemented in the following Python3 code:

```
# Evaluate contours
co = measure.find_contours(original, 1.0, fully_connected='high')
cr = measure.find_contours(recovered, threshold)

# Converting scale of recovered contour
for i in range(len(cr)):
    cr[i][:, 1] = original.shape[1]*cr[i][:, 1]/recovered.shape[1]
    cr[i][:, 0] = original.shape[0]*cr[i][:, 0]/recovered.shape[0]

# Thresholding
masko = np.zeros(original.shape, dtype=bool)
maskr = np.zeros(recovered.shape, dtype=bool)
masko[original > 1] = True
maskr[recovered >= threshold] = True

# Evaluate centers
xo, yo = np.meshgrid(np.arange(0, original.shape[1]),
                     np.arange(0, original.shape[0]))
xr, yr = np.meshgrid(np.linspace(0, original.shape[1]-1, recovered.shape[1]),
                     np.linspace(0, original.shape[0]-1, recovered.shape[0]))
xco = np.sum(masko*xo)/np.sum(masko)
```

```

yco = np.sum(masko*yo)/np.sum(masko)
xcr = np.sum(maskr*xr)/np.sum(maskr)
ycr = np.sum(maskr*yr)/np.sum(maskr)

# Centralization
for i in range(len(co)):
    co[i][:, 0] = co[i][:, 0]-yco+original.shape[0]/2
    co[i][:, 1] = co[i][:, 1]-xco+original.shape[1]/2

# Centralization
for i in range(len(cr)):
    cr[i][:, 0] = cr[i][:, 0]-ycr+original.shape[0]/2
    cr[i][:, 1] = cr[i][:, 1]-xcr+original.shape[1]/2

# Verify points
masko = np.zeros(original.shape, dtype=bool)
counter = np.zeros(original.shape)
for i in range(len(co)):
    maskt = measure.grid_points_in_poly(original.shape, co[i])
    counter[maskt] += 1
    masko[np.mod(counter, 2) == 1] = True

# Verify points
maskr = np.zeros(original.shape, dtype=bool)
counter = np.zeros(original.shape)
for i in range(len(cr)):
    maskt = measure.grid_points_in_poly(original.shape, cr[i])
    counter[maskt] += 1
    maskr[np.mod(counter, 2) == 1] = True

# Xor operation
diff = np.logical_xor(masko, maskr)

# Area of the difference
zeta_s = np.sum(diff)/np.sum(masko)*100

# Figure
fig, axis = plt.subplots(ncols=3, figsize=[3*6.4,4.8])
fig.subplots_adjust(wspace=.5)
axis[0].imshow(masko, origin='lower')
axis[0].set_title('Original')
axis[1].imshow(maskr, origin='lower')
axis[1].set_title('Recovered')
axis[2].imshow(diff, origin='lower')
axis[2].set_title('Difference')

plt.show()

```

This code yields results in Figura J.3. The  $\zeta_S$  measure in this case was 20.68%.

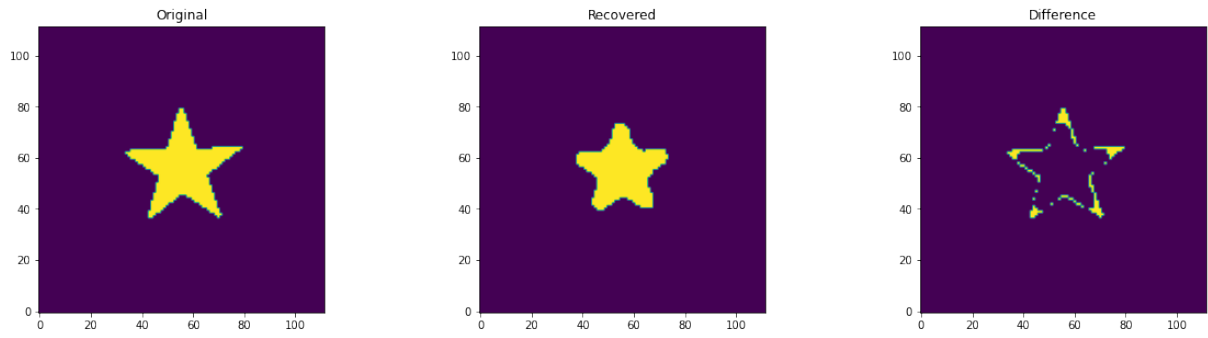


Figura J.3: Original, recovered and difference area.